FEM MODELLING AND CHARACTERIZATION OF ULTRASONIC FLEXTENSIONAL TRANSDUCERS

Monica La Mura

UNIVERSITY OF SALERNO

DEPARTMENT OF INDUSTRIAL ENGINEERING

Ph.D. Course in Industrial Engineering
Curriculum in Electronic Engineering - XXXI Cycle

FEM MODELLING AND CHARACTERIZATION OF ULTRASONIC FLEXTENSIONAL TRANSDUCERS

Supervisor
Prof. Nicola A. Lamberti

Ph.D. student
Monica La Mura

Scientific Referees
Prof. Alessandro S. Savoia
Prof. Giosuè Caliano

Ph.D. Course Coordinator
Prof. Ernesto Reverchon

List of publications

Journal articles

La Mura, M., Lamberti, N. A., Mauti, B. L., Caliano, G., & Savoia, A. S. (2017). Acoustic reflectivity minimization in Capacitive Micromachined Ultrasonic Transducers (CMUTs). Ultrasonics, 73, 130–139. https://doi.org/10.1016/j.ultras.2016.09.001

Book chapters

Lamberti, N. A., La Mura, M., Apuzzo, V., Greco, N., & D'Uva, P. (2018). A Sensor for the Measurement of Liquids Density, 431, 30–36. https://doi.org/10.1007/978-3-319-55077-0_5

Lamberti, N. A., La Mura, M., D'Uva, P., Greco, N., & Apuzzo, V. (2018). A New Resonant Air Humidity Sensor: First Experimental Results (pp. 79–87). https://doi.org/10.1007/978-3-319-66802-4_12

Lamberti, N. A., La Mura, M., Guarnaccia, C., Rizzano, G., Chisari, C., Quartieri, J., & Mastorakis, N. E. (2019). An ultrasound technique for the characterization of the acoustic emission of reinforced concrete beam. Lecture Notes in Electrical Engineering (Vol. 489). https://doi.org/10.1007/978-3-319-75605-9_9

Conference proceedings

Lamberti, N. A., La Mura, M., Apuzzo, V., Greco, N., & D'Uva, P. (2016). Optimization of a piezoelectric resonant sensor for liquids density measurement. IEEE International Ultrasonics Symposium, IUS, 2016–Novem, 16–19. https://doi.org/10.1109/ULTSYM.2016.7728670

Lamberti, N. A., La Mura, M., Greco, N., D'Uva, P., & Apuzzo, V. (2017). A resonant sensor for relative humidity measurements based on a polymer-coated quartz crystal. Proceedings - 2017 7th International Workshop on Advances in Sensors and Interfaces, IWASI 2017, 259–262. https://doi.org/10.1109/IWASI.2017.7974266

La Mura, M., Lamberti, N. A., Caliano, G., & Savoia, A. S. (2018). An ultrasonic flextensional array for acoustic emission techniques on concrete structures. In 2018 IEEE International Ultrasonics Symposium (pp. 1–4). https://doi.org/10.1109/ULTSYM.2018.8580178

Table of contents

List of figures

List of tables

Abstract

This work describes the finite element modelling and characterization of ultrasonic flextensional transducer arrays. Flexural acoustic transducers can be piezoelectrically actuated plates or capacitive devices based on the electrostatic attraction between a moving electrode and a substrate. Due to the limited miniaturization allowed by the piezoceramic fabrication process, piezoelectric flexural devices based on bulk ceramics are able to work in the low-frequency ultrasonic range. Capacitive flexural devices, instead, can take advantage of the Silicon micromachining techniques to be fabricated to reach higher frequencies.

Capacitive Micromachined Ultrasonic Transducers (CMUTs) are MEMS devices consisting of miniaturized metallized membranes, forced into flexural vibration by an electric signal during transmission, and vice versa generating a voltage signal when actuated by an incident acoustic signal. Due to their low acoustic impedance, CMUT arrays have given excellent results in ultrasound imaging applications.

The most recent frontier of ultrasound imaging is real-time volumetric imaging. 3D images have been originally obtained by means of linear phased arrays mechanically titled along the elevation plane. More complex structures like 2D arrays allow electronic beam steering and dynamic focusing in both azimuthal and elevation planes, thus achieving better performance. In order to increase the achievable frame rate, though, part of the front-end transceive and beamforming operations must be performed in probe. Therefore, 2D arrays should be small-sized and easily interfaced with the front end. Nevertheless, 2D arrays with good radiation characteristics require wide apertures with a small pitch between elements, therefore a great number of elements and many channels to wire and control individually. To overcome these issues, much attention is being focused on the design of sparse arrays, which try to achieve comparable performance by counting a lower element number.

For the design of optimized CMUT devices, accurate modeling is mandatory: the propagation of the acoustic wave produced by a source made of multiple vibrating membranes radiating into a fluid-like medium cannot be fully described by analytical models, thus CMUT devices must be simulated by Finite Elements Models (FEM). In this work, a simplified model of a wide

aperture multicell CMUT device was used to develop a tool to support the design process. The model was used to investigate the design parameters variation effect on the static and dynamic performance of CMUT arrays composed of circular cells. The collapse voltage, the membrane deflection profile and the static capacitance of Reverse-Fabricated CMUT devices (RF-CMUTs) were computed by varying the membrane radius and thickness and the cavity height. Since devices fabricated by the Reverse Fabrication Process are built from top to bottom, the Silicon Nitride base can be made very thin, and the devices can be backed by arbitrarily designed backing layers. The backing material effect on the pulse-echo behavior of immersed CMUT devices was investigated, and the reverberation phenomenon reduction was observed by matching the backing material acoustic impedance to the acoustic impedance of the propagating medium.

In order to investigate the performance of a sparse CMUT array, a 3D FEM model is needed, since there is no axial symmetry in a sparse array layout. For this reason, a full model of a reverse CMUT cell was implemented, tested and experimentally validated. Due to the long simulation time required by the FE analysis of a finite transducer element, a mesh optimization study was carried out on a simpler structure, i.e. an infinite transducer. The results of this optimization process were used to mesh a CAD-imported model of a sparse array element.

The studied array element is part of a multi-chip module (MCM) comprising a CMUT array based on a density tapered Fermat's spiral and an analog front end (AFE) ASIC wafer-bonded to the transducer array by means of a Benzocyclobutene (BCB) layer. The 10-mm array is designed for broadband operation around 7 MHz in immersion operation, and is made by 256 1.0λ-wide elements consisting of 19 hexagonally tiled circular cells. The proposed model was used to perform a harmonic analysis in ANSYS, in order to compute the element factor that modulates the array radiated pressure field. The study of the array element directivity is important to assess the beam steering capabilities of the device. The beam pattern was computed by varying the mechanical boundary conditions applied to the array element, in order to investigate the effects of an acoustic isolation of the array element, achievable by performing trenches in the BCB layer or in both the BCB and the structural nitride. The results obtained for the device included in an infinitely extended structure are in good agreement with the measurement performed on the probe head prototype featuring the MCM, though some differences in the main lobe and side lobe level exist, probably due to the incorrect compensation for the hydrophone directivity applied.

The FEM model of the wide aperture multicell CMUT was used as a basis to model a flextensional array of circular membranes actuated by piezoelectric disks, housed inside the cavity and glued to the rear of the membrane. The transducer array was designed for broadband reception operation in concrete-coupled condition, in order to perform efficient acoustic emission

measurements for the monitoring of concrete structures. The piezoelectric flextensional array design process was based on the computation of the device reception transfer function, obtained in concrete-coupled conditions by varying the geometrical parameters of the elastic plate, of the structural layer and of the backing. The resulting device has a 200 kHz wide -6 dB reception sensitivity bandwidth around the center frequency of 112 kHz, thus is suitable for acoustic emission techniques applied to concrete structures.

Introduction

This work is a study on ultrasonic acoustic transducers based on plates moving by flexural vibration. The applications considered are ultrasound imaging and acoustic emission techniques for the monitoring of concrete structures.

In this kind of devices, the generation and reception of acoustic waves is obtained by the vibration of membranes with fixed rim, which bend and extend along the direction normal to their surface. Ultrasonic transducers based on flexural plates are devices able to convert energy from the electrical to the mechanical domain, and vice versa. The operating principle can be piezoelectric or capacitive. In the case of piezoelectric flextensional transducers, the flexural vibration and normal extension of an elastic membrane is obtained by exciting a piezoelectric element coupled to a bending plate. The deformation of the piezoceramic bends the membrane causing the flexural deformation that originates the transmission of an acoustic wave. In the case of capacitive transducers, a hollow cavity is obtained inside an elastic structure, and two electrodes are placed on top and at the bottom of the gap. By applying a static voltage across the electrodes, the electrostatic force causes the bending of the top plate towards the substrate. Providing an alternate voltage signal makes the suspended membrane move by flexural vibration, generating an acoustic wave. The main characteristics of flextensional devices is that their mechanical impedance is much lower than the mechanical impedance of thickness mode piezoelectric transducers, which makes them particularly suitable for broadband operation when coupled to low-to-medium acoustic impedance propagating media.

The broadband sensitivity of flexural membranes is centred around the frequency of the first resonant mode of the membrane. The first resonance frequency is inversely proportional to the square of the membrane size, therefore the maximum frequency of operation achievable by an ultrasonic device is determined by the miniaturization level allowed by the fabrication process. The techniques for the fabrication of piezoelectric bulk ceramic plates and disks do not allow miniaturization below the mm-scale. For this reason, piezoelectric flexural devices based on bulk piezoceramics can be used for sensing and non destructive testing applications, which require frequencies of

operation below the MHz. Ultrasound imaging, instead, is performed at frequencies above 1 MHz an up to 20 MHz, therefore flexural devices for imaging must have apertures of tens-to-hundreds of microns. Piezoelectric devices with dimensions in the sub-mm scale can only be obtained by film deposition. On the contrary, capacitive transducers can be fabricated as MEMS devices by taking advantage of the well-known Silicon micromachining techniques, and therefore can work at high frequency with a reduced technological effort. These devices are known as CMUTs – Capacitive Micromachined Ultrasonic Transducers. CMUTs can reach high performance in the medical ultrasound imaging application. In particular, the CMOS-compatible fabrication technique of CMUTs makes these devices very appealing for critical imaging applications, such as real-time volumetric imaging. In fact, in order to perform successfully a high frame-rate volumetric imaging, the front-end electronics should be placed in probe; therefore, the transducer array must be small-sized and directly coupled to the transceiver electronic and the beamforming circuits.

The investigation of the propagative behaviour of such ultrasonic devices involves a coupled-field analysis that requires multiphysical PDEs solution, unless strong simplifications are assumed. A reliable prediction of the devices electroacoustic behaviour, which is necessary for an accurate application-specific design, requires simulation by finite element analysis. In this work an ANSYS FEM model for the simulation of ultrasonic transducer arrays is developed. The FEM model of CMUT devices is used to investigate the performance of dense and sparse 2D arrays for medical imaging. Wide aperture multicell devices are simulated by means of a 2D axisymmetric model, and a sparse array element is simulated by a 3D model with finite dimensions. FEA is also used to support the design of a piezoelectric device for acoustic emission techniques for the structural monitoring of concrete structures.

Chapter I introduces CMUT devices for ultrasound imaging, describing the most common types of probes and focusing on a new 2D sparse array of Reverse-Fabricated CMUTs based on a Fermat's spiral pattern.

Chapter II thoroughly describes the developed FEM models for the simulation of multicell CMUTs, such as 2D dense arrays or wide aperture single element transducers, and for the simulation of the directivity pattern of a sparse array element.

The effect of the variation of the structural dimensions and of the bias voltage on the static and dynamic transmission and reception performance of immersed CMUT devices is analysed in Chapter III, thus showing how FEM can support the design process by leading to the CMUT device optimization.

Chapter IV is dedicated to the performance analysis of the 2D spiral array element, whose one-way beam pattern is compared to the measured directivity of the fabricated prototype.

Finally, the design of a flextensional transducer, based on piezoelectric disks activating the flexural vibration of an array of membranes, is carried out in Chapter V. Such piezoelectric flextensional array is optimized for the application to acoustic emission techniques applied to concrete structures, for the structural health monitoring.

Chapter I
CMUT arrays for ultrasound imaging

I.1 Transducers for medical ultrasound imaging

Ultrasound (US) imaging is the preferred technique for the investigation of human body tissues, such as organs, muscles, tendons and vessels. In fact, US imaging offers several advantages over other available imaging techniques: it is completely harmless and non-invasive, provides real-time images and is cost-effective. Images of anatomic structures are obtained by transmitting and receiving ultrasonic acoustic waves propagating through the human body, by means of an electroacoustic transducer device. The fabrication technology of transducer arrays for ultrasound imaging based on piezoelectric materials is nowadays very mature and therefore hardly improvable. During the last two decades, excellent results were obtained by new MEMS devices, fabricated by silicon micromachining technology and based on the electrostatic cell working principle. These devices are known as CMUTs, which stands for Capacitive Micromachined Ultrasonic Transducers. Transducer arrays fabricated by CMUT technology have reached top-level performance.

The use of arrays instead of solid apertures for medical imaging can be easily justified by the numerous advantages arrays grant with respect to single-crystal transducers [1], [2]. For instance, using multiple active elements allows for electronic beam steering and focusing. Besides, the use of arrays enables the adjustment of the lateral resolution and the beam shaping by the electronic aperture *apodization*, which means that the active aperture can be changed dynamically by exciting only a part of the available array elements. Moreover, a dynamic focusing can be obtained in receive mode, so that the highest resolution achievable can be maintained through the entire scan depth. It should also be noticed that all of these features can be obtained without mechanically tilting the probe, therefore reducing the needs for mechanical maintenance.

I.1.1 1D arrays

1D arrays, such as linear arrays, curvilinear arrays and phased arrays, are made by several elements arranged along a line and controlled independently from one another. Let us suppose the elements are arranged along the *x*-direction on the *xy* plane, and the propagation of ultrasonic waves takes place along the z-direction. These kinds of transducer arrays generate images of planar sections of the human body, and allow dynamic focusing in the azimuthal (*xz*) plane. The focus in the elevation plane (*yz*) is fixed by an acoustic lens.

Linear arrays are usually made by up to 256 elements, but only a small number of elements are excited at the same time. The resulting image has a rectangular shape, with a constant density of scan lines.

Convex arrays, also called curvilinear arrays, are essentially linear arrays arranged on a curved convex structure. Due to the natural divergence of such shape, the sequential excitement of a small number of adjacent elements allows the scanning of a wider sector of the azimuthal plane, hence returning an annular sector of the scanned plane with a line density decreasing by increasing the depth.

Phased arrays count up to 128 elements, as they are designed to have a smaller footprint in order to investigate parts of the body with small access areas. As for linear arrays, the number of elements excited at the same time can be varied, but the fired elements are always centred at the centre of the array. Moreover, by exciting the elements with a different amplitude (electronic aperture apodization), the active area of the transducer can be electronically reduced to have a wider main lobe of the radiation pattern, or the array can be excited by signals whose amplitude is modulated by a Hanning window, in order to reduce the side lobe level. By providing phased input signals, instead, the transmitted beam can be steered in order to focus at different depths on the propagation direction, on a wide angular range of the azimuthal plane. In this way, a wider part of the body in front of the transducer surface can be investigated by a small aperture, obtaining a trapezoidal shaped image of the investigated area. This feature is particularly useful for cardiac imaging applications, where the probe head must fit in between the ribs in order to reach the heart without any shading caused by the bones. Also in this case, the line density decreases at the bottom of the image.

I.1.2 2D arrays

2D arrays are made by elements arranged along rows and columns. By controlling the array elements individually along both directions, the input signals can be tuned in order to have the beam steered and focused at different depths on the elevation plane as well as on the azimuthal plane, thus granting much more flexibility with respect to 1D arrays. The dynamic focusing in an

arbitrary point of the half space facing the transducer made available by 2D arrays has moved increasing attention towards the imaging of volumes. The steep improvement in the computational power of modern architecture also fostered the development of volumetric imaging performed in real-time, in order to observe moving volumes with an acceptable frame rate. This feature is particularly interesting for the diagnosis of cardiac diseases.

With respect to traditional probes for volumetric US imaging, the capability of 2D arrays to steer the beam electronically in both azimuthal and elevation direction eliminates the need for mechanical rotation and tilting of the probe, with a consequent increase of the achievable frame-rate. In fact, volumetric imaging has been traditionally performed by means of mechanical 3D probes: such probes are based on 1D linear or convex arrays, moved under computer control or by freehand translation to collect the 2D frames used to render the volume of the investigated region. The rotation and tiling of the conventional 1D transducer array is performed either by an external fixture (rather bulky and heavy) or by an in-probe integrated positioning system [3], [4]. Although this technique is effective for the rendering of the observed volume, the mechanical scan is inevitably too slow to allow real-time imaging of moving volumes. Moreover, it is strongly subject to errors and uncertainty, due to the necessity of position-sensing devices and tracking systems. 2D arrays do not require this increased complexity, as they rely on electronic scanning, which is undoubtedly faster. The first attempts at volumetric imaging by means of 2D arrays date back to 1991, when a preliminary real-time 3D scan with 8 frames/s was demonstrated by means of a 289-elements piezoelectric transducer array [5], [6]. Developing fully sampled matrix arrays, though, introduced new issues to deal with. Due to the spatial repetition of elements across the array surface, grating lobes can arise in the radiation pattern. Grating lobes cause dispersion of the radiated energy, and are responsible for the formation of artefacts on the ultrasound image. In order to avoid the formation of grating lobes in the directivity pattern of the radiated pressure field, the distance between adjacent cells (pitch) should be less than half wavelength. On the other side, large apertures are required for a good lateral resolution. Therefore, having a wide aperture and small elements means dealing with a very high number of elements, and each of them must be controlled individually. The consequences are a high difficulty in the channel wiring, a great complexity of the front-end electronics, a strong power dissipation and, finally, a high cost. For this reason, the first 3D scan system based on 2D transducers, proposed in 2002 by Philips, reduced the data coming from about 3000 acoustic elements to just 128 signals according to the method described in [7], which could then be processed by a conventional ultrasound system. Soon after, a fully sampled 2D array made by CMUT technology was proposed, though the first volumetric images obtained by means of a CMUT probe were produced by a small 16x16 elements sub-array [8]. Even now, the only way to use fully-sampled arrays to perform real-time

volumetric imaging is to scale down the channel number to a maximum of 256 [9], [10].

One possible solution to reduce the number of channels to be wired and connected to the external ultrasound system is to implement μ-beamforming techniques for the beam formation and received signal processing [11], [12]. The beamformer is the system in charge of controlling the ultrasonic beam characteristic in transmission and reception. The transmit beamformer generates the delay pattern of the input signals, in order to steer and focus the beam. The receive beamformer delays the signals received from different depths and sums the realigned signals, in order to provide the data for the image reconstruction. The beamforming in reception is usually performed according to delay-and-sum (DAS) algorithms, even though non-linear algorithm such as the delay-multiply-and-sum (DMAS) have also been proposed for a higher dynamic range in B-mode images [13]. The beamforming can be performed digitally [14] or analogically [15]. Analog beamforming is not suitable for 2D arrays, as it does not allow dynamic focusing and requires a considerable area to include all the needed components. Digital beamforming, nonetheless, also requires space on the ASIC for the analog-to-digital converters (one for each element), and is therefore not suitable for high element counts. In the case of a high element number, the μ-beamforming is a valid solution to reduce the number of cables connected to the external imaging system. The μ-beamforming is a two-steps beamforming technique, where the transducer array is divided into sub-apertures. The echo signals from the elements of each sub-aperture are processed by an in-probe ASIC, which performs a preliminary realignment of the echoes and returns one output signal for each sub-aperture into which the array is divided. In this way, only one cable per sub-aperture is routed to the main beamformer in the external imaging system, which combines the signals pre-processed by the μ-beamformers into one final output signal used for the image reconstruction [16]. This method is currently used in commercial real-time 3D imaging systems.

In order to overcome the issues related to the connection of a high element number, much attention is also being focused on the design of sparse arrays, which try to maintain acceptable performance while counting a lower element number. Lessening the element count also increases the achievable frame rate of volumetric imaging, since it reduces the amount of data that must be processed. For this reason, sparse arrays have become even more appealing with the increasing interest for volumetric imaging. Removing elements from the array, though, intrinsically lowers the array sensitivity, and at the same time degrades the acoustic beam pattern, as the energy missing from the main lobe reappears in the form of grating lobes or by increasing the side lobe level. The issues related to sparse array design were already faced in the early 1990s [17]–[19], and new methods are still under investigation [20]–[24]. Grating lobes can be avoided by breaking the spatial periodicity of the remaining

active elements, but improving the sparse array performance over a wide range of steering angles requires a strong effort in the design optimization. Recently, good results were obtained by arranging the elements outside of the rows and columns of a grid, by following a spiral pattern [25]. In particular, a method for the design of a sparse array realized by arranging cell clusters according to a Fermat's spiral pattern has been proposed [26]. Simulation results encourage the study of this particular array topology in order to obtain good performance with a limited number of active elements. The improvement in 2D array design are particularly important for the outcome in real-time volumetric cardiac imaging, which is undoubtedly the critical application for ultrasound imaging.

I.2 History and *state-of-art* of CMUTs

I.2.1 CMUT devices

Capacitive Micromachined Ultrasonic Transducers (CMUTs) are MEMS devices consisting of metallized Silicon membranes suspended over a cavity, with the outer edge clamped onto a conductive substrate. The membranes are set into flexural vibration by an electric signal during transmission, and vice versa generate a voltage signal when actuated by an incident acoustic signal. A multitude of electrostatic cells represents a CMUT array.

CMUTs were firstly developed in the mid-1990s [27], mainly pushed by the idea of obtaining high-frequency ultrasonic transducers for air-coupled operations. In fact, technological issues do not allow the use of piezoelectric devices at high frequencies in air. The acoustic impedance mismatch between the piezoceramic and the air requires the interposition of matching layers between the two materials; though, finding low-loss materials with the needed acoustic impedance is not a simple task. Moreover, the thicknesses required for operation in the MHz range are unachievable for such materials. On the contrary, CMUTs have an intrinsically low mechanical impedance, so they have been soon recognized as suited for air-coupled operation. Efficient air-coupled transmission was soon demonstrated [28], [29], and shortly followed by the demonstration of broadband water-coupled transmission [30]–[32]. As the first results proved CMUTs could compete with piezoelectric devices for immersion operation [33], the first CMUT-based devices for medical ultrasound imaging appeared: fully functional 1D linear [34] and phased arrays [35], 2D dense arrays [36] and annular arrays [37] were fabricated and characterized. Soon after, the first ultrasound images obtained by means of CMUT devices were demonstrated [38]–[41]. Since then, several other CMUT arrays for imaging applications were proposed [42], [43] before Hitachi Medical Corp. came out with the first commercial CMUT probe in 2009. Later, research has moved great steps towards the optimization of CMUT arrays for high-performance ultrasound imaging [44]–[48]. Finally,

during the last years, CMUT technology became consolidated and is currently transforming from a research topic to a commercial reality.

I.2.2 CMUT fabrication techniques

CMUT arrays are fabricated by surface micromachining techniques [49]. The traditional approach to CMUT fabrication starts from a Silicon wafer, where a sacrificial layer is deposited and covered by the Silicon Nitride membrane layer by *Low-Pressure Chemical Vapor Deposition* (LPCVD). In the first reported technique, the sacrificial layer was an oxide layer, removed by a selective wet etching process through vias created in the membrane. In this way, a vibrating freestanding structure is created [50], [51]. Figure I.1 describes the steps for the fabrication of CMUT devices by the classic sacrificial-release technique.

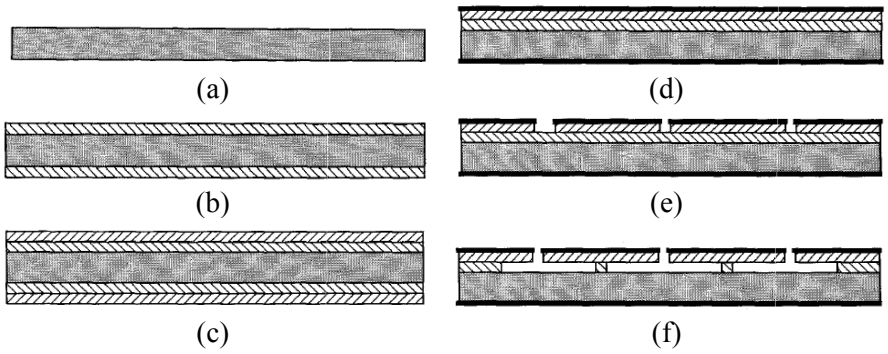

Figure I.1 *An example of a traditional sacrificial-release fabrication process, as described in* [50]. *The frames show: (a) the starting Silicon wafer, (b) the Silicon oxide growth, (c) the LPCVD Silicon Nitride deposition, (d) the Au metallization deposition, (e) the membrane etching, (d) the sacrificial layer etching.*

In the early years of CMUT technology development, also examples of CMUT-on-CMOS were reported [52]. The deposition technology quickly switched to *Plasma-Enhanced Chemical Vapor Deposition* (PECVD), in order to keep the temperature below 400°C, and the use of Chromium as sacrificial layer was described [35]. Since the classical fabrication technique requires to make vias through the membrane to empty the cavity, which can affect the acoustic performance of the device, different techniques for the transducer fabrication were investigated. One example is the transducer assembly by wafer bonding [53]. Another solution was proposed by Roma Tre University [54], [55], where a technique named *Reverse Fabrication Process* was developed. The steps for the fabrication of CMUTs by reverse technology are described in Figure I.2. By reverse fabrication, CMUTs are built from top to bottom, starting from a Silicon wafer already covered by a layer of LPCVD

Silicon Nitride. The top electrode is realized by Aluminum evaporation, and then covered by a passivation Silicon Nitride layer, deposited by PECVD. On top of the Nitride layer, the sacrificial layer of Chromium is deposited. Chromium is then removed from the areas that must be filled with another deposition of the structural Silicon Nitride, in order to shape the cell. Afterwards, the second electrode and the last Silicon Nitride layer are deposited. Finally, vias are made through the structural layer to reach the remaining Chromium, which is etched by a selective wet etch process to create the cavity. In this way, the holes are drilled into the bottom layers of the device, so that they do not affect the acoustic behavior of the membranes. An arbitrarily shaped backing layer made of a sound-absorbing material, such as epoxy resin, can be attached to the back surface of the CMUT array, in order to provide mechanical support and also improve the device performance by absorbing the incoming pressure signals. At this point, the device can be flipped upside down, and the silicon wafer is etched up until the LPCVD Silicon Nitride, thus releasing the membrane.

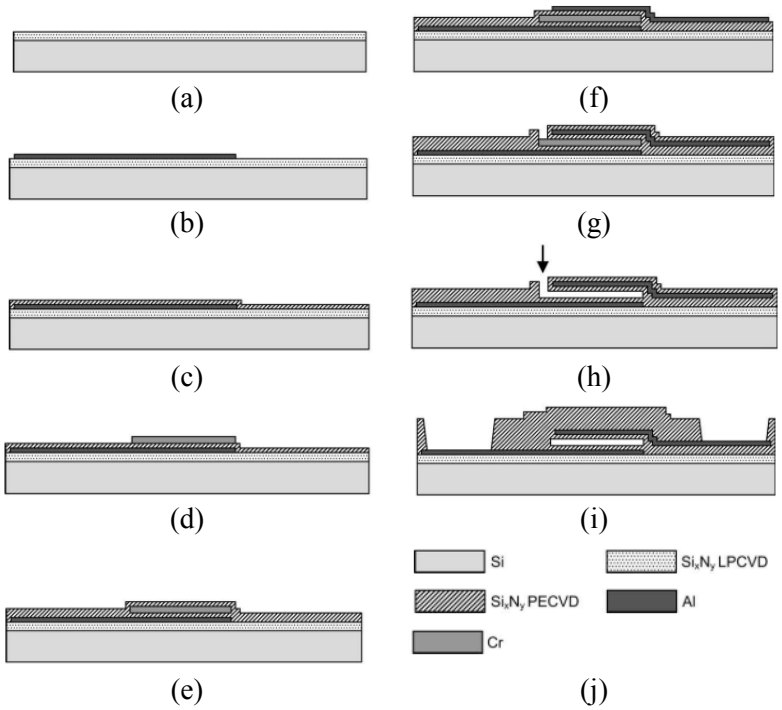

Figure I.2 *The steps for the fabrication of a CMUT device by reverse fabrication process: (a) LPCVD SiN deposition, (b) top Al metallization deposition by evaporation, (c) passivation by PECVD SiN, (d) Chromium sacrificial layer deposition, (e) passivation by PECVD SiN, (f) bottom Al metallization deposition, (g) passivation and etching of the Nitride, (h) sacrificial layer etching, (i) base PECVD SiN deposition. Legend in (j). Images from* [44].

I.2.3 CMUTs for the next generation of US imaging

After the development of fully functional CMUT based probes for ultrasound imaging, the technology was pushed forward by developing different kinds of CMUT-based probes for advanced applications. For example, side-looking catheters [56], for intravascular guidance and navigation, and forward-looking catheters [57], for intravascular therapy delivery and lesion assessment, were proposed and demonstrated to be feasible. The first in-vivo intravascular ultrasound image obtained with a CMUT array was obtained in 2012 [58]. Much more recently, an example of intravascular array for volumetric imaging in intracardiac echography was also proposed [59], in the view of a next generation of high-performing devices enabling improvements in life-saving technologies.

Some recent developments also concern the optimization of high-frequency CMUT arrays [60] and criss-cross arrays for biplane imaging [61].

For what concerns classical ultrasound imaging, the next frontier is high frame rate volumetric imaging, especially interesting for cardiac investigation. As previously outlined, volumetric imaging can be performed by 2D arrays, but a high frame rate can only be achieved by reducing the element count, hence by using sparse arrays. For this reason, there is currently a great interest in the development of 2D sparse arrays for fast, real-time 3D imaging. It should also be noticed that, by means of one single probe, whole-body imaging can be performed, since the wide bandwidth of CMUTs allows working at different frequencies and the aperture can be dynamically modified to suit the desired application.

Furthermore, CMUT devices can be more easily interfaced to the CMOS in-probe electronics with respect to traditional piezoelectric transducers. The feasibility of coupling the transducer array and the front-end ASIC (CMUT-on-ASIC) by flip-chip bonding techniques was investigated [62]–[64], and the coupling was successfully obtained for some of the available channels. The scope is the realization of integrated modules for miniaturized, low-weight, low-cost and energy efficient portable imaging systems. The peculiarity of these systems is that the transmit and receive beamforming is performed entirely by the ASIC device coupled to the CMUT array, and the data is processed in-probe. This will allow the development of all-in-one portable devices for point-of-care ultrasound, that can perform ultrasound imaging by simply connecting to a mobile device, such as a smartphone or a tablet, and can also send the data in the cloud to be shared. An example of such device was recently announced by Butterfly Network, Inc.

I.3 A Reverse-Fabricated 2D CMUT spiral array

The reasons behind the increasing attention towards sparse array configurations were introduced in Section I.1.2. Various random and

deterministic layouts of sparse arrays have been studied since the early 1990s. One deterministic pattern that prevents a periodicity in the spatial sampling of elements is the spiral pattern. Among all different spiral patterns, the Fermat's spiral pattern for the arrangement of transducer array elements was considered in [65]. In a *N*-elements Fermat's spiral based array, the position of the *n*-th element in polar coordinates is given by the couple

$$\theta_n = n\,\alpha \tag{I.1}$$

$$r_n = R_a \sqrt{\frac{\theta_n}{\theta_N - 1}} \tag{I.2}$$

where α is the *divergence angle*, which determines the number of branches of the spiral, and R_a is the aperture radius.
The configuration obtained by using a divergence angle α equal to the golden angle

$$\alpha = \pi\left(\sqrt{5} - 1\right) \tag{I.3}$$

is also known as the "sunflower" pattern. The main characteristic of this pattern is that the spatial density of the elements is kept constant but there are no elements with the same angular position, hence any kind of spatial periodicity is prevented. For this reason, this particular spiral pattern was investigated for the design of a sparse CMUT array [66]. Spatial density tapering according to a Blackman tapering function was also introduced to reduce the side lobes level without introducing electronic apodization. Fabricating non-gridded array configurations with the fabrication approach used for piezoelectric transducers is particularly complicated. The fabrication of CMUT devices is much more suitable to the construction of these non-periodic structures. Reverse fabrication technology, in particular, has the advantage of allowing easy access to the connection pads, placed on the back of the device.

For this reason, a RF-CMUT spiral array was realized to be inserted in a Multi-Chip Module (MCM) comprising the transducer array and an ASIC, interconnected by means of a flip-chip bonding technique, according to the procedure described in [64], [67]. The RF-CMUT spiral array is designed for broadband operation in immersion around 7 MHz, with a two-way -6 dB fractional bandwidth of 100%. The array elements are 1.0λ wide (220 μm-wide aperture), arranged according to a sunflower pattern on a 10-mm quasi-circular area. Figure I.3 shows (a) the 6" wafer of the MEMS dice and (b) a close-up on the array die before the packaging operation.

Each element has a hexagonal shape and features 19 circular CMUT cells packed by hexagonal tiling with a centre-to-centre distance of 53 μm. Figure I.4 shows an optical microscopy view of (a) one array element and of (b) the CMUT spiral array.

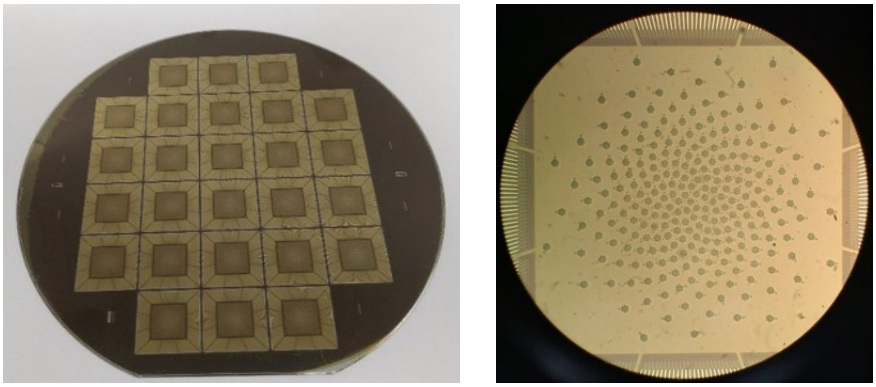

(a) (b)

Figure I.3 *RF-CMUT spiral array (a) dice on 6" wafer and (b) single die.*

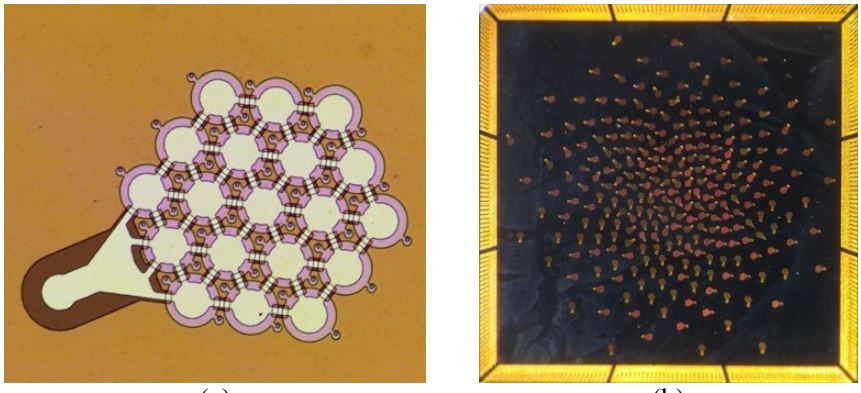

(a) (b)

Figure I.4 *Optical microscopy view of (a) one 19-cells 1.0λ-wide hexagonal element and (b) the RF-CMUT spiral array.*

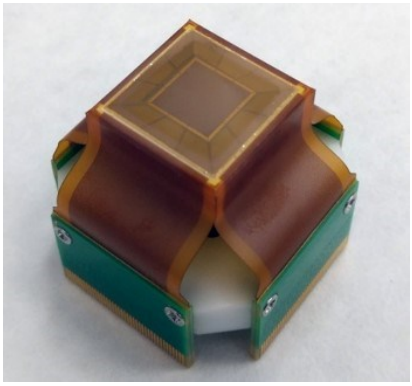

Figure I.5 *Probe head prototype including the multi-chip module comprising the RF-CMUT spiral array transducer flip-chip bonded to the analog front-end ASIC by means of an acoustically optimized integration technique.*

The ASIC is a 256-channel analog front end (AFE), featuring unipolar pulsers and low-noise amplifier for the transceive operation, together with a programmable transmit beamformer. The channel pads layout was specifically optimized for the interface with the spiral transducer array. Figure I.5 shows a probe head prototype mounting the flip-chip bonded MCM.

Chapter II
Finite Element Modelling of CMUT devices

II.1 The need for Finite Element Analysis in the study of CMUTs

The earlier models for the simulation of CMUT cells were based on the assumption of piston-like displacement of the membrane (uniform displacement along one axis, normal to the transducer surface), leading to the acoustic behaviour of a piston radiator and the electrical behaviour of a moving parallel plate capacitor. This theory is easily described by 1D models, usually linearized around a bias point, and since the early days of CMUT simulation transposed in a lumped parameter equivalent circuit [31], [50], [68]. Equivalent circuit models, featuring standard electrical components that represent mechanical, acoustic and electrical elements, allow the use of electrical network analysis to predict easily the behaviour of a complex vibrating system. Lumped parameters circuit always involve the presence of a transformer, which represents the energy conversion from the electrical domain to the mechanical domain and vice versa [69]. During the years, this kind of models have been expanded and improved in order to include the effects of other parameters, such as the electrode size [70], the atmospheric pressure [71], the air in the cavity (if present) [72], the interaction with nearby membranes [73] and some of the higher order modes [74].

Another approach for the time-domain simulation of the nonlinear behaviour of CMUTs relies on the numerical solution of the simplified differential equations that describe the multiphysical system. These nonlinear models take into account the intrinsic nonlinearities of the electromechanical coupling (the electrostatic force depends on the square of the applied voltage, as will be explained in Section III.3), thus allowing the simulation of the effect of large signals applied across the electrodes. Nonlinearities are also figuring in equivalent circuit models in form of controlled sources [75].

Even if these models give accurate results around the first resonance frequency of the membrane, they fail in simulating the high frequency

behaviour of the transducer, where higher order modes intervene and determine a variation of the transmitted pressure. An analytical method for the simulation of higher order modes based on the mode superposition analysis was proposed in [76], but gives accurate results only after extracting the system parameters from measurements.

Consequently, the only reliable method for the time-domain simulation of the behaviour of CMUT devices that takes into account the acoustic fluid loading, the electromechanical coupling, the transducer non-linearity, the higher order resonant modes, the membranes cross-talk and the diffraction phenomenon is the Finite Element Method (FEM). Though very time consuming and computationally expensive, the Finite Element Analysis (FEA) is still the most complete tool for the accurate design of acoustic transducers.

By taking advantage of a circular CMUT cell rotational symmetry, a simple and light 2D axisymmetric FEM model of a CMUT cell was firstly presented in [77]. Originally, this model was used for the computation of the electromechanical coupling coefficient in conventional polarization [78] and in collapse-snapback regime [79], and then for the computation of the device electrical impedance in vacuum [80]. The axisymmetric FEM model was improved with the possibility to simulate the device propagative behaviour in [81], where the modelling of a fluid medium infinitely extended in the lateral directions by means of a cylindrical waveguide of fluid coupled to the transducer structural model was introduced. This acoustic coupling FEM model was then extensively used for the evaluation of the transmitted pressure in conventional operation and collapse-snapback operation [82], [83], and allowed the study of an impedance-matched backing effect on the CMUT arrays performance [82], [84]. 3D FEM models were also proposed for the simulation of different membrane geometries [85] and for the study of the cross-talk between near membranes [43]. These more accurate models were key-enablers for the design of high-performance CMUT dense arrays [42], [44], [86].

FEM simulation is the only simulation technique that can predict accurately also the performance of sparse arrays, where the directivity function of a small radiating element depends on the solution of the diffraction integral, and is strongly influenced by the acoustic interaction of a small number of membranes close to each other. The implementation of a FEM model of a dense array was then considered a preliminary step for the realization of a more complex model of a Fermat's spiral-based sparse array element.

The next section introduces the infinite transducer model, a simplified model that represents a wide aperture device made by closely packed, regularly spaced circular membranes, implemented in ANSYS (ANSYS Inc, Canonsburg, PA) by means of a 2D axisymmetric model and a 3D model. The infinite transducer model was used to compute the mesh size that was applied

in the meshing of the Fermat's spiral sparse array element described in the last section of this chapter.

II.2 The infinite transducer model

Large, regular arrays, where a high number of membranes are arranged in a grid-like fashion and are all operated in parallel for maximum output pressure, allow the exploitation of symmetry for the implementation of reduced-order FEM models. Such lighter models have the invaluable advantage of requiring shorter times for the simulation of time-domain signals propagation, without losing results accuracy.

By assuming the array lateral extension is large enough compared to the signal wavelength at the operating frequency, we can consider the transducer as if it were an infinite source radiating plane waves into the half space. Symmetry boundary conditions applied at the edge of one single cell create the model of an unbounded transducer, which extends infinitely on a plane orthogonal to the wave propagation direction. In such situation, the membranes composing the array would be all vibrating in phase, in a fluid of real acoustic impedance. For this reason, the assumption of wide aperture allows to simulate one single cell radiating plane waves, and then extend the results to the entire dense array made of several identical cells.

In order to support plane wave propagation, the semi-space of fluid can be represented by a cylindrical rigid-walled acoustic waveguide having a cut-off frequency higher than the maximum frequency involved in the analysis, in order to avoid the excitation of guided propagation modes. In fact, below the cut-off frequency of the first nonplanar mode of a rigid-walled waveguide with circular section, only plane waves can propagate, as if the signal were radiated in an infinitely extended medium [87]. The diffraction phenomenon gives an upper frequency limitation to the validity of such model. By increasing the frequency, the plane waves travel along the propagation direction with an increased angle θ with respect to the longitudinal axis [1]. At high frequencies, angled plane waves are reflected by the lateral rigid walls of the fluid waveguide, originating stationary waves that invalidate the model results.

As a consequence of this consideration, a dense array of regularly spaced identical cells can be modelled, in a reasonably wide frequency range around the first resonance mode of the device, by a single CMUT cell replicated along both lateral directions, radiating in a cylindrical column of fluid. The fluid waveguide radius matches half the centre-to-centre distance of the membranes, thus taking into account the spatial periodicity of the array.

If the cell has a circular geometry, the first resonance mode around which the sensitivity bandwidth in centred is an axisymmetric mode, and therefore the cell and the fluid waveguide can be represented by a 2D model of a half of the cross-section of the transducer and fluid medium.

Such model, described in Section II.2.1, was implemented in ANSYS and used to study a reverse-fabricated CMUT dense array, by investigating the effect of varying the geometrical parameters and increasing the bias voltage on the device static properties and on its dynamic performance in large signal regime.

The study of a sparse array element, instead, requires a 3D FEM model of the device, since the hypothesis of large aperture and plane waves propagation is no longer verified. In fact, the planar extension of an array element represents an aperture small with respect to the signal wavelength at the operating frequency. Moreover, the element structure does not exhibit any rotational symmetry; hence, no axisymmetric models can be used to simulate its behaviour. Due to the significant complexity of such a model, in order to find a trade-off between the results accuracy and the computational burden, a study for the mesh optimization was carried out on a lower complexity model. In particular, a 3D model of the infinite transducer was reproduced in ANSYS for the representation of an unbounded dense array of circular membranes arranged by both square and hexagonal tiling. This model is presented in Section II.2.2.

The results obtained by simulations performed on this model are compared to the results obtained on an already validated 2D model in Section II.3, in order to find the widest mesh size that grants accurate results without prolonging the simulation time unnecessarily. The resulting mesh size is then used on the FEM model of the Fermat's spiral array element, described in Section II.5.

II.2.1 2D axisymmetric model in ANSYS

The rotational symmetry of both the structure and the displacement (for frequencies around the first resonant mode) of a circular cell coupled to a cylindrical waveguide of fluid allows the reduction of a 3D cell model to a 2D axisymmetric model. Symmetry boundary conditions applied at the edge of the axisymmetric model can take into account the presence of a high number of identical cells regularly spaced on the transducer plane, composing an infinitely extended transducer array radiating into a half space of fluid. The commercial FEM software ANSYS is provided with elements that support axisymmetry, therefore a very light model can be used to investigate the behaviour of a 3D structure providing accurate results in the frequency range of interest.

In the 2D axisymmetric ANSYS model of a reverse-fabricated CMUT device, the membrane, the electrodes and the cell structure were meshed by PLANE42 elements (using the axisymmetric keyoption), defined by 4-nodes on a plane having two degrees of freedom (DOF) each: the displacement along the *x*-axis (UX) and the displacement along the *y*-axis (UY). The membrane was attributed the material properties of Silicon Nitride grown by Low-

Pressure Chemical Vapour Deposition, while the structural material was attributed the properties of Silicon Nitride grown by Plasma Enhanced Chemical Vapour Deposition. The plane elements describing the electrodes were attributed the material properties of Aluminium in order to take into account their contribution to the mechanical properties of the structure. However, their electrical activity was limited to the lower surface of the top electrode and the upper surface of the bottom electrode, where the voltage degree of freedom (VOLT) was made available by the application of TRANS126 elements between the facing nodes of these two surfaces. TRANS126 elements are 2-nodes fully coupled elements, which relate the electrostatic response and the structural response of an electromechanical device [88]. In particular, the transducer element models the capacitive response of a device to the motion in the direction defined by the connection of the element nodes *I* and *J*. In the proposed model, the nodes *I* and *J* of the applied TRANS126 elements lie on the upper surface of the bottom electrode and the lower surface of the top electrode, respectively. Being a 2-nodes element, each TRANS126 can be placed along one of the three nodal directions *x*, *y* or *z* in any of the global or local coordinate systems. In the proposed 2D model, the elements are directed along the y-axis, as shown in Figure II.1.

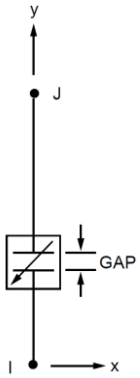

Figure II.1 *One TRANS126 element, applied across two nodes I and J and lying on the y-direction. The nodal displacement determines the gap, which is related to the capacitance associated to the considered element. Image taken from ANSYS Mechanical APDL Element Reference* [88].

The capacitance between the two coupled nodes *I* and *J* is related to the deflection by a polynomial function, whose coefficients the user can input by the real constant table. Being nonlinear elements, analyses including TRANS126 require an iterative solution to converge. The cavity was described by mesh-only MESH200 elements, which do not contribute to the solution, as the cavity is supposed to be sealed in vacuum.

The structural model of the RF-CMUT device was realized by defining the geometrical parameters as variables, so that these values could be easily replaced to model a similar structure with different dimensions.

Figure II.2 shows (a) the 2D axisymmetric model of the RF-CMUT cell modelled in ANSYS and (b) its axisymmetric 3/4 expansion, which is just a visual rendering of the structure that the FEM software simulates when the axisymmetric keyoption of the meshed elements is enabled. The axisymmetric model of a RF-CMUT cell in Figure II.2 includes, from top to bottom, the LPCVD Silicon Nitride membrane (in light green), the top electrode (in grey), which is common to all the cells of the array, the top and bottom passivation layers (in green) separated by the cavity (in red), the bottom electrode (in grey), whose radius is smaller than the cavity radius, and the structural PECVD Silicon Nitride (in green). The transducer elements are visible between the nodes of the lower surface of the top electrode and the nodes of the upper surface of the bottom electrode, covering an area equal to the area of the bottom electrode (the smaller between the two).

This electromechanically coupled model can be used to simulate the static performance of the CMUT array. The bias voltage value can be varied in order to observe the consequent variation of the mechanical and electrical impedance centre frequency (*spring-softening* effect), the membrane displacement profile due to the varying electrostatic force and the resulting static capacitance, as well as to study the coupling efficiency.

The investigation of the dynamic performance of the array requires the addition of the propagation fluid acoustically coupled to the transducer. An axisymmetric representation of the cylindrical fluid waveguide can be done by meshing a rectangular area with FLUID29 elements. In particular, a first layer of fluid must be meshed by specifying that the elements are in contact with a solid surface, by selecting a proper keyoption. The second layer into which the propagation of the acoustic signals takes place can eventually be meshed with larger elements, as accurate results require that the mesh should include at least 10 elements per wavelength. This mesh size was chosen as one tenth of the smaller wavelength, based on the longitudinal propagation velocity of acoustic waves in water and the maximum frequency of interest. In this way, the lower nodes number makes the model even lighter by reducing the DOFs count, thus making the simulation even faster. The layers with different mesh sizes must be coupled by imposing a constraint equation of continuity of the pressure degree of freedom (PRES).

Since the fluid column is surrounded by vacuum, the rigid walls work as a perfect reflector. As plane waves with a wavefront orthogonal to the radiating surface impinge on the farthest edge of the fluid waveguide, they are reflected towards the transducer. This allows the simulation of the pulse-echo behaviour of the device in the time-domain. To consider only the transmission operation, an absorbing boundary must be placed on the edge of the fluid column.

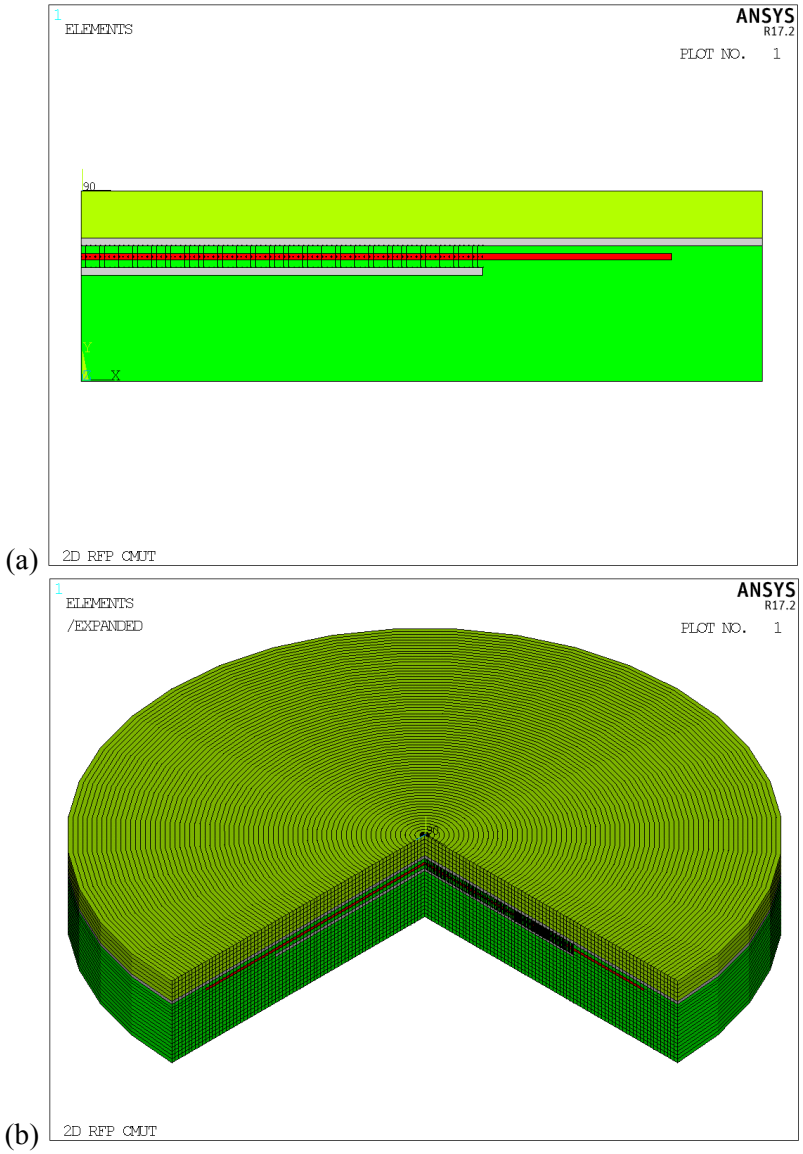

Figure II.2 *The 2D axisymmetric ANSYS model of a RF-CMUT cell in (a) an unmeshed 2D view and (b) a meshed 3/4 expansion showing the equivalent 3D structure.*

There are several ways to implement an absorbing boundary in ANSYS. The simplest method is the placement of surface impedance boundary conditions, and this is the method applied to this unbounded transducer model. It requires the attribution of an acoustic impedance to the elements placed at the further edge of the fluid column, in order to damp the acoustic pressure on the boundary. Another method involves the use of second-order absorbing

elements, applied on top of the boundary elements and meshed by their same pattern. In 2D models, the absorbing boundary should be a circular area on top of the fluid column; in 3D models, it should be a spherical surface centred at the origin. This method was applied to the sparse array element model described in the next section. The last method involves the use of Perfectly Matched Layers (PML), which are layers of pressure-absorbing elements made of an artificial material, transparent to pressure waves but extremely lossy. The thickness of the PML region can be increased to improve absorption. This method is frequently used when the acoustic source must be encapsulated into a surrounding medium. In this model, the absorbing of plane waves was performed by assigning an appropriate acoustic impedance to material assigned to the fluid elements placed on the last section of the propagation fluid.

By increasing the frequency, plane waves propagate with an increased angle θ with respect to the direction normal to the transducer surface because of the diffraction phenomenon. Therefore, the wavefronts are not parallel to the absorbing boundary, which does not work properly anymore. In this case, the reflection from the boundary, as well as from the side walls of the waveguide, originates stationary waves that compromise the transmitted pressure results. For this reason, the model is only effective until the absorbing boundary is working as expected.

The nodes at the interface between the transducer and the fluid were selected to activate the ANSYS flag for Fluid-Structural Interaction (FSI), in order to enable the coupling of the structural displacements (UX, UY) of the PLANE42 elements to the pressure degree of freedom (PRES) of the FLUID29 elements.

Figure II.3 shows the 2D axisymmetric model of the transducer coupled to the propagating medium. On top of the previously described electromechanically coupled model of the device structure, the layers representing the fluid medium can be seen. In particular, starting from the device surface, on top of which the FSI flag is activated, there is the first layer of contact fluid (in blue) and the first layer of propagation fluid (in light blue). Further, the longest fluid layer (in cyan) is the propagation fluid meshed with larger elements: the application of the constraint equation of continuity of the pressure DOF between the differently meshed layers is visible in magenta. Finally, the last fluid layer (in light blue-green) represents the absorbing boundary that prevents the reflection of acoustic plane waves at the end of the fluid waveguide length. The application of symmetry boundary conditions at the lateral edges of the structure can be recognized by the blue triangles pointing at the nodes on the left and right side of the structure; the same triangles pointing at the nodes on the bottom surface of the structure represent the clamped substrate boundary condition. In Figure II.3 (a) the model can be seen, unmeshed, in the *x-y* plane. Figure II.3 (b) shows the meshed 3/4 axisymmetric expansion of the model. Since the RF-CMUTs can be supported

by arbitrarily designed backing layers, the backing layer effect on the device performance can be taken into account by adding another layer under the SiN base, meshed by PLANE42 elements and having the mechanical properties of the acoustic backing.

(a)

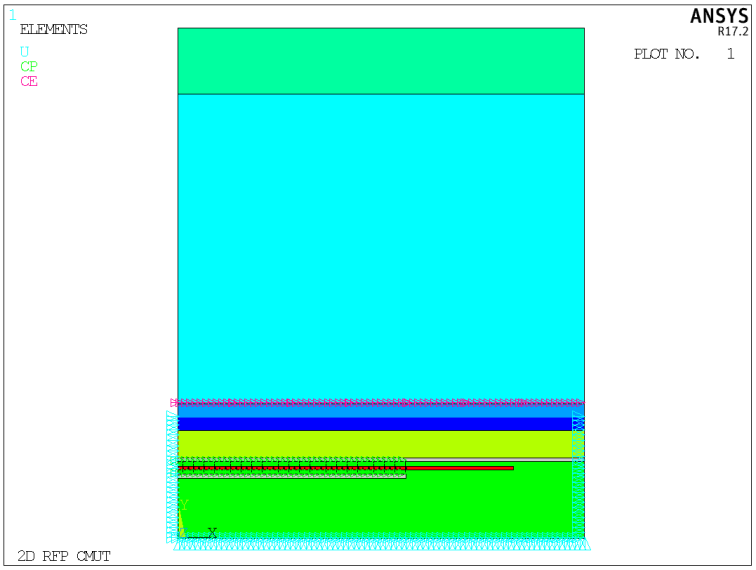

(b)

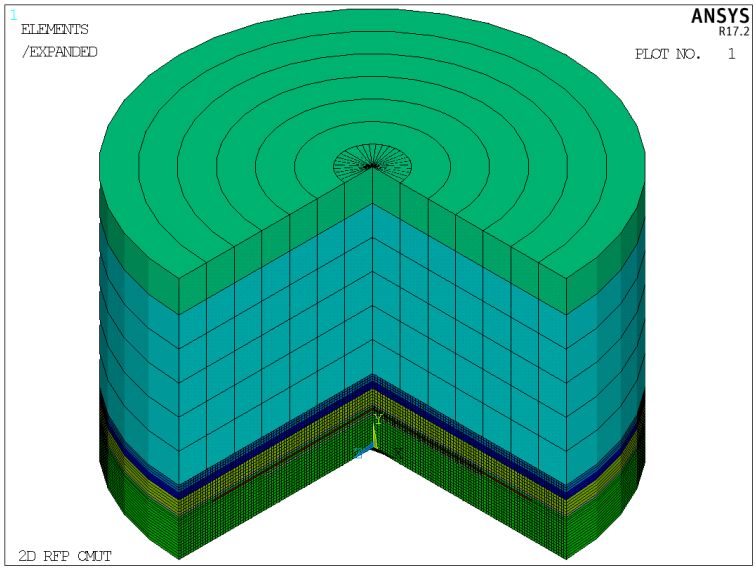

Figure II.3 *The 2D axisymmetric ANSYS model of a RF-CMUT cell with the propagating fluid coupled to the structural model in (a) an unmeshed 2D view and (b) a meshed 3/4 expansion showing the equivalent 3D structure.*

II.2.2 3D model in ANSYS

Finite Element Analysis of 3D electromechanical transducers coupled to an acoustic fluid is a very time-consuming operation. The degree of refinement of the mesh applied to the device model determines the results accuracy and the models complexity. A very fine meshing process returns models with a very high number of DOFs, which are very accurate but require a very long simulation time and a high-performing hardware. A coarse mesh originates very light model, which run very fast but can also turn insufficiently precise. In order to obtain correct results in a reasonable simulation time, the model should be the lightest model that gives adequate results accuracy.

The simulation of an array element of finite dimensions is much more computationally burdensome than the simulation of the unbounded transducer. For this reason, the mesh size for the simulation of the Fermat's spiral based sparse array was firstly determined by means of an infinite transducer model. The mesh degree of refinement was optimized by comparing results obtained with the 3D model of the unbounded transducer with results obtained by a 2D axisymmetric model, already validated by comparison with experiments. In this way, a trade-off between the results correctness and the computational burden was found.

The 3D model of the infinite transducer was obtained by applying symmetry boundary condition at the lateral edges of the model of the spatial period of a dense array of circular cells. The ANSYS script allows the choice of a square tiling of the cells as well as a hexagonal tiling. This latter arrangement, where the membranes are centred in the vertexes of an hexagon, is the one that provides the highest fill factor, hence maximizes the active area per unit area, thus improving the array sensitivity in both transmit and receive mode.

Figure II.4 shows the modelling of the volumes of the spatial period of a reverse fabricated CMUT dense array of circular cells. The model in Figure II.4 (a) represents a quarter of a circular cell, inscribed in a square area, whose replication in both direction leads to an infinite repetition of square tiled identical cells. The model in Figure II.4 (b) represents two quarters of two different circular cells, shifted with respect to one another in a way that the replication of the structure results in a repetition of hexagonally tiled identical cells. The volumes shown in Figure II.4 are the structural PECVD SiN in green, the LPCVD SiN membrane in light green, the Aluminium electrodes in grey and the cavity in red. The bigger circumference arch delimits the cavity area, hence the surface of the vibrating membrane; the smaller circumference arch represents the bottom electrode area, hence the area that determines the static capacitance.

The structural model of the device was meshed by tetrahedral elements, such as SOLID187. SOLID187 is a higher order 10-nodes element, with quadratic displacement behaviour, for the meshing of solids. Each node has 3

degrees of freedom, i.e. the nodal translations in the *x*, *y*, and *z* directions (UX, UY, UZ). A regular structure such as the one presented in Figure II.4 could be effectively meshed by reduced order elements with linear displacements, such as SLOID185. On the contrary, SOLID187 is particularly suited for the meshing of irregular solid structures, such as structures with holes or sharp edges, imported by a CAD model. This will be the case of the sparse array element model. Therefore, the mesh optimization process was carried out on this type of element. The meshing operation was performed by partitioning the lines according to a specified size, which therefore determines the tetrahedrons side dimension.

The electromechanical coupling was enabled by TRANS126 elements, the transducer elements previously defined in the 2D axisymmetric model description. In order to lay the transducer elements along the *z*-direction, the meshing of the electrodes surface had to be identical. For this reason, the meshing was performed starting from the bottom area; the area meshing was then copied on every other surface by sweeping the volumes from bottom to top.

The model was completed with the propagating fluid and the backing layer. Figure II.5 shows the meshed model of the RF-CMUT array composed of (a) the square tiled and (b) the hexagonally tiled circular membranes, including the fluid (cyan) and the backing (purple). The fluid was included as a rigid-walled rectangular waveguide, meshed with the FLUID30 elements, forced in a tetrahedral shape. As for the 2D model, the fluid thickness includes a layer of fluid in contact with the transducer structure. The nodes at the interface are selected to apply the ANSYS fluid-structure interaction flag, which couples the structural displacements with the fluid pressure DOF. The propagating fluid can be meshed with a coarse mesh without impairing the accuracy of the results, hence the mesh size was chosen equal to one tenth of the smallest wavelength, computed as the ratio between the acoustic wave velocity in the fluid medium and the maximum frequency of interest. The top layer of the fluid column was attributed an acoustic impedance necessary to obtain an absorbing boundary for the plane waves propagating in the fluid. In this way, reflection from the boundary is prevented in the frequency range considered. The backing was meshed with SOLID187 tetrahedrons, and the reflection of waves from the lower boundary was avoided by placing SURF154 elements on the bottom surface of the acoustic backing.

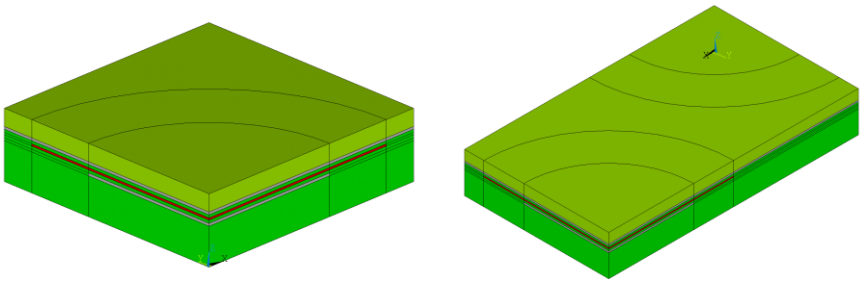

(a) (b)

Figure II.4 *The modelling of the volumes of the spatial period of an RF-CMUT array composed of circular membranes arranged by (a) square tiling and (b) hexagonal tiling.*

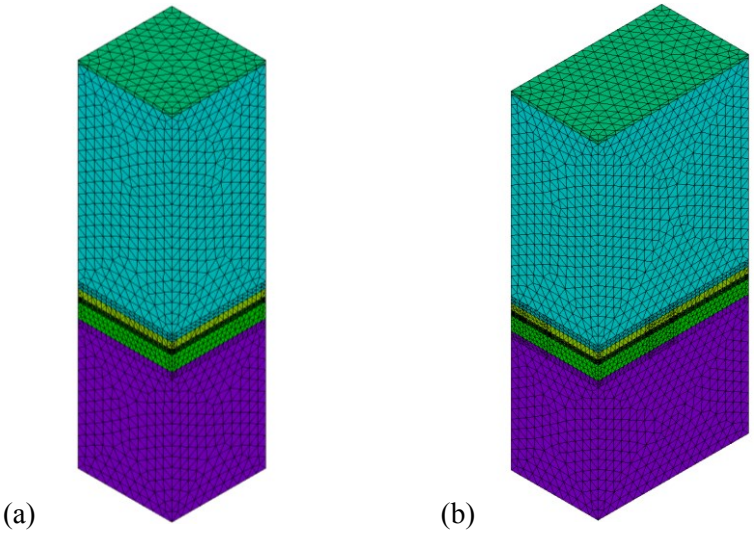

(a) (b)

Figure II.5 *The 3D ANSYS model of the spatial period of RF-CMUT array of circular cells arranged by (a) square tiling and (b) hexagonal tiling. The model includes the propagating fluid coupled to the structural model and the acoustic backing below the transducer device.*

II.3 Mesh optimization process

The element size used to mesh the model strongly affects the accuracy of the results and the simulation time. In order to determine a mesh size that would grant an adequate trade-off between the results accuracy and the simulation time, the first mode frequency computed by varying the tetrahedral elements size was compared to the one obtained by the 2D axisymmetric

model of the same device. The considered device has the geometrical parameters listed in Table II.1.

Table II.1 *Geometrical parameters of the modelled RF-CMUT device*

Lateral dimensions [μm]		Thicknesses [μm]	
Membrane pitch	57.7	Membrane	2
Membrane diameter	50	Gap	0.25
Electrode diameter	34	Electrodes	0.3
		Passivation layers	0.35
		Base	4.5

The structure used for this mesh optimization process was the configuration with circular membranes arranged by hexagonal tiling. In order to keep unaltered the ratio of the inactive area with respect to the active vibrating surface, the pitch dimension of the 2D axisymmetric model was corrected to take into account the different shape. As can be seen in Figure II.6 (a), the axisymmetric model represents a circular structure with a radius equal to half the membrane pitch p (centre-to-centre distance), whereas the 3D model describes two membrane quarters arranged in a rectangular surface, as shown in Figure II.6 (b). In the considered section, the short side is $l_y = p/2$, and the long side is $l_x = p \sin(60°)$, and the surface including one membrane is twice the area of the rectangle in Figure II.6 (b). Therefore, in order to have the same amount of inactive area around one membrane, the axisymmetric model should have an equivalent pitch l_{eq} that equals the areas as in eq. (II.1).

$$\pi \frac{l_{eq}^{\,2}}{4} = 2\frac{\sqrt{3}}{4} p^2 \tag{II.1}$$

hence

$$l_{eq} = \sqrt{\frac{2\sqrt{3}}{\pi}} p = 1.050075\, p \tag{II.2}$$

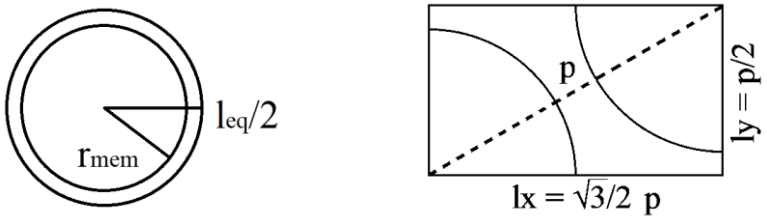

Figure II.6 *The geometry modelled by (a) the axisymmetric model and (b) the 3D model of the hexagonally tiled membranes.*

The result of the modal analysis performed on the 2D model with the corrected pitch value returned a first mode mechanical resonance frequency of f_{m0} = 13.066 MHz. The results obtained by varying the mesh size of the 3D model are shown in Figure II.7. It can be seen that a coarse mesh causes the effect of an increased stiffness, which determines an overestimation of the resonance frequency of the structure. On the contrary, a very fine mesh has the effect to create a more elastic structure, since the nodes able to move are closer to each other. Results comparable to those obtained with the 2D model, which was already validated by experimental measurements, can be obtained with a 1.1 μm mesh size.

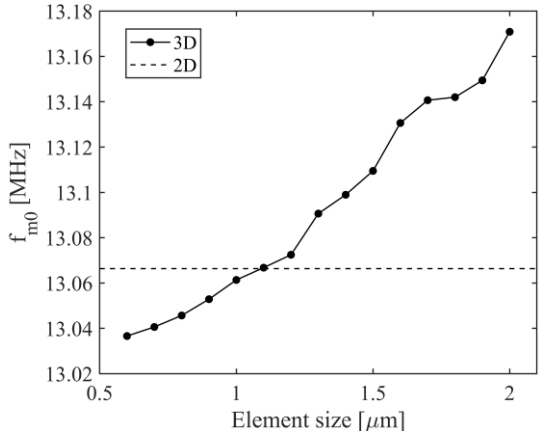

Figure II.7 *The first mode mechanical resonance frequency for the RF-CMUT device described in Table II.1, computed by performing the modal analysis on the 3D model by varying the meshing elements size. The dashed line represents the result obtained by using the 2D axisymmetric model of the same device.*

As the mesh size was reduced, the computation time increased from about 1 minute to almost 1 hour. The simulation time depends on the model complexity, and reducing the mesh size increases the model size (the number of equations to solve) in a nonlinear way. This is clearly shown in Figure II.8. In particular, it can be noticed that the increase of the total equation count in response to a 0.1 μm reduction of the elements size is much steeper when the mesh size is reduced below 1 μm.

The first mode frequency was then plotted against the model size in Figure II.9. As can be seen, increasing the model complexity leads to a convergence towards a modal frequency value slightly lower than the one obtained with the 2D model. Further increasing the refinement would not improve the accuracy considerably, but it would prolong the time required for the simulation in a substantial way. A lighter model overestimates the resonance frequency, but a small increase of the complexity results in a significant improvement in the accuracy of the returned value.

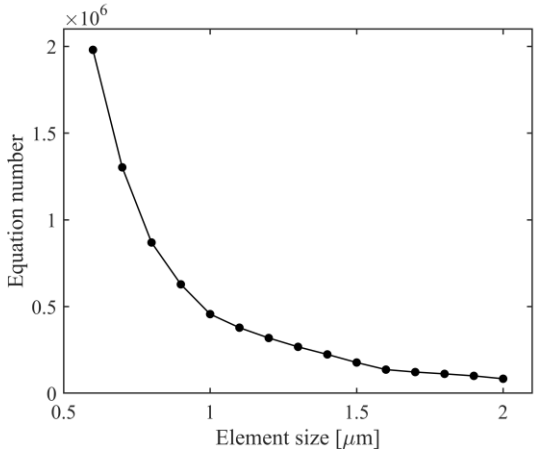

Figure II.8 *The model complexity, described by the equation count, for different mesh sizes applied to the 3D model of the RF-CMUT described in Table II.1.*

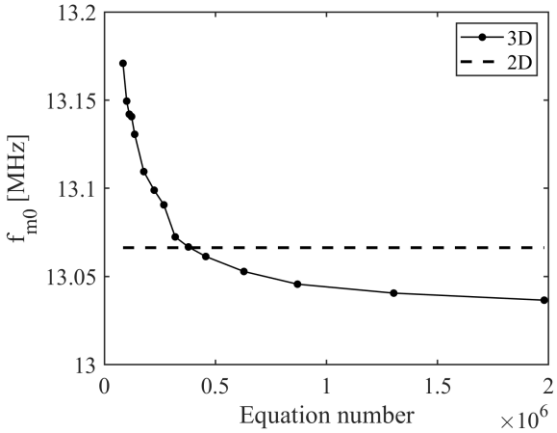

Figure II.9 *The first mechanical resonance frequency plotted against the model total equation count.*

Due to the long simulation time required to perform a simple modal analysis on the structural model, the effects of the mesh refinement were observed on the results of a harmonic analysis performed to compute the mechanical impedance of the device. A uniform pressure was applied on the surface of the transducer, and the resulting average nodal displacement along the *z*-axis of the same surface was used to compute the average surface normal velocity. The mechanical impedance was computed as the ratio between the pressure and the normal velocity in the frequency domain.

Figure II.10 shows the mechanical impedance computed by varying the mesh size on the 3D model of the device described by the parameters in Table II.1. It is clear that the mechanical impedance shows very small differences

even by increasing considerably the model complexity. For this reason, it was observed that, for the simulation of the considered device, the steep increase of the simulation time would not be worth the improvement in terms of accuracy of the results. Then, an element size of 1.5 μm was considered a good trade-off between the model complexity and the time needed to obtain the desired results.

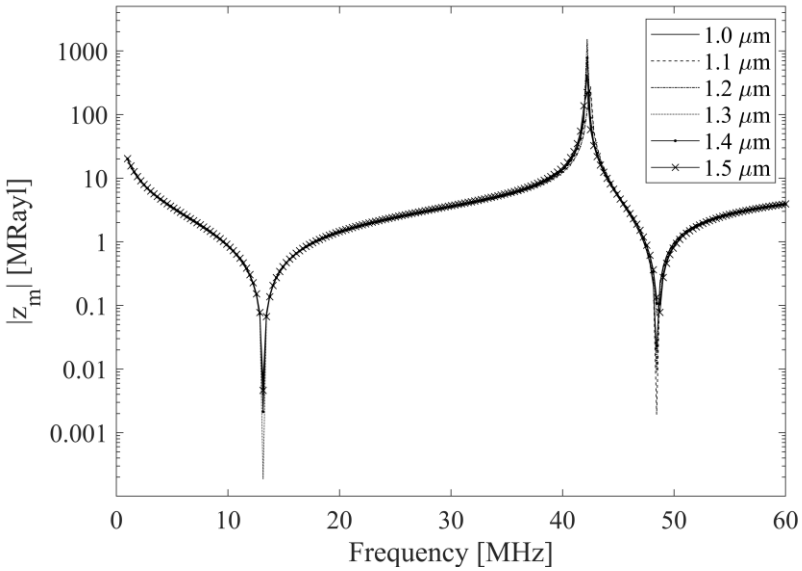

Figure II.10 *Comparison between the mechanical impedance curves computed by varying the mesh size.*

II.4 FEM Model validation

In order to prove the model effectiveness, experimental measurements on single-element RF-CMUT devices were performed at the Aculab, Roma Tre University. The accuracy of the mechanical coupling to the backing and of the acoustic coupling to the propagation fluid was tested by measuring the electrical impedance and transmission transfer function of two devices provided with backings of different acoustic impedance. The first device has a backing made of epoxy resin Epotek 301 enriched by 11% Al_2O_3 and 11% W powders; the second device has a backing made of Epotek 301 enriched by 22% Al_2O_3 powder. The two devices lateral and vertical dimensions are reported in Table II.2.

Table II.2 *Geometrical parameters of the simulated and measured devices*

Lateral dimensions [µm]		Thicknesses [µm]	
Membrane pitch	33	Membrane	1
Membrane diameter	29.6	Top electrode	0.2
Electrode diameter	20	Top passivation	0.35
		Gap	0.2
		Bottom passivation	0.3
		Bottom electrode	0.3
		Base	4.5

Figures II.11 and II.12 show the comparison between the simulated and measured real part and imaginary part of the electrical impedance of the considered devices. Simulations and measurements were carried out by varying the bias voltage. For both devices, the model well represents the resonance frequency variation in response to the bias voltage variation caused by the *spring-softening effect*.

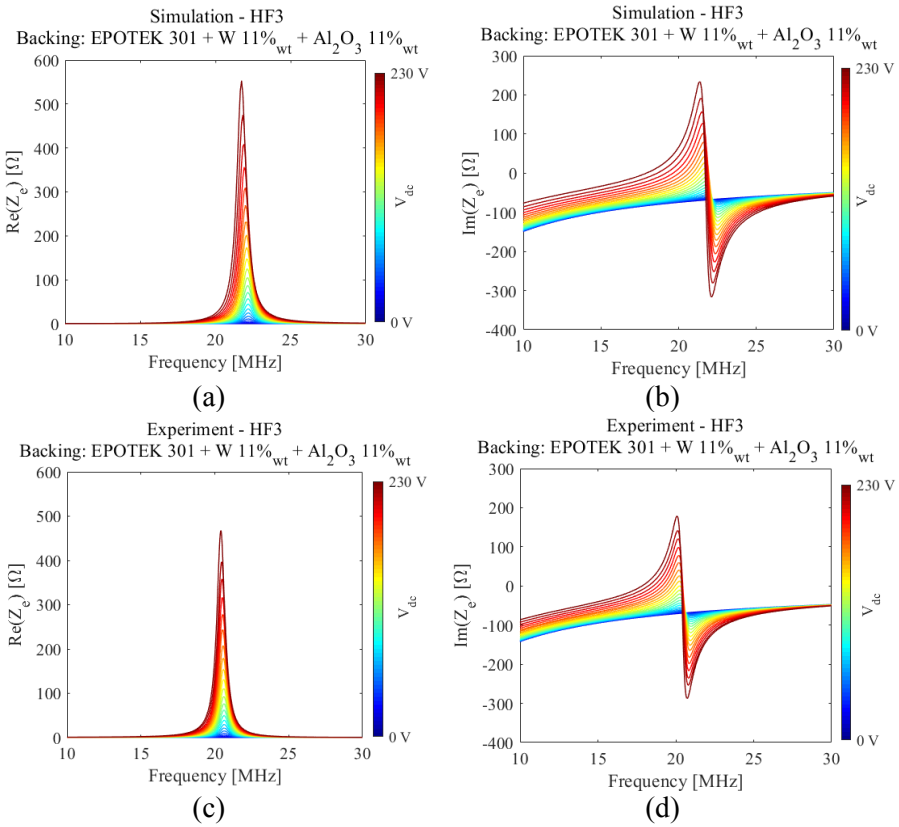

Figure II.11 *Electrical impedance simulated (a) real part and (b) imaginary part compared to the measured (c) real part and (d) imaginary part of the 1st device. Simulations and measures were performed by varying the bias voltage.*

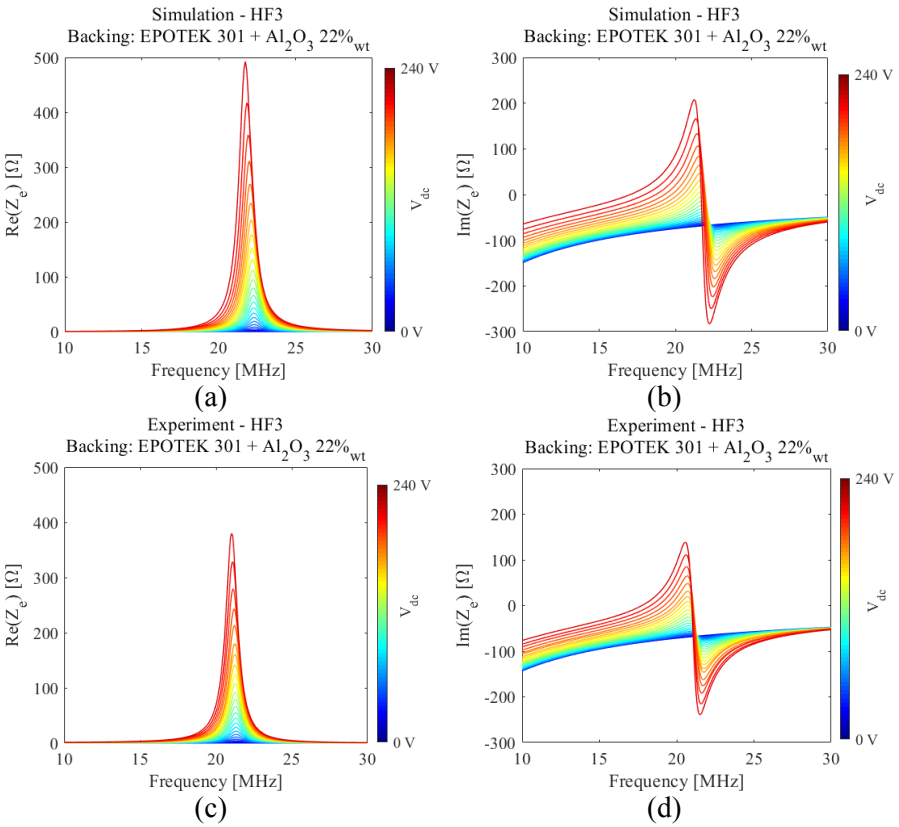

Figure II.12 *Electrical impedance simulated (a) real part and (b) imaginary part compared to the measured (c) real part and (d) imaginary part of the 2nd device. Simulations and measures were performed by varying the bias voltage.*

The FEM model was used to simulate the RFP-CMUT device behaviour in water-coupled conditions by performing a coupled-field electro-acoustic analysis under small-load approximation. By means of ANSYS harmonic analysis, the transmission sensitivity was computed for both devices and compared to the measured impulse response. The transmission sensitivity was simulated by biasing the transducer at $V_{dc} = 0.9\ V_{coll}$, with $V_{coll} = 268$ V. The collapse voltage value was computed by repeating a nonlinear static analysis for increasing values of the bias voltage, until the returned gap height was non-positive. The measurement of the transmission impulse response was performed by exciting the devices with a -16 V, 8 ns voltage pulse, and by measuring the transmitted pressure by means of a hydrophone at an on-axis distance of 7.5 mm. Figure II.13 compares the simulated transmission frequency response of the device (a) with the measured impulse response (b). Due to the different nature of the transfer functions, the curves in Figure II.13 cannot be compared on their amplitude values. What can be verified by

observing the curves is the second mode resonance frequency in immersion operation, which is correctly predicted by the model.

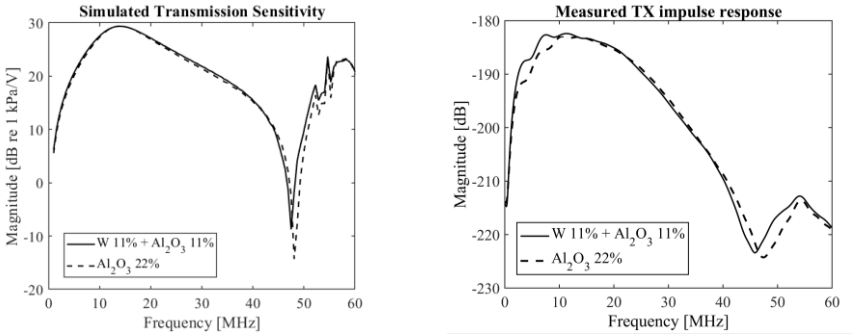

(a) (b)

Figure II.13 *Comparison between (a) the simulated transmission transfer function and (b) the measured impulse response for both the described devices.*

These measurements prove that the model successfully predicts the electrical and acoustic behaviour of wide aperture CMUT devices.

II.5 The sparse array element model

A CMUT sparse array element is usually a quite complex structure. Sometimes a more straightforward approach to create the FEM model is to build up a CAD model using dedicated software, and then import it in ANSYS. In this way, the FEM model can be made from the structural design.

A CAD model of an RF-CMUT sparse array element was made in AutoCAD Mechanical 2016 (Autodesk Inc., San Rafael, CA, USA), and then the design was transferred to ANSYS. The FEM model was made by meshing the volumes according to the mesh sizing results obtained in the previous section, because the membranes geometry is very close to the one described in Table II.1.

The reference design is the 256-elements RF-CMUT sparse array designed for wideband operation around 7 MHz in immersion, part of a multi-module chip described in [64]. This device is made of 256 elements, arranged according to a Fermat's spiral having the divergence angle equal to the so-called *golden angle*. The elements spatial density is modulated by a tapering function, as described in [66]. The array layout is shown in Figure II.14 (a). Each element is composed of 19 circular cells packed by hexagonal tiling, as shown in Figure II.14 (b). Each membrane has a diameter of 48 μm, and the membrane pitch is 53 μm (the kerf is 5 μm). The quasi-circular area of the array element can be described by an effective radius of about r_{eff} = 220 μm, hence, the element aperture expressed in terms of λ is a = λ. The array is

interfaced with an ASIC, which performs the required operations for the μ-beamforming, by means of the packaging technique described in [64]. For this reason, the array radiative performance was studied by considering the device both clamped and supported by a thin layer of Benzocyclobutene (BCB), representing the layer bonding the transducer with the ASIC.

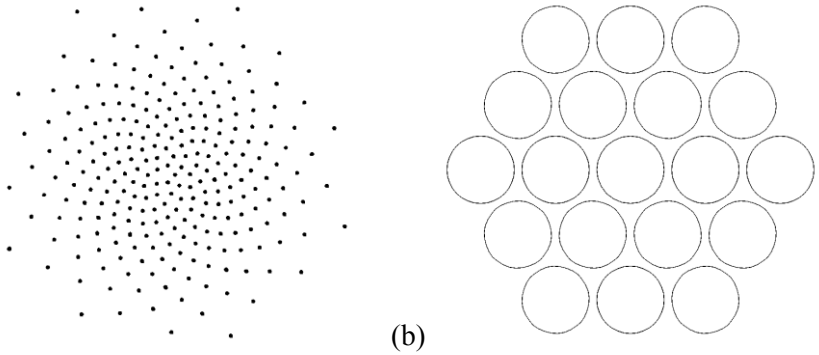

Figure II.14 *The investigated 256-elements RF-CMUT sparse array with a Fermat's spiral-based layout. (a) The elements spatial arrangement and (b) the membrane pattern of each element.*

II.5.1 The device model in AutoCAD®

The CAD model of the sparse array element was built taking advantage of the symmetry of the structure. An angular sector of 30° was modelled in AutoCAD and imported in ANSYS, where symmetry boundary conditions were applied to simulate the entire element. Figure II.15 (a) shows an x-rays view of the 30° sector of the array element modelled in AutoCAD; a side view of the model is shown in Figure II.15 (b). The membrane is in yellow-green, the structural Silicon Nitride is in green, the electrodes are in grey and the cavities in red.

The geometric parameters of the RF-CMUT cells are listed in Table II.3.

Table II.3 *Geometrical parameters of the RF-CMUT cells composing the sparse array element*

Lateral dimensions [μm]		Thicknesses [μm]	
Membrane pitch	53	Membrane	2
Membrane diameter	48	Gap	0.2
Electrode diameter	34	Electrodes	0.3
		Passivation layers	0.35
		Base	2.5
		BCB layer	12

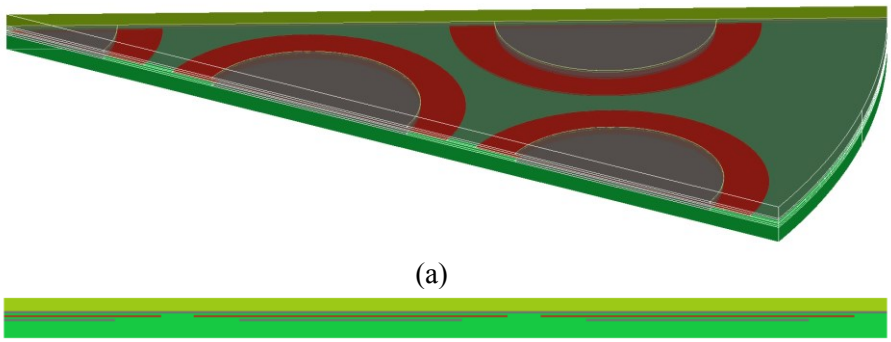

(a)

(b)

Figure II.15 *The model of a 30° sector of the sparse array element modelled in AutoCAD, (a) in an x-rays view and (b) in a side view.*

In order to obtain the acoustic radiation pattern, the device was coupled to a sphere of propagating fluid centred in the array central point, as shown in Figure II.16.

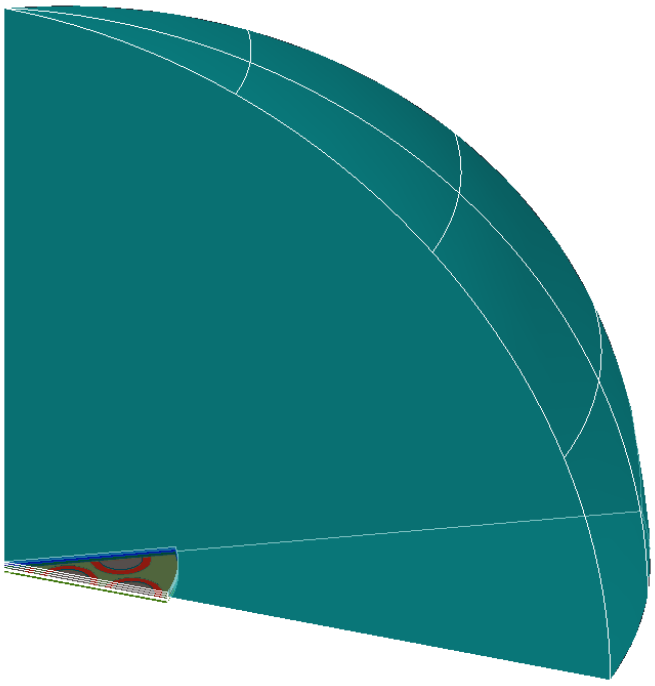

Figure II.16 *An x-rays view of the 30° sector of the sparse array element modelled in AutoCAD.*

To study the variation of the beam pattern caused by the coupling with the ASIC by means of the BCB layer, the model with the fluid coupled to the transducer was also provided with the underlying BCB layer.

II.5.2 The device model in ANSYS®

The model of the sparse array element was imported in ANSYS to perform a finite element analysis. The BCB underfill was also included in the structural model. The structure of the device was meshed with SOLID187 elements, the 10-nodes tetrahedral elements used in the mesh optimization analysis described in Section II.3. The fluid was meshed with higher order tetrahedral elements, the 20-node FLUID221, in order to fit better the fluid sphere layout. The absorbing boundary for the acoustic waves was realized by laying FLUID130 absorbing elements on the outer surface of the fluid sphere. The electromechanical coupling was included by placing TRANS126 elements across the electrodes of the membranes of the array element. The nodal displacements at the side surfaces of the 30° sector model were clamped, in order to simulate the behaviour of a repeated structure having the periodical pattern of the circular element. Different boundary conditions were applied to the side surface nodes of the Silicon Nitride and the BCB layer, in order to test the feasibility of acoustic isolation of the array elements. The presence of the ASIC under the BCB layer was taken into account by clamping the nodes of the bottom surface, since it is a 700 μm thick layer of Silicon.

Chapter III
Electroacoustic performance of RF-CMUT devices

III.1 FEA-based CMUT design tool

A design tool for the simulation of wide aperture RF-CMUT multicell devices, based on the 2D axisymmetric finite element model described in Chapter II, was developed.

The ANSYS code is designed to receive an input file containing information about whether the user requests the inclusion of the backing, the electromechanical coupling and the fluid in the analysis. The input text file also includes the geometrical parameters of the device, so that any structure based on an array of circular cells can be simulated by means of the same code. A MATLAB (The Mathworks Inc, Natick, MA) script writes the input text file according to the data provided by the user, then runs ANSYS by means of a batch file. By including the launcher in a loop, several simulations with different parameters can be performed by one MATLAB script. This integrated environment allows the evaluation of the CMUT characteristics in relation to the physical dimensions of the device, thus representing a valuable tool supporting the design process.

In this chapter, the results of the static and dynamic characterization of dense arrays of reverse fabricated CMUTs are described. The first resonance frequency and the collapse voltage value are studied by varying the device geometrical parameters, and the electrical properties and transfer functions in transmission and reception operation are investigated by varying the bias voltage and the backing material.

The nominal values of the geometrical parameters of the studied device and the considered variation range of the lateral and vertical dimensions are listed in Table III.1.

Table III.2 includes the material properties used in the simulations: the LPCVD Silicon Nitride is the membrane material, the PECVD Silicon Nitride is the structural material and Aluminium is the material of the electrodes. In

order to simulate the behaviour of the device coupled to the human body, the load has the material properties of water.

Table III.1 *Geometrical parameters of the simulated device and their variation range*

Lateral dimensions [μm]			Thicknesses [μm]		
	Nominal values	Variation range		Nominal values	Variation range
Membrane pitch	57.7	46.2 – 115.4	Membrane	2	1 – 2
Membrane radius	25	20 – 50	Gap	0.25	0.1 – 0.3
Electrode radius	17	13.6 – 34	Electrodes	0.3	
			Passivation layers	0.35	
			Base	4.5	
			Backing	1000	
			Fluid	1000	

Table III.2 *Material parameters used in the simulations*

	Young's modulus [GPa]	Poisson ratio	Density [kg/m^3]	Relative permittivity	Longitudinal velocity [m/s]
LPCVD SiN	180	0.25	3000		
PECVD SiN	150	0.25	2600	7	
Aluminium	70	0.33	2700		
Fluid (water)			1000		1500

III.2 Structural analysis

The first step for the design of an ultrasonic transducer is the design of the CMUT cell geometry according to the desired operating frequency. In fact, the bandwidth of the transmission and reception transfer function spreads around the frequency of the first resonant mode of the structure, which is determined by the lateral and vertical dimensions of a CMUT cell, together with the mechanical properties of the materials used for the fabrication of the device. The *n*-th mode frequency of a membrane with fixed rim is given by [87], [89]

$$f_n = \frac{\alpha_n}{2\pi r_m^2}\sqrt{\frac{D}{\rho_m t_m}} \tag{III.1}$$

where α_n has tabled values depending on the mode number, r_m is the membrane radius, t_m is the membrane thickness, ρ_m is the membrane volume density and D is the plate flexural rigidity, defined as

$$D = \frac{Y_m t_m^3}{12\left(1-\nu_m^{\,2}\right)} \tag{III.2}$$

with Y_m Young's modulus and ν_m Poisson's number of the membrane material.

The analytical equation of the resonant modes of a plate, eq. (III.1), relies on the assumption of a perfectly clamped boundary, and does not take into account the presence of multiple layers of different materials, unless an equivalent Young's modulus and Poisson's number are used in eq. (III.2). Finite element analysis, on the contrary, can consider the exact geometry and mechanical properties of the structure.

III.2.1 Resonant modes of the circular membrane

In the case of circular membranes with circular electrodes, only axisymmetric modes of the thin plate can be excited. Figure III.1 shows the first three modal shapes of the CMUT having the dimensions reported in Table III.1, resulting from a modal analysis performed on the ANSYS FEM model described in Section II.2.1. The frequencies of the first three axisymmetric modes are f_{m0} = 13.13 MHz, f_{m1} = 48.45 MHz, f_{m2} = 100.70 MHz.

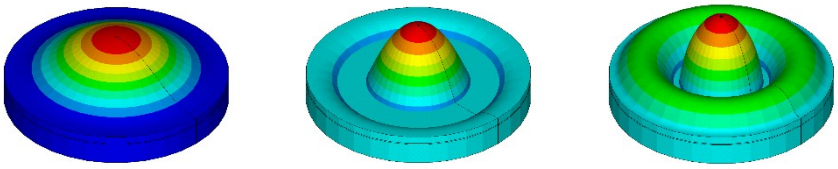

(a) (b) (c)

Figure III.1 *The modal shapes of the RF-CMUT membrane (a) at the first, (b) at the second and (c) at the third resonant mode frequency, computed by the modal analysis (ANSYS). The colours represent the displacement along the direction normal to the radiating surface plane, ranging from the minimum (blue) to the maximum (red).*

III.2.2 Mechanical impedance in vacuum of the circular membrane

The frequencies of the membrane axisymmetric modes match the frequencies of the mechanical impedance minima. The membrane vibration at the first resonant mode frequency effectively generates acoustic waves, since

the average displacement is significant. As higher modes are excited, positive and negative displacements across the radiating surface compensate, resulting in an almost null average displacement and drastically impairing the transmission efficiency. For this reason, the transfer function bandwidth spreads around the first mode frequency, i.e. the first minimum of the mechanical impedance. The wider the range of frequency where the mechanical impedance of the device in vacuum is lower than the mechanical impedance of the propagating medium, the wider will be the bandwidth of the coupled device transfer function. For this reason, the study of the mechanical impedance of a device is usually the first approach for the design of broadband transducers.

Figure III.2 shows the mechanical impedance in vacuum of the RF-CMUT device with the nominal values of the geometric parameters listed in Table III.1. The harmonic analysis, run on the model described in Section II.2.1 by using the FEM software ANSYS, returns a first resonance frequency at f_0 = 13.11 MHz and a second resonance frequency at f_1 = 48.42 MHz, in agreement with the modal analysis results (small inaccuracies are due to the frequency step size).

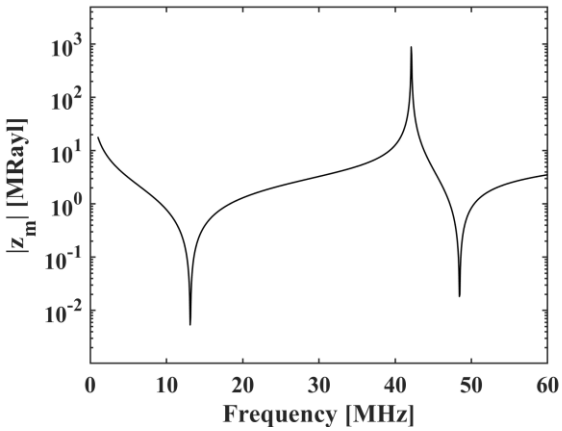

Figure III.2 *The mechanical impedance of the RF-CMUT device described in Table III.1, computed by a finite element harmonic analysis.*

III.2.3 First mode frequency dependence on the device geometry

The computation of the resonance frequency can be quickly performed by means of the modal analysis. The first resonance frequency of the RF-CMUT cell structure described in Table III.1 was computed by the modal analysis by varying the membrane radius r_m and thickness t_m. Eqs. (III.1) and (III.2) state that the first resonance frequency should decrease with the square of the radius, and increase linearly with the thickness. The effect of the cavity height

d, which cannot be evaluated by means of the analytical equation of the plate resonant modes, was also computed by FEA.

Figure III.3 shows the first axisymmetric mode frequency f_{m0} computed by means of the modal analysis by varying the membrane aperture. For this analysis, the membrane thickness and cavity height used were the nominal values of the considered RF-CMUT, i.e. t_m = 2 μm and d = 0.25 μm.

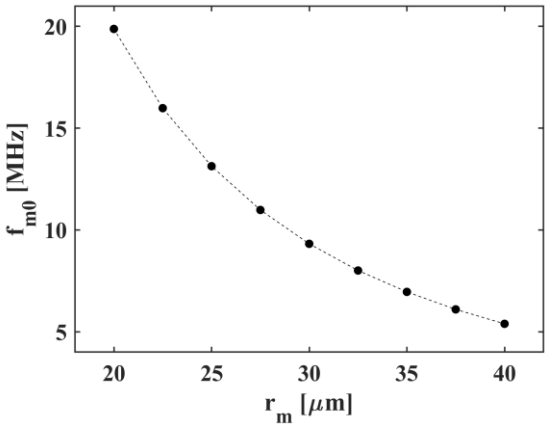

Figure III.3 *The first axisymmetric mode frequency of the RF-CMUT described in Table III.1 computed by varying the membrane radius, obtained by performing a modal analysis on the 2D axisymmetric FEM model (ANSYS).*

Figure III.4 shows the same quantity computed by varying the membrane thickness, when the membrane radius and cavity height equal the nominal values in Table III.1, i.e. r_m = 25 μm and d = 0.25 μm.

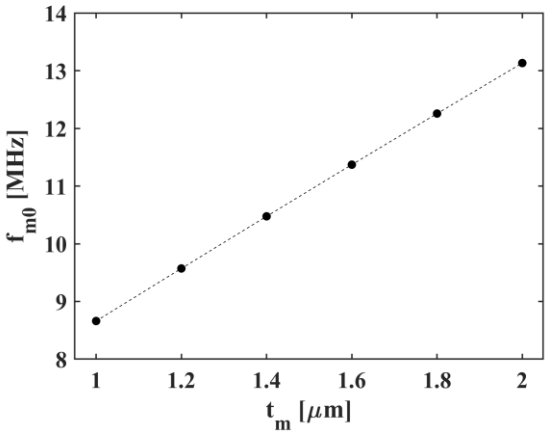

Figure III.4 *The first axisymmetric mode frequency of the RF-CMUT described in Table III.1 computed by varying the membrane thickness, obtained by performing a modal analysis on the 2D axisymmetric FEM model (ANSYS).*

The first modal frequency f_{m0} was also computed by varying the cavity height d. The results are shown in Figure III.5. As can be seen, the gap height affects the resonance frequency, which decreases by increasing the distance between the membrane and the substrate. This variation, though, is very small.

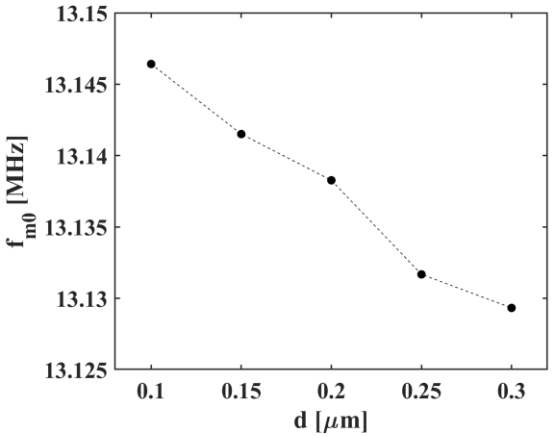

Figure III.5 *The first axisymmetric mode frequency of the RF-CMUT described in Table III.1 computed by varying the cavity height, obtained by performing a modal analysis on the 2D axisymmetric FEM model (ANSYS).*

This kind of analysis represents the first step for the design of CMUT devices, and leads to the definition of the cell structure depending on the operating frequency for the application of interest.

III.3 Static characterization

The FEM model includes the modelling of the electromechanical energy conversion by means of the transducer elements applied to the nodes of the electrodes surfaces. The voltage degree of freedom is coupled for all the nodes of the bottom surface of the top electrode, whose potential is set to ground, and for the nodes of the top surface of the bottom electrode, whose potential is set to the bias voltage V_{dc}. As the bias voltage is applied, an equilibrium condition is reached when the electrostatic force balances the elastic force that keeps the membrane deflected towards the substrate. Since the membrane rim is fixed, the centre undergoes the maximum displacement, which decreases along the radius until it becomes null at the fixed edge. The suspended plate deflection profile depends on its flexural rigidity (determined by the membrane material properties and the membrane geometrical parameters, such as the radius and thickness) as well as on the electrical boundary conditions, such as the bias voltage applied and the electrically active surface (the electrode area). The plate deflection as a function of the radial position $u(r)$ is found in the literature of basic plate theory [71], [90]

$$u(r) = \frac{P_0}{64D}\left(r_m^2 - r^2\right)^2 = u_{MAX}\left(1 - \frac{r^2}{r_m^2}\right)^2 \tag{III.3}$$

where P_0 is the uniform loading on the plate, r_m is the membrane radius and D is the flexural rigidity expressed in eq. (III.2); u_{MAX} is the peak deflection at the centre of the membrane

$$u_{MAX} = \frac{P_0 r_m^4}{64D} = \frac{P_0}{4Y_m}\frac{r_m^4}{t_m^3} \ . \tag{III.4}$$

The applied pressure depends on the electrostatic force by

$$P_0 = P_{atm} + \frac{F_{el}}{\pi r_m^2} \tag{III.5}$$

where F_{el} is not uniform across the membrane surface, due to the non-uniform displacement. In particular, it is maximum at the centre of the membrane, where the distance from the substrate is minimum. Nevertheless, as to consider a uniform loading, the electrostatic force can be computed by means of the average displacement of the membrane. The average membrane deflection u_{avg} is obtained by averaging the displacement over the membrane area

$$u_{avg} = \frac{1}{\pi r_m^2}\int_0^{2\pi}\int_0^{r_m} r\,u(r)\,dr\,d\phi = \frac{u_{MAX}}{3} \ . \tag{III.6}$$

Therefore, the electrostatic force F_{el}, which is defined as the first derivative of the energy stored in the capacitor, can be expressed by

$$F_{el} = \frac{d}{du_{avg}}\left[\frac{1}{2}C_0 V_{dc}^2\right] \tag{III.7}$$

where C_0 is the static capacitance of the CMUT cell [71]

$$C_0(r) = \int_0^{2\pi}\int_0^{r_m}\frac{\varepsilon_0 r}{d - u(r)}dr = \int_0^{r_m}\frac{2\pi\varepsilon_0 r}{d - u_{MAX}\left(1 - \frac{r^2}{r_m^2}\right)^2}dr \tag{III.8}$$

which depends on the average displacement by eq. (III.6):

$$C_0 = \frac{\varepsilon_0 \pi r_m^2}{\sqrt{d\, u_{MAX}}} \operatorname{arctanh}\left(\sqrt{\frac{u_{MAX}}{d}}\right) = \frac{\varepsilon_0 \pi r_m^2}{\sqrt{3d\, u_{avg}}} \operatorname{arctanh}\left(\sqrt{\frac{3u_{avg}}{d}}\right) . \quad \text{(III.9)}$$

It is important to notice that eq. (III.7) states that the higher the bias voltage, the higher the attraction between the electrodes. Therefore, by increasing the bias, the membrane deflects until the elastic force cannot balance the electrostatic force, and the membrane collapses onto the substrate starting from the centre.

Several models for the computation of the collapse voltage have been proposed [31], [71], [74], [91]. In particular, according to these models the collapse occurs when the membrane average displacement reaches approximately one third of the gap height. The collapse voltage value is given by

$$V_{coll} = \sqrt{\frac{8 k_m d^3}{27 \varepsilon_0 \pi r_m^2}} \quad \text{(III.10)}$$

where k_m represents the elastic spring constant of the membrane, which depends on the mechanical properties of the plate and is usually modelled by

$$k_m = \frac{192 \pi D}{r_m^2} = \frac{16 \pi Y_m t_m^3}{(1-\nu_m{}^2) r_m^2} . \quad \text{(III.11)}$$

Therefore, the collapse voltage V_{coll} varies as the inverse square of the radius, the square root of the cubic power of the thickness and of the gap height, as expressed by eq. (III.12):

$$V_{coll} = \sqrt{\frac{128 Y_m d^3 t_m^3}{27 \varepsilon_0 (1-\nu_m{}^2) r_m^4}} \quad \text{(III.12)}$$

III.3.1 Collapse voltage computation

Analytical models for the collapse voltage always rely on the computation of the average displacement of the membrane. The finite element analysis, instead, can take into account the suspended plate deflection profile, along with all the structural properties that cannot be easily included in the physical equations that describe the system. For this reason, the collapse voltage can be accurately predicted by FEA. Such study was performed by running a static analysis by progressively increasing the bias voltage. Due to the nonlinear dependence of the electrostatic force on the displacement, the static analysis is nonlinear, thus requires some iterations to converge. At the end of each converged analysis, the gap height was read on the applied transducer

elements. The bias voltage was increased with a step of 0.5 V until the gap height returned from the analysis was negative, which meant that the membrane had collapsed. At that point, the bias voltage that caused the collapse was stored.

The collapse voltage computed for the device described in Table III.1 with the described method was V_{coll} = 277 V. Figure III.6, 7 and 8 show the collapse voltage V_{coll} computed by varying the membrane geometrical parameters according to the values listed in Table III.1.

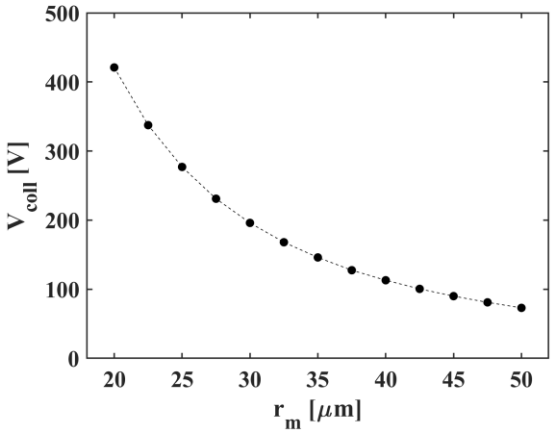

Figure III.6 *Collapse voltage value computed by a finite element nonlinear static analysis (ANSYS) by varying the membrane radius of the device described in Table III.1 from 20 μm to 50 μm.*

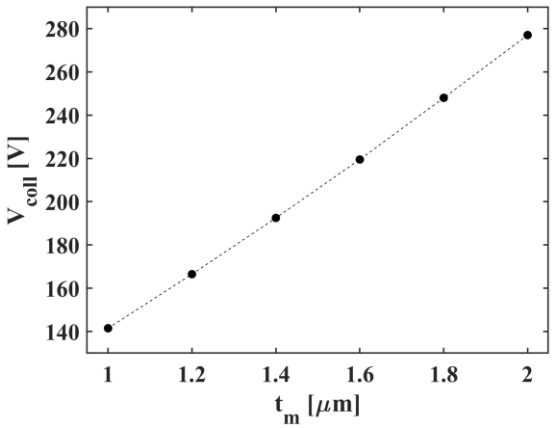

Figure III.7 *Collapse voltage value computed by a finite element nonlinear static analysis (ANSYS) by varying the membrane thickness of the device described in Table III.1 from 1 μm to 2 μm.*

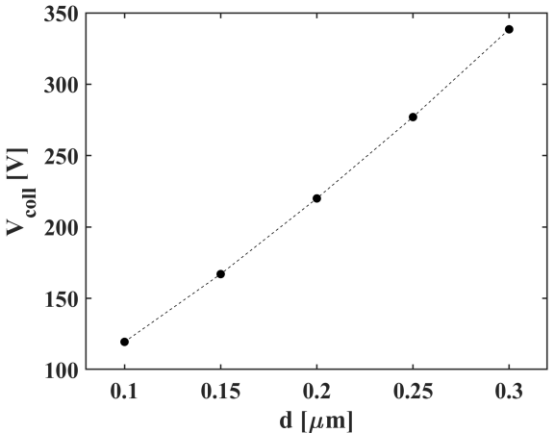

Figure III.8 *Collapse voltage value computed by a finite element nonlinear static analysis (ANSYS) by varying the cavity height of the device described in Table III.1 from 0.1 μm to 0.3 μm.*

III.3.2 Membrane deflection profile computation

A finite element static analysis can accurately predict the membrane shape at the equilibrium. The displacement along the *y*-axis UY, which is the direction normal to the transducer surface, can be read for each node of the membrane radius on the upper surface of the biased transducer.

Figure III.9 shows the membrane deflection profile computed by varying the bias voltage $V_{dc} = \alpha V_{coll}$, with $\alpha = 0.05 \div 0.95$, hence in the range $V_{dc} = 13.85 \div 263.15$ V. The device considered is the RF-CMUT with the nominal values of the geometrical parameters reported in Table III.1.

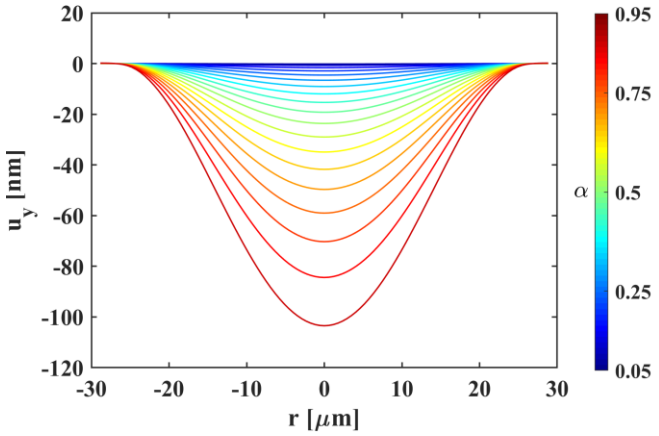

Figure III.9 *The membrane deflection profile computed by varying the bias voltage $V_{dc} = \alpha V_{coll}$, with α varying from α = 0.05 to α = 0.95.*

The amplitude of the maximum membrane displacement at the static equilibrium, observed at the centre of the plate and computed by varying the bias voltage, is shown in Figure III.10.

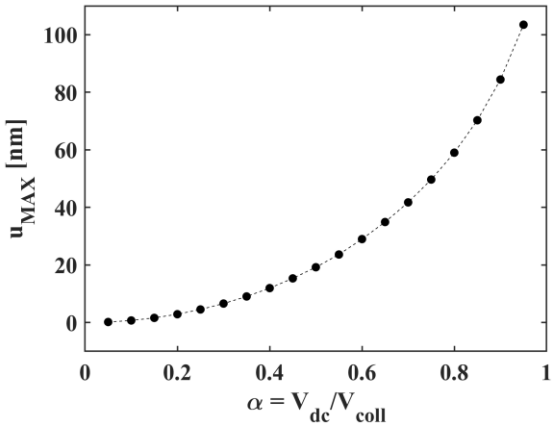

Figure III.10 *The membrane maximum displacement computed by varying the bias voltage $V_{dc} = \alpha V_{coll}$, with α varying from α = 0.05 to α = 0.95.*

III.3.3 Static capacitance computation

In order to design the front-end electronics, it is important to consider the static capacitance value of the biased transducer. Analytical models always compute the static capacitance by modelling the device with a parallel plate capacitor, though using the membrane average displacement value to compute an equivalent gap height. FEM simulations compute the static capacitance as the sum of all the capacitance values of the capacitors into which the active area is divided. Basically, each transducer element TRANS126 acts as a small parallel plate capacitor. Therefore, if the membrane radius is divided in a sufficiently high number of small segments, the different displacement experienced by each TRANS126 element returns a different capacitance value. The capacitance of each element placed along the radius must be summed, as the small capacitors are in parallel. Since the model is axisymmetric, static capacitance value of the single transducer cell can be obtained by integration across the electrode area.

As the bias voltage is increased, the membrane moves closer to the substrate, reducing the cavity height at the static equilibrium. This increases the total capacitance value, as can be observed in Figure III.11.

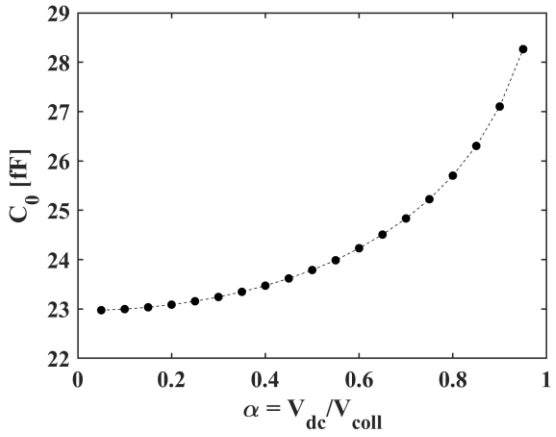

Figure III.11 *The static capacitance value of the RF-CMUT cell described in Table III.1, computed by ANSYS by varying the bias voltage $V_{dc} = \alpha V_{coll}$, with α varying from α = 0.05 to α = 0.95.*

III.3.4 Spring-softening effect

Increasing the bias voltage also causes a phenomenon known by the name of *spring-softening*. As already explained, the increase of the bias voltage causes an increase of the attraction between the membrane and the substrate, due to the higher electrostatic force that pushes one electrode towards the other. From the mechanical point of view, this relates to a lower flexural rigidity of the membrane, and a reduced elastic spring constant k_m of the membrane (hence the name "*spring-softening* effect"). Due to the lower flexural rigidity, also the resonance frequency of the structure decreases as the bias voltage is increased. For this reason, also the sensitivity bandwidth has a centre frequency drifting towards a lower value as the bias is raised. FEA can be used to compute quickly the resonance frequency depending on the bias voltage applied, by means of a modal analysis for the model including the electromechanical coupling.

Figure III.12 shows the first axisymmetric mode resonance frequency computed by varying the bias voltage from 5% to 95% of the collapse voltage. The reduction is greater when the bias voltage approaches the collapse value, due to the increase of the electrostatic force that makes the attraction between the plate and the substrate stronger. The unbiased device had a resonance frequency f_{m0} = 13.13 MHz. By increasing the voltage applied across the electrodes, the resonance frequency reduces until the value f_{m0} = 8.79 MHz when the bias approaches the collapse voltage value.

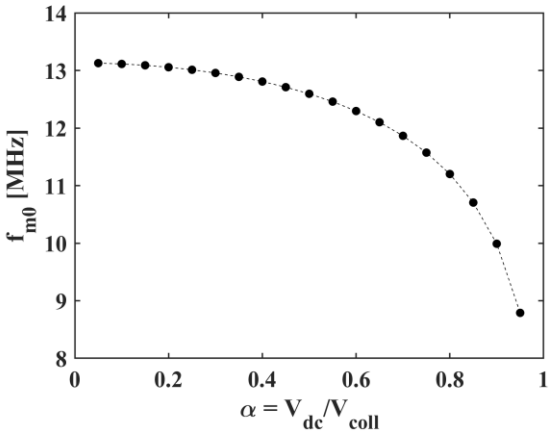

Figure III.12 *The first mode resonance frequency fm0 computed by the modal analysis (ANSYS), performed by varying the bias voltage $V_{dc} = \alpha V_{coll}$, with α varying from α = 0.05 to α = 0.95.*

III.4 Dynamic behaviour analysis

When operating in receive mode, transducers must detect small ultrasonic signals propagating through an attenuating medium; thus, a linearized small-signal analysis is appropriate for the purpose of describing the receiving behaviour of an imaging device. When operating in transmit mode, though, the amplitude of the input signal must be high, in order to generate a strong acoustic output power. In this case, a linearized analysis is not accurate enough, as the system nonlinearities cannot be neglected anymore. For this reason, an accurate finite element analysis of the transmit performance of an acoustic transducer requires a time-domain simulation.

III.4.1 Transient analysis in fluid-coupled condition

The finite element transient analysis can be used to perform a time-domain simulation of CMUTs in transmit, receive or pulse-echo operation. In order to simulate the transmission and reception of waves to and from a propagating medium, the FEM model must include the fluid coupling. The transmission behaviour can be simulated by feeding the transducer with a voltage pulse similar to the one produced by a pulser device. The results can then be post-processed to extract the transmitted pressure wave propagating in the fluid. The behaviour in receive mode can be simulated by applying a pressure signal on the transducer surface, or by generating an acoustic pressure inside the fluid, so that the acoustic wave impinges on the device surface and generates a received voltage signal. The pulse-echo operating mode, which is much more interesting for the study of the performance of imaging devices, can be

simulated by removing the absorbing boundary from the fluid column top surface and by providing an input signal as for the transmit behaviour simulation. In this way, the voltage pulse applied across the electrodes causes the generation of an acoustic wave that impinges on the upper boundary of the fluid column and propagates back towards the transducer surface, due to the total reflection occurring at the boundary because of the acoustic impedance mismatch between the fluid and the vacuum. Thus, by reading the pressure in the fluid and the voltage across the electrodes, the device behaviour can be studied both in transmission and in reception operation. Finally, by performing a Fast Fourier Transform of the generated and received pulses, the Transmission Transfer Function (TTF) and the Reception Transfer Function (RTF) of the transducer can be computed to evaluate the device performance.

The Transmission Transfer Function (TTF) is defined as

$$TTF = \frac{P_t}{V_{in}} \tag{III.11}$$

where P_t is the transmitted pressure and V_{in} is the input voltage, and is also known as the output pressure-per-volt function. It represents the transmission efficiency of the device.

The Reception Transfer Function (RTF) is defined as

$$RTF = \frac{V_r}{P_{in}} \tag{III.12}$$

where V_r is the generated voltage, in response to the pressure P_{in} impinging on the transducer front face. It represents the receive sensitivity of the device.

In the following sections, the results obtained by simulating the CMUT device described in Table III.1 in pulse-echo operation are discussed. The analysis was performed by varying the device dimensions and by increasing the bias voltage applied to the device. The characterization of the pulse-echo behaviour was made by observing the membrane average displacement, the pressure signal propagating in the fluid and the voltage signal across the cell electrodes. These signals were obtained by averaging the results on a circular area by means of a surface integral.

The transient analysis, performed by time steps of t_s = 1 ns, is divided in three loadsteps. During the first step, which lasts for t_{dc} = 100 ns, the bias is applied to reach the static equilibrium. In conventional operation, the membrane is prestressed by the application of a bias voltage slightly lower than the collapse value. During the second step, a broadband voltage pulse is applied across the electrodes: the input signal, generated by a MATLAB script in form of a text file, is a -16 V unipolar raised cosine voltage pulse. The excitation signal lasts 50 ns, but the voltage constraint is maintained for a time t_{exc} = 900 ns to allow the membrane displacement transients to extinct. The generated pressure signal propagates through the fluid load. Finally, during

the third step the electrical constraint is removed, and the system is observed for $t_{obs} = 2.5$ μs, until the final time $t_{end} = t_{dc}+t_{exc}+t_{obs} = 3.5$ μs. During this interval, the pressure signal reaches the top boundary of the fluid waveguide, where total reflection occurs: the pressure signal returns towards the transducer unaltered, due to the ideal boundary of the model and the absence of acoustic losses in the loading. For this reason, if the pressure is observed at a fixed height in the fluid, two identical pulses can be seen in sequence: the first is the signal propagating along the positive *y*-direction, the second is the signal reflected from the boundary and propagating along the negative *y*-direction. Since the fluid waveguide has a sound speed $c_{flu} = 1500$ m/s and a length $l_{flu} = 1$ mm, and the pressure is observed at a distance $l_{flu}/2 = 500$ μm from the device front face, the first pressure pulse is seen at a time t_{p1} given by

$$t_{p1} = t_{dc} + \frac{l_{flu}}{2c_{flu}} = 433 \text{ ns} \tag{III.13}$$

and the second pulse is seen at a time

$$t_{p2} = t_{dc} + \frac{3l_{flu}}{2c_{flu}} = 1.1 \text{ μs} \ . \tag{III.14}$$

As the pressure wave impinges on the transducer surface, the membrane is set into vibration and another pulse appears in the average displacement. This occurs after the pressure signal has travelled along twice the full length of the fluid, hence at a time

$$t_{d2} = t_{dc} + \frac{2l_{flu}}{c_{flu}} = 1.43 \text{ μs} . \tag{III.15}$$

At the same time, due to the membrane displacement, a received voltage signal is generated. This is the first echo signal, which is the signal used for the reconstruction of the investigated structure in ultrasound imaging.

Due to the transducer surface reflectivity, the pressure is newly reflected into the fluid. This reflected pressure is observed at the distance $l_{flu}/2$ at

$$t_{p3} = t_{d2} + \frac{l_{flu}}{2c_{flu}} = 1.77 \text{ μs} . \tag{III.16}$$

This pressure pulse once again undergoes total reflection at the top boundary, travels along the negative *y*-direction and reaches the transducer surface at a time

$$t_{d3} = t_{d2} + \frac{2l_{flu}}{c_{flu}} = 2.76 \text{ μs} \tag{III.17}$$

generating a second voltage echo at the same time. This second echo is the first reverberated echo, which causes unwanted artefacts on the ultrasound image. The elimination of the reverberation phenomenon is an important issue in the improvement of the quality of the ultrasound images. Some methods for the reduction of the transducer surface acoustic reflectivity involve the tuning of the backing layer acoustic impedance [92], of the receiving electronics electrical impedance [93] or a combination of both [84], [94]. Otherwise, the possibility to remove the reverberation artefacts after the image reconstruction by means of image post-processing have also been investigated [95].

The voltage across the electrodes, the membrane average displacement and the pressure signal at a distance l_{flu} /2 from the CMUT front face, computed from $t_0 = 0$ to $t_{end} = 3.5$ μs, are shown in Figure III.13. The simulated device is the RF-CMUT with the nominal values of the geometrical parameters listed in Table III.1 and the material parameters reported in Table III.2.

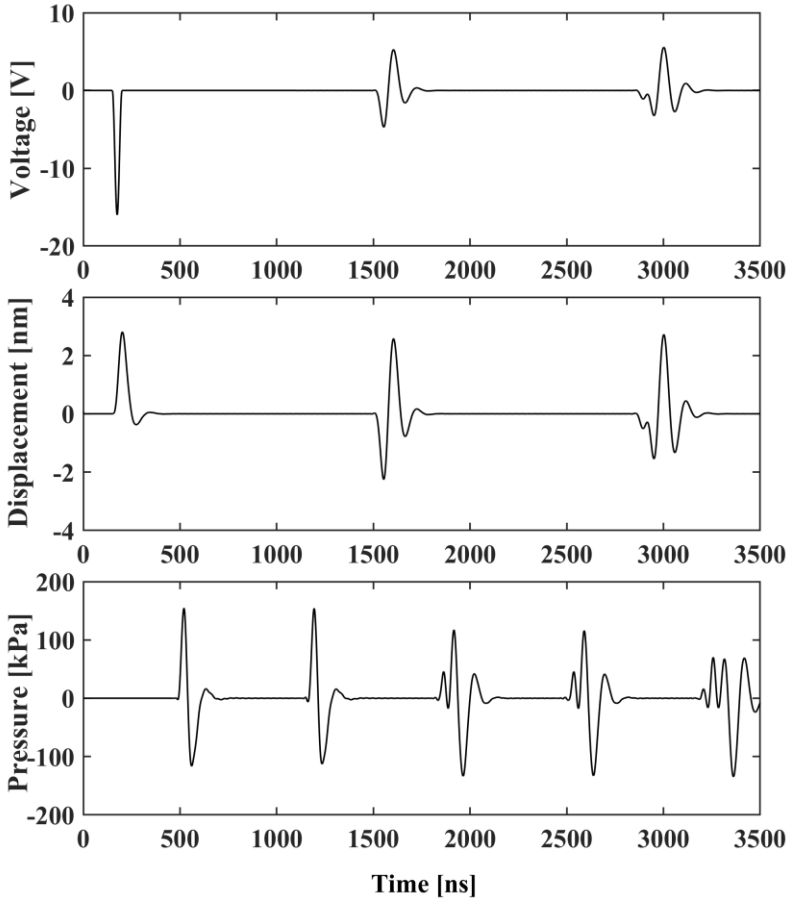

Figure III.13 *The voltage across the electrodes, the membrane average displacement and the pressure propagating in the fluid in the time domain, computed by a transient analysis (ANSYS).*

Following, a study of the displacement, pressure and voltage signal in the frequency domain is proposed. The time-domain simulation of the pulse-echo operation, followed by a Fast Fourier Transform operation on the resulting signals, is performed by varying the geometry of the RF-CMUT cell, the bias voltage and the backing acoustic impedance of the device with the nominal geometrical parameters.

III.4.2 CMUT dynamics relation to structural parameters variation

As already explained in Section III.2, the design of the CMUT device starts with the membrane geometrical parameters definition according to the desired resonance frequency. The same resonance frequency can be achieved by infinite couples of radius and thickness values, and the dimensions of the membranes that populate the array determine the dynamic performance of the transducer; therefore, an efficient design must consider how the variation of radius and thickness affects the transducer dynamics. Simulating the pulse-echo behaviour in the time domain by varying the membrane parameters provides an important background for an efficient design of the CMUT device.

The membrane average displacement, the pressure propagating in the fluid and the voltage signal in simulated pulse-echo operation were computed by varying the membrane radius r_m, the membrane thickness t_m and the cavity height d. The CMUT devices were biased at $V_{dc} = 0.98\ V_{coll}$, with V_{coll} collapse voltage value computed in Section III.3.1 for the investigated structures. In the following analysis, the curves resulting from the simulation of the CMUT with the nominal dimensions listed in Table III.1 are always represented by a continuous line.

The membrane displacement, caused by the input voltage pulse, is a broadband pulse with a transient component superimposed to the average static displacement value. Hence, in the frequency domain, the displacement is a lowpass signal. The maximum amplitude of the displacement is observed close to the biased transducer mechanical resonance frequency. As already discussed in Section III.2.3, the resonance frequency decreases by increasing the membrane radius r_m and by decreasing the membrane thickness t_m. Consequently, the displacement maximum amplitude frequency exhibits the same behaviour, as can be observed in Figures III.14 and III.15. The gap height d variation, instead, affects the static displacement but has a negligible effect on the displacement frequency content, as shown in Figure III.16. In the figures, the constant average static displacement value is removed from the displacement curves in the time domain, and the displacement frequency spectrum is corrected for the input pulse spectrum.

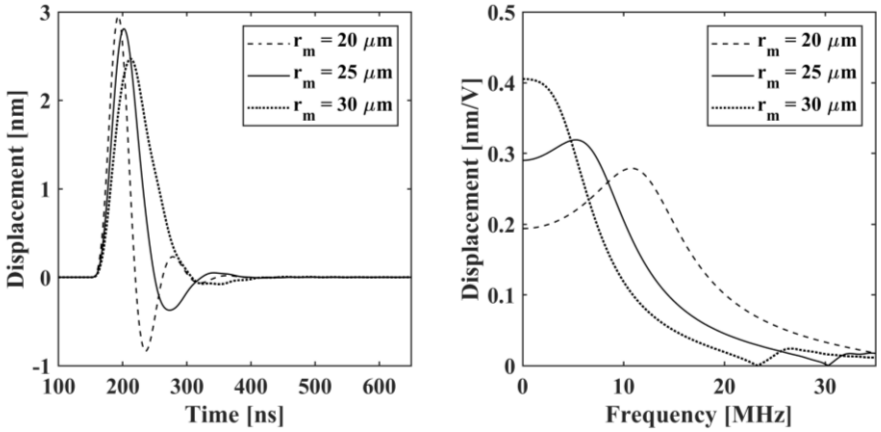

Figure III.14 *The membrane average displacement in the time domain (left) and in the frequency domain (right), in response to a broadband raised cosine voltage pulse, computed by varying the membrane radius.*

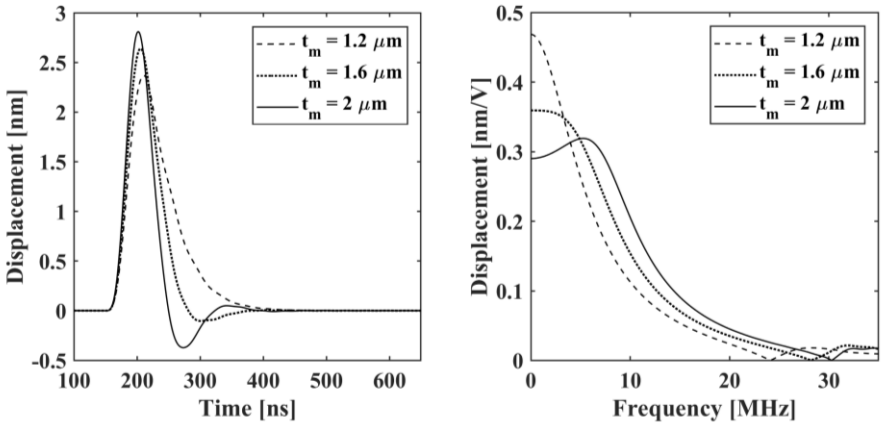

Figure III.15 *The membrane average displacement in the time domain (left) and in the frequency domain (right), in response to a broadband raised cosine voltage pulse, computed by varying the membrane thickness.*

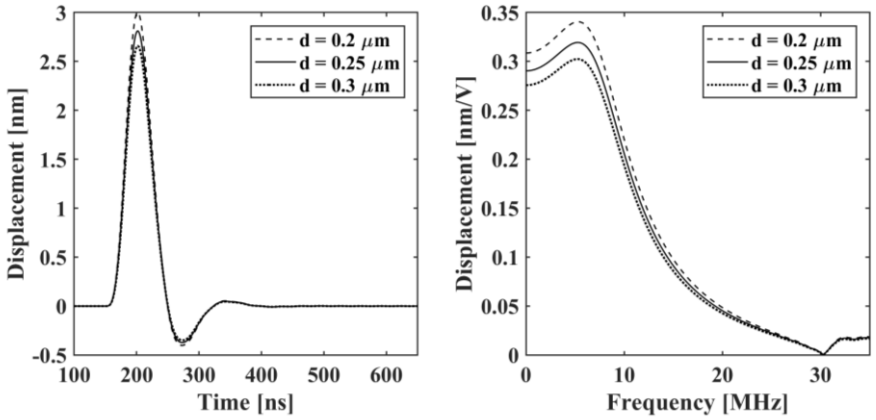

Figure III.16 *The membrane average displacement in the time domain (left) and in the frequency domain (right), in response to a broadband raised cosine voltage pulse, computed by varying the cavity height.*

As the frequency increases, a second resonant mode is excited, determining a notch in the frequency spectrum of the average displacement between the first and the second mode frequency. This null average displacement corresponds to a null transmitted pressure, therefore the same notch can be found in the frequency spectrum of the average pressure, corrected for the input voltage pulse. The transmitted pressure, shown in the time domain on the left and in the frequency domain on the right of Figures III.17, III.18 and III.19, was computed at a distance $l_{flu}/2$ from the transducer radiating surface by varying the membrane radius r_m, membrane thickness t_m and cavity height d, respectively. Figure III.17 shows that, as the membrane aperture increases, if the input signal amplitude is kept constant, the pressure amplitude decreases. The maximum amplitude frequency also decreases due to the lower flexural stiffness of the membrane, which lowers the mechanical resonance frequency. For the same reason, the opposite effect can be noticed by increasing the membrane thickness, as shown in Figure III.18.

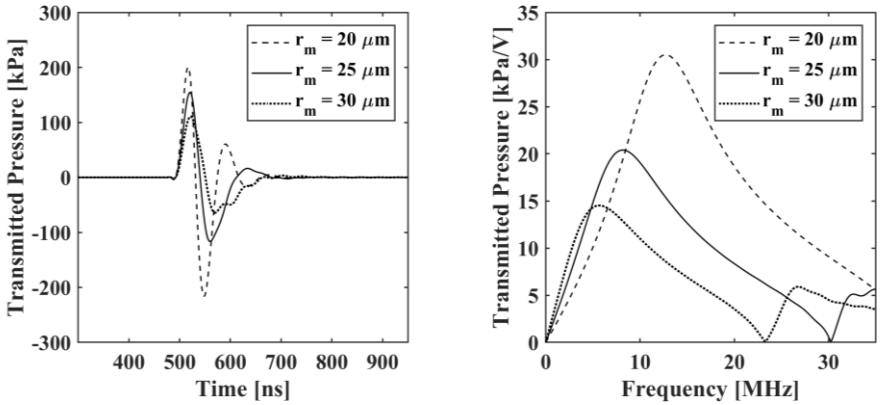

Figure III.17 *The transmitted pressure in the time domain (left) and in the frequency domain (right) computed by varying the membrane radius.*

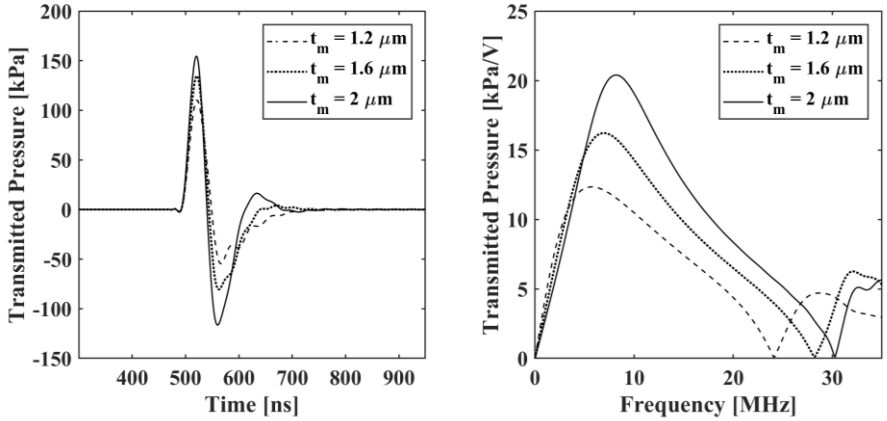

Figure III.18 *The transmitted pressure in the time domain (left) and in the frequency domain (right) computed by varying the membrane thickness.*

Varying the membrane radius or thickness strongly affects the transmission performance of the device. The bandwidth variation of the transmission transfer function due to the variation of the membrane radius and thickness can be easily evaluated by observing the normalized functions shown in Figure III.19 and Figure III.20. In particular, increasing the membrane aperture and thickness always determines an increase of the transmitted pressure but a reduction of the TTF bandwidth. These results are in agreement with those found in the literature[91]. The membrane geometry must then be designed according to the target application, by taking into account these effects.

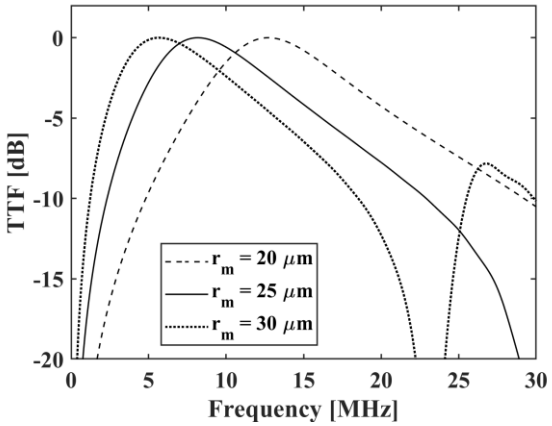

Figure III.19 *Normalized Transmission Transfer Function (TTF) computed by varying the membrane radius.*

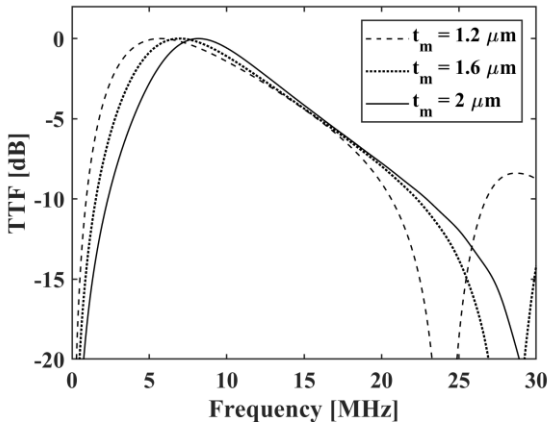

Figure III.20 *Normalized Transmission Transfer Function (TTF) computed by varying the membrane thickness.*

Unlike the membrane aperture or thickness variation, the cavity height variation does not affect the transmitted pressure harmonic content. As can be noticed in Figure III.21, the frequency spectrum of the transmitted pressure computed by varying the gap height has unvaried harmonic content. The peak amplitude, instead, increases by reducing the distance between the membrane and the substrate. For this reason, it can be concluded that a small gap height improves the output pressure per volt of a given design, at the expense of inevitable technological and electrical issues, the first arising from the difficulties of removing thin layers of sacrificial material by microfabrication techniques, and the latter arising from the increased risk of dielectric breakdown. These results are in agreement with those found in the literature [83].

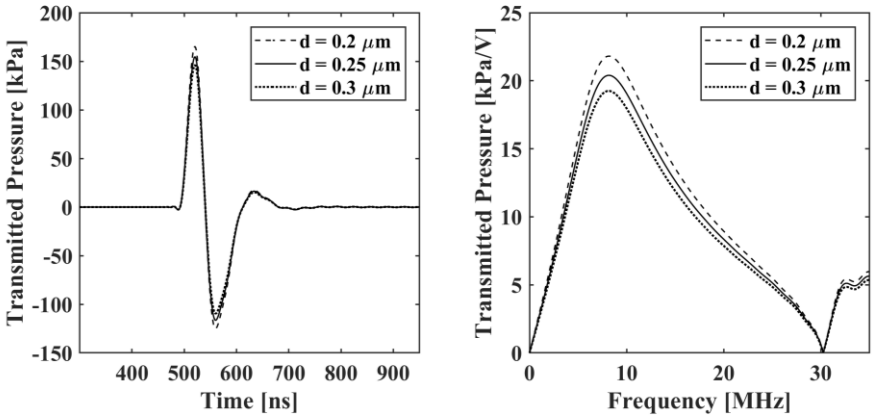

Figure III.21 *The transmitted pressure in the time domain (left) and in the frequency domain (right) computed by varying the cavity height.*

After the pressure wave is reflected by the top boundary of the fluid column, it newly reaches the transducer surface, generating a voltage signal. This simulates the echo received from a highly reflective structure during ultrasound imaging conventional pulse-echo operation.

Again, the resonance frequency shift due to the flexural stiffness dependence on the membrane radius is clearly observed by looking at the received voltage signals both in the time domain and in the frequency domain in Figure III.22. As the membrane radius increases, a lower number of periods can be seen in the same time interval; therefore, the signal has a higher-frequency resonant peak. Moreover, the higher is the flexural stiffness, the higher is the signal amplitude. These effects are also observed by increasing the membrane thickness, as shown in Figure III.23.

For what concerns the cavity height variation, only the amplitude of the received signal is affected, as shown in Figure III.24.

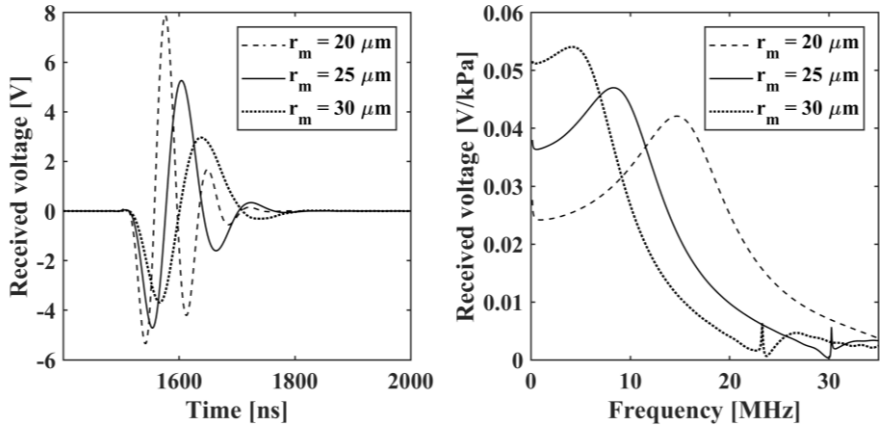

Figure III.22 *The voltage echo in the time domain (left) and in the frequency domain (right) computed by varying the membrane radius.*

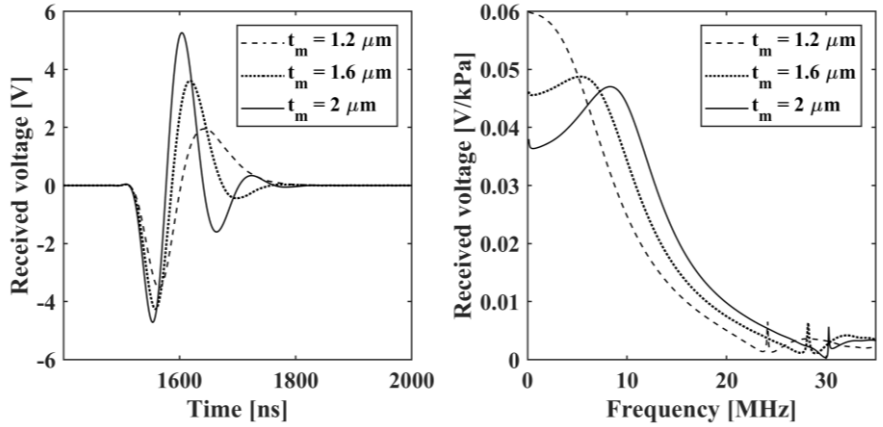

Figure III.23 *The voltage echo in the time domain (left) and in the frequency domain (right) computed by varying the membrane thickness.*

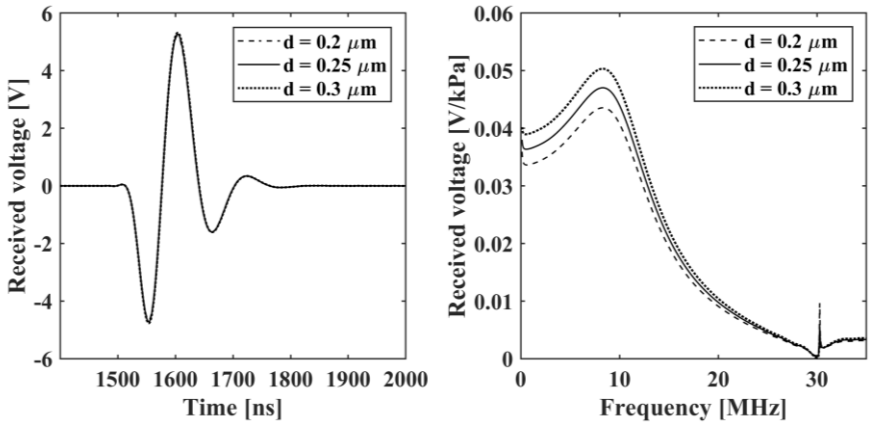

Figure III.24 *The voltage echo in the time domain (left) and in the frequency domain (right) computed by varying the cavity height.*

III.4.3 Bias voltage influence on the CMUT array dynamic behaviour

The bias voltage value does not only affect the static behaviour of the CMUT device, but also the dynamic performance. As previously described in Section III.3.4, the increase of the bias voltage causes the *spring-softening* effect. From the static point of view, the decrease of the first mode resonance frequency was observed by means of a modal analysis, performed by increasing the applied bias voltage. From a dynamic point of view, the spring-softening effect can be clearly observed by looking at the resonant peak of the displacement and of the transmitted pressure in the frequency domain (see Figures III.25 and III.26). The transient analysis was performed by increasing the bias voltage $V_{dc} = \alpha\, V_{coll}$, with α varying from α = 0.5 to α = 0.9, provided to the CMUT device described in Table III.1. It can also be noticed that a higher bias voltage produces a stronger transmitted pressure (in Figure III.26) and a higher received voltage signal (in Figure III.27). In fact, the electromechanical conversion coefficient increases proportionally with the applied static voltage [31], [78]. The bias voltage affects the transmission behaviour more than the receive performance, as can be clearly evinced from Figure III.28 and Figure III.29, which show the TTF and the RTF of the device, respectively, as defined by eqs. (III.11) and (III.12). It is worth noting that, in both cases, increasing the bias voltage increased the amplitude of both the TTF and the RTF: the bias voltage is the only parameter whose variation improves both transmission and reception efficiency.

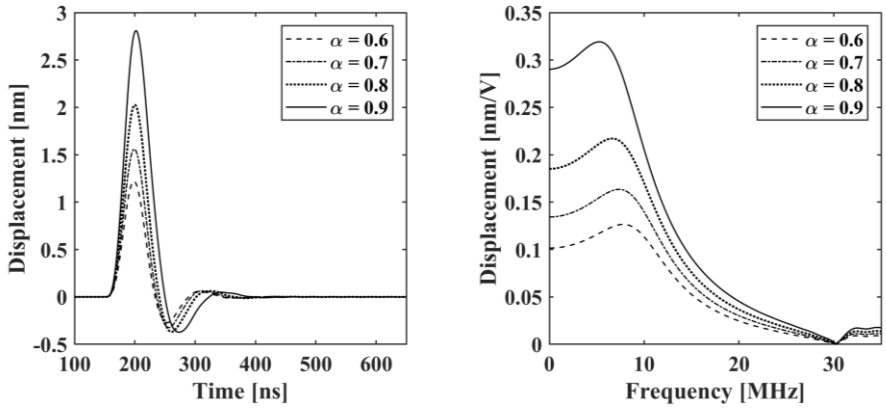

Figure III.25 *The membrane average displacement in the time domain (left) and in the frequency domain (right), computed by varying the bias voltage.*

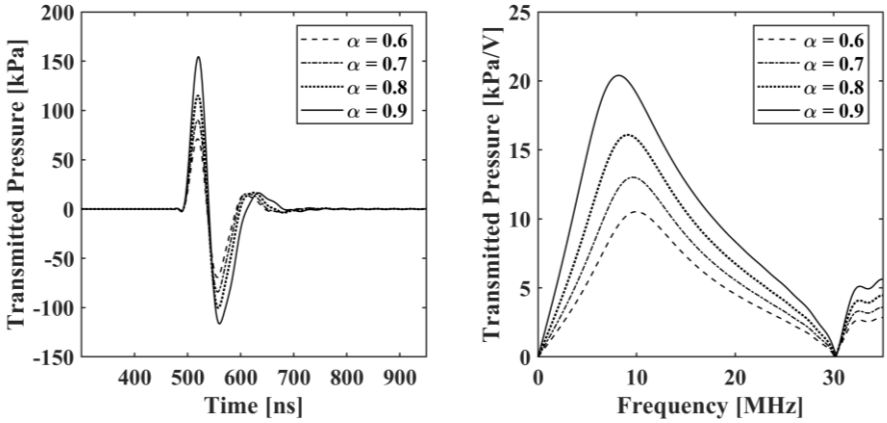

Figure III.26 *The transmitted pressure in the time domain (left) and in the frequency domain (right) computed by varying the bias voltage.*

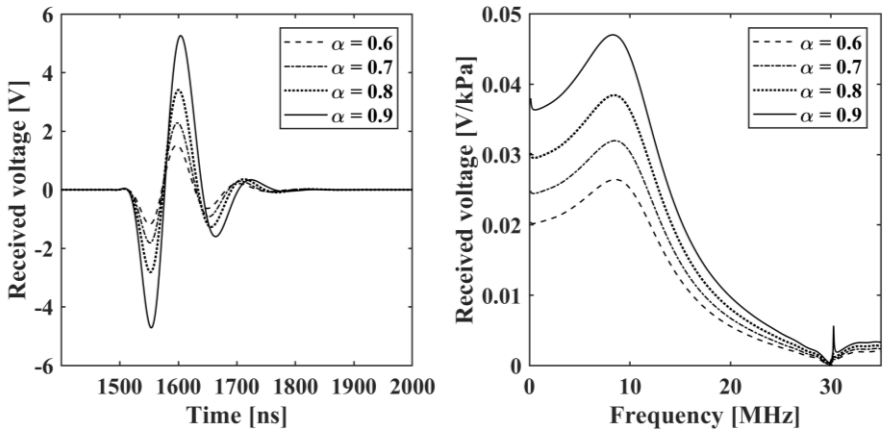

Figure III.27 *The voltage echo in the time domain (left) and in the frequency domain (right) computed by varying the bias voltage.*

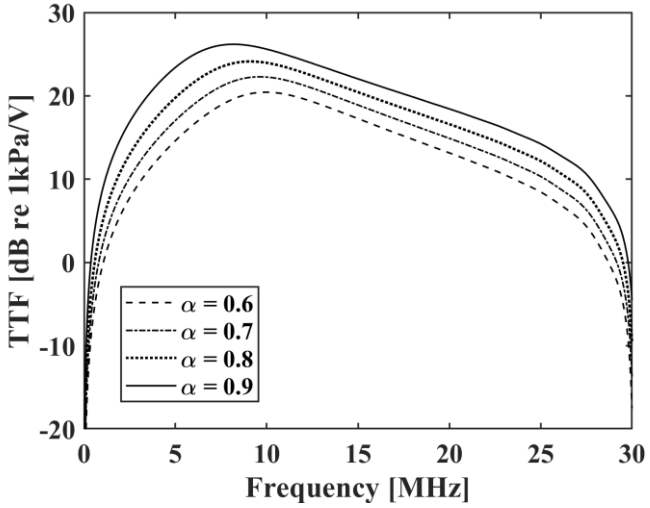

Figure III.28 *The TTF computed by varying the bias voltage in pulse-echo behaviour simulation.*

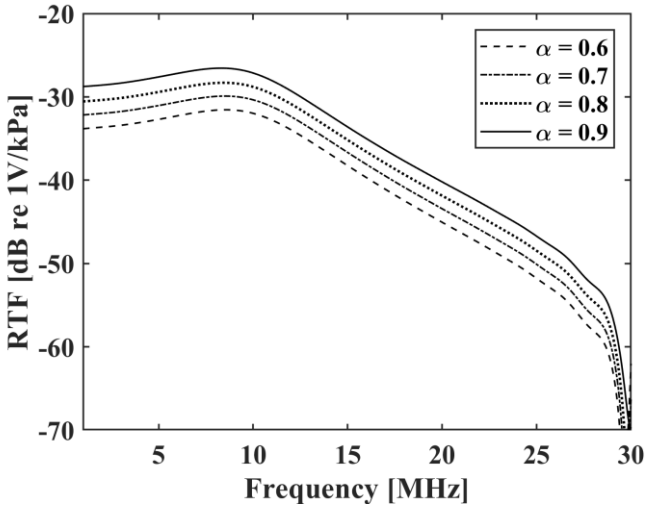

Figure III.29 *The RTF computed by varying the bias voltage in pulse-echo behaviour simulation.*

III.4.4 Backing effect on the CMUT array performance

In order to reduce the ringing of the pulse-echo signal, ultrasonic transducers are usually provided with acoustic backings. Backing layers should either be made of lossy materials or have irregular bottom surfaces, since their purpose is to improve the dissipation of the acoustic energy propagating towards the back surface of the transducer, in order to prevent its backscattering. To be efficient, backing materials should have an acoustic impedance that matches that of the device substrate [96]–[99].

With respect to traditional CMUT devices, RF-CMUTs are much thinner. Fabrication by the reverse process, in fact, implies that the structural Silicon Nitride is grown on top of the membrane; hence, there is no Silicon substrate under the transducer. So, devices fabricated by the reverse process are only a few microns thick [54]. Since the ultrasound imaging operating frequencies range from 2 to 15 MHz, wavelength in immersion are typically in the 100-750 μm range. Therefore, the RF-CMUT thickness is much smaller than the acoustic signal wavelength. For this reason, the backing layer acoustic impedance should not match that of the device structural material, but the acoustic impedance of the load, which is much close to the impedance of water. Low-impedance materials, such as rubbers and epoxy resins, are usually very lossy, due to their irregular polymeric matrix. This allows reverse fabricated devices to be provided with very efficient backing layers.

The presence of a soft material under the transducer bottom surface leads to a different acoustic behaviour of the device, as compared to the case of a rigid substrate. This latter case is usually modelled by the boundary condition

of clamped substrate, obtained by setting to zero the nodal displacements of the bottom surface. The previous analysis of the static and dynamic behaviour of a RF-CMUT element was performed under this condition.

Subsequently, the effects of three different acoustic backings on the performance of a wide aperture RF-CMUT device are described. The considered backing materials are compounds based on the Epo-Tek 301-2 epoxy resin (Epoxy Technology Inc., Billerica, MA), obtained by filling the resin with Alumina powder and Tungsten powder in order to increase the acoustic impedance of the resulting material. The materials were realized and characterized at Roma Tre University. The measured acoustic properties of the backing compounds are listed in Table III.3. Simulations were performed by biasing the transducer at $V_{dc} = 0.9\ V_{coll}$, where V_{coll} was newly computed, following the procedure described in Section III.3.1, by including the backing layer in the model.

Table III.3 *Measured material properties of the backing compounds.*

Backing compound	Acoustic impedance z_B [MRayl]	Density ρ [kg/m^3]	Speed of sound c [m/s]
Epoxy resin Epo-Tek 301-2	2.75	1251	2666
Epoxy + Al	5.19	1724	2868
Epoxy + Al + W	8.23	3485	2096

Figures III.30 and III.31 show that the amplitude of the displacement and transmitted pressure curves decreases by providing backings made of materials with lower acoustic impedance. This is due to the transmission of energy to the backing, which improves by improving the match of the acoustic impedance of the backing material to the impedance of the fluid load. In the clamped substrate case, the nodal displacements at the bottom surface are set to zero, as if the device was sitting on top of an infinitely rigid substrate. In this case, no energy was transferred below the device, and most of the energy was directed towards the load. When a backing is added at the bottom of the device, instead, the constraint on the displacement DOFs at the bottom surface of the device is removed, and the base of the device acts as another plate coupled to a low impedance solid material (the backing); therefore, it is free to move. The electrostatic force both bends the membrane towards the bottom electrode and raises the back plate towards the top electrode. This partitioning of the electrostatic force between the front plate and the back plate reduces the average displacement computed on the top surface of the device and shown in Figure III.30. The acoustic wave generated in response to the input voltage pulse also has a lower amplitude, as it is directed both towards the fluid and towards the backing. The transmission to the backing is higher when the backing material acoustic impedance is better matched to the fluid acoustic impedance (i.e. when it is lower), as can be seen in Figure III.31.

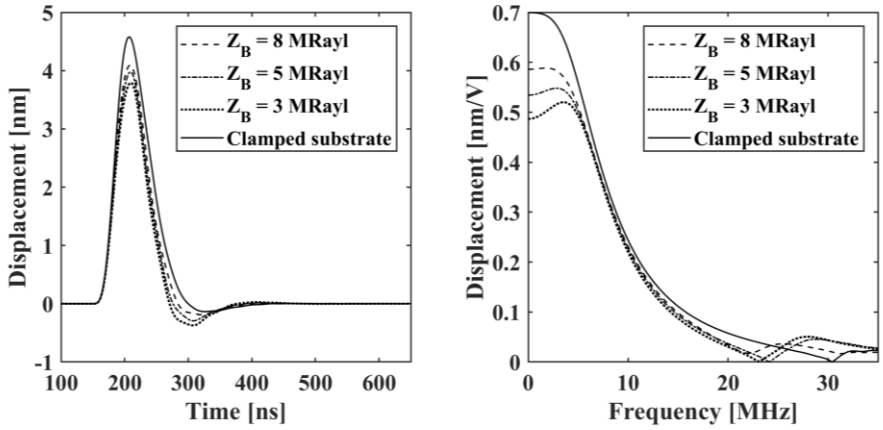

Figure III.30 *The membrane average displacement in the time domain (left) and in the frequency domain (right), computed by varying the backing acoustic impedance.*

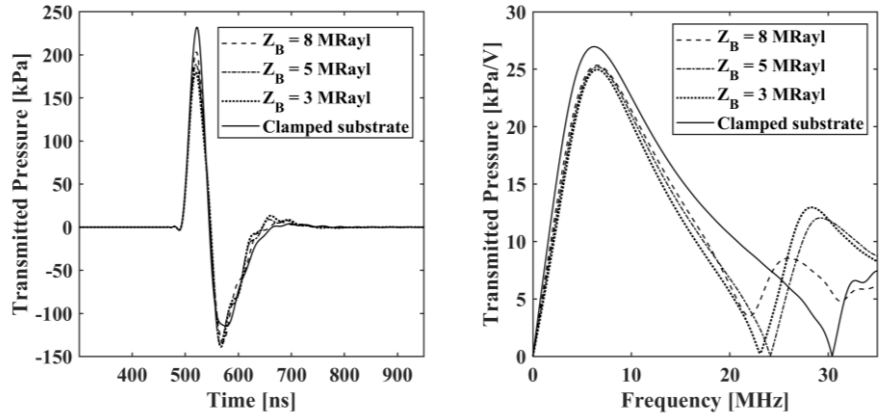

Figure III.31 *The transmitted pressure in the time domain (left) and in the frequency domain (right) computed by varying the backing acoustic impedance.*

Figure III.32 shows the transmission transfer function computed by varying the backing material, and it can be clearly evinced that the backing impedance value also affects the frequency of the dip in the transmission transfer function, caused by the excitation of the higher modes that determine a null average displacement. This change in the frequency response is due to the change in the mechanical impedance of the device. The mechanical impedance of the structure varies due to the mass and stiffness variation caused by the addition of the backing layer. In particular, by reducing the backing acoustic impedance a sharper resonant peak is clearly noticeable in the reception transfer function shown in Figure III.33.

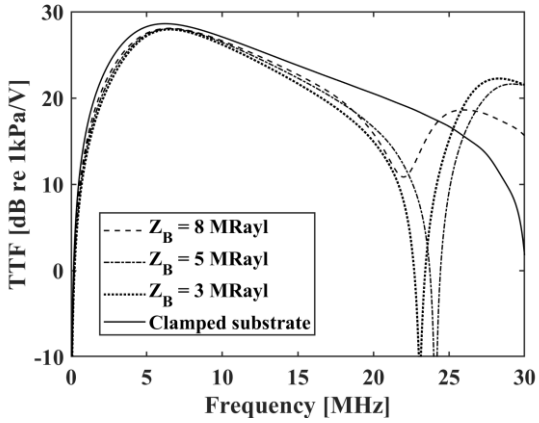

Figure III.32 *Transmission Transfer Function (TTF) computed by varying the backing acoustic impedance.*

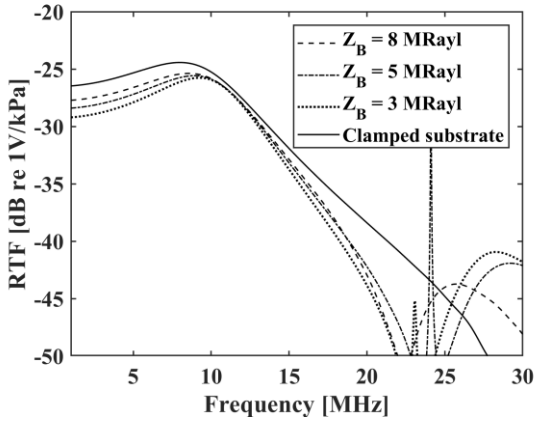

Figure III.33 *Reception Transfer Function (RTF) computed by varying the backing acoustic impedance.*

As a consequence of the lower amplitude of the average displacement and transmitted pressure signals observed by reducing the backing material acoustic impedance, also the received voltage amplitude decreases by lowering the acoustic impedance of the backing layer. The first received voltage echo has unvaried harmonic content, regardless of the backing material properties (see Figure III.34). Nevertheless, the backing acoustic impedance strongly affects the second received voltage echo, both in terms of magnitude and frequency spectrum. This second echo, shown in Figure III.35, is due to the pressure reflected by the transducer front face, newly sent towards the transducer after the total reflection occurring at the fluid top boundary, and simulates the first reverberation signal. We remind that this second echo is strongly unwanted in ultrasound imaging, since it causes detrimental artefacts on the ultrasound image.

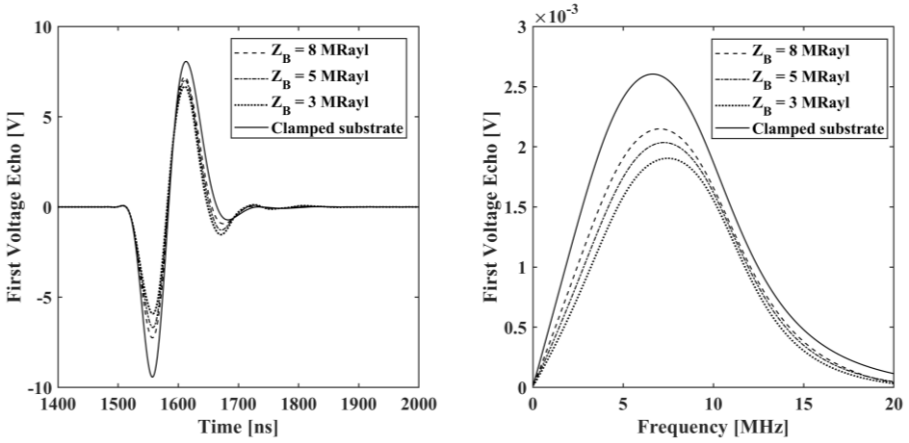

Figure III.34 *The voltage signal generated by the first echo received from the load, in the time domain (left) and in the frequency domain (right), computed by varying the backing acoustic impedance.*

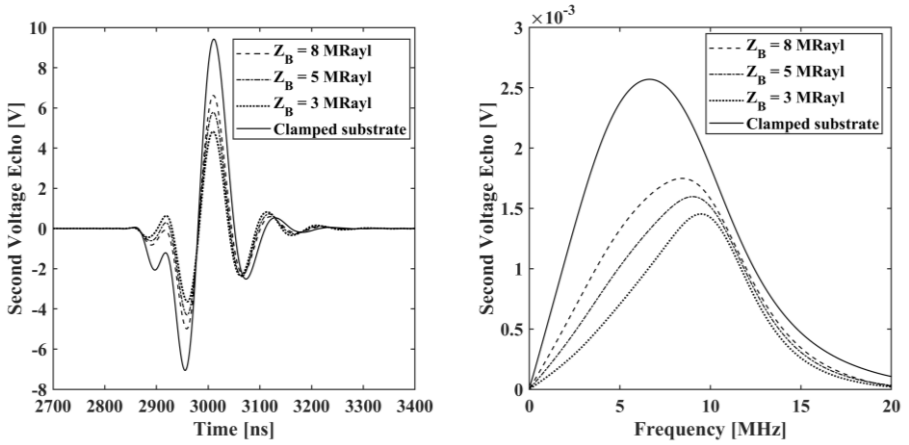

Figure III.35 *The voltage signal generated by the second echo received from the load (first reverberation signal), in the time domain (left) and in the frequency domain (right), computed by varying the backing acoustic impedance.*

Again, the reduction of the second echo amplitude must be ascribed to the better acoustic matching obtained by using a backing material whose acoustic impedance is closer to the propagating medium acoustic impedance. The acoustic wave of the first echo signal, incoming from the medium and propagating towards the transducer surface, is partly reflected towards the load due to the surface acoustic reflectivity and partly transmitted to the backing, by means of the area between the membranes where the fluid and the backing are separated only by the Silicon Nitride. As the coupling between

these materials becomes more efficient, i.e. as the backing material acoustic impedance gets closer to the impedance of the fluid, the transmission of mechanical energy from the fluid to the backing is improved, and less energy is reflected towards the medium. In this way, the second echo signal impinging on the transducer surface is attenuated. This situation reduces the front face acoustic reflectivity, and results in a reduction of the intensity of the reverberation phenomenon, as thoroughly discussed in [84], [94]. This effect of the backing acoustic impedance variation on the reduction of the reverberation phenomena can be observed in Figure III.36, which shows the reverberation level (RL) computed by varying the backing material acoustic impedance compared to the reverberation level computed in the clamped substrate case. The reverberation level was computed as the ratio between the spectrum of the voltage signal generated by the second received echo V_2 (the first reverberated signal) and the spectrum of the voltage signal generated by the first received echo V_1 (the signal used for the image formation in ultrasound imaging):

$$RL = \left| \frac{V_2}{V_1} \right| . \tag{III.18}$$

As can be seen, by clamping the nodal displacements of the bottom surface no attenuation of the reverberation level is observed until the frequency approaches the transmitted pressure notch frequency. The application of an acoustic backing, on the contrary, reduces the ratio between the second and the first received echo signal. Matching the acoustic impedance of the backing with the acoustic impedance of the fluid load further improves the reverberation reduction within the transducer sensitivity bandwidth, thus leading to an improvement of the quality of the obtained ultrasound image.

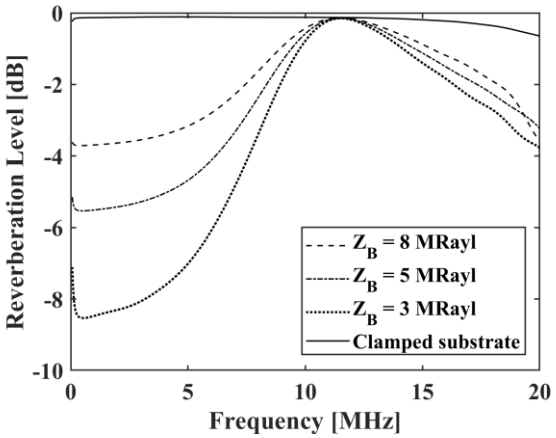

Figure III.36 *The reverberation level (RL), computed as the ratio between the second and the first received voltage echoes, computed by varying the backing acoustic impedance.*

Chapter IV
Performance analysis of a RF-CMUT sparse array

IV.1 Pressure radiation from an acoustic transducer array

According to Huygens' diffraction theory, the pressure field generated by any source can be computed by assuming the radiating aperture is made of an infinity of point sources. The amplitude of the pressure field radiated by the aperture is determined by the constructive and destructive interference between the pressure waves radiated by the point sources into which the aperture is divided. Thus, integrating the pressure emitted by a simple source over the transducer aperture leads to the computation of the pressure radiated by an arbitrary source in any point of the half-space facing the transducer. In this process, the non-uniform velocity potential across the source aperture must be taken into account.

Let us consider an arbitrary source lying on the *xy* plane, as shown in Figure IV.1. The distance between the considered point $P(r,\theta,\phi)$ and the centre of the aperture is *r*, and the distance between $P(r,\theta,\phi)$ and each simple source composing the aperture is *r*'. The angle that forms between the distance *r* and the axial direction *z* is θ, and the angle between *r*' and *z* is θ'.

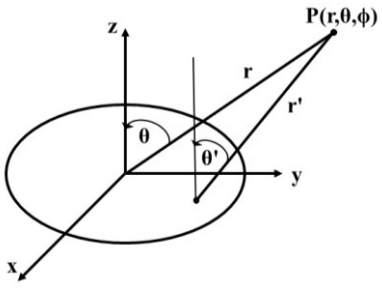

Figure IV.1 *Geometry of an arbitrary source observed from a generic point* $P(r,\theta,\phi)$

Then, the velocity potential as a function of the position r in the frequency domain $\Phi(r,\omega)$ is expressed by the Rayleigh-Sommerfeld integral [1]:

$$\Phi(r,\omega) = -\frac{1}{2\pi}\int_S \frac{e^{j[\omega t - k\cdot r']}}{r'}\frac{\partial v(r')}{\partial n}dS \tag{IV.1}$$

where $\partial v(r')/\partial n$ is the normal component of the velocity distribution as a function of the position on the radiating surface, k is the wavenumber $k = 2\pi/\lambda$ and S is the radiating surface composed of infinite small elements dS. Let us assume that the normal velocity $v_n(r')$ is uniform across the aperture and equal to v_0, so that

$$v_n(r') = \frac{\partial v(r')}{\partial n} = v_0 A(r') \tag{IV.2}$$

where $A(r')$ is the *aperture function* of the transducer.

In this case, the radiated pressure $P(r,\omega)$ can be obtained by deriving the velocity potential and multiplying by the propagating fluid density ρ, and by using eqs. (IV.1) and (IV.2) it can be computed as

$$P(r,\omega) = -j\omega\rho\,\Phi(r,\omega) = j\frac{\omega\rho v_0}{2\pi}\int_S \frac{e^{j[\omega t - k\cdot r']}}{r'}A(r')dS\,. \tag{IV.3}$$

The resulting transmitted pressure depends on both the distance from the radiating source and the angle with respect to the normal axis under which the pressure is observed. In the far field zone, that conventionally starts at an on-axis distance depending on the widest aperture lateral dimension a by $z = a^2/\lambda$, the distance r' can be approximated by r; similarly, the angle θ' can be replaced by θ.

Then, for simple geometries, the pressure field far from the aperture can be expressed by separating the dependence on the distance r and the angle θ, as in

$$P(r,\theta) = P_{ax}(r)H(\theta) \tag{IV.4}$$

where $P_{ax}(r)$ is the axial pressure, which is the pressure computed along the axis normal to the radiating surface of the transducer, and $H(\theta)$ is the directivity factor. The directivity represents the way the acoustic intensity spreads along the angular direction from the transducer to the front space. The directivity is maximum and equal to unity along the axial direction $\theta = 0$. For complex apertures, it can also depend on the spherical coordinate ϕ.

As is well known [87], [100], in the far field the directivity function on a plane at a fixed distance from the transducer is the Fourier transform of the aperture function. This makes the directivity function quite easy to compute for simple geometries of the aperture, such as rectangular or circular apertures. In these particular cases, the directivity can be expressed in form of *sinc*

functions and *jinc* functions, respectively. The positions of the nulls of *sinc* and *jinc* functions determine the angles θ where the interference of the pressure waves is completely destructive. These directions describe a nodal surface on the radiation pattern, where there is no transmitted pressure. Between the nodal surfaces, corresponding to the relative maxima of the directivity function, the radiation lobes can be observed, as can be observed in the example in Figure IV.2.

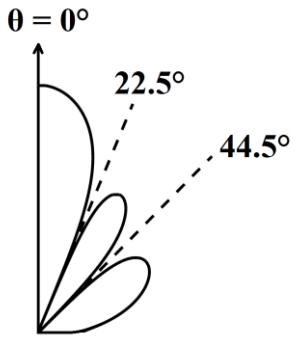

Figure IV.2 *The directivity of a circular aperture a vibrating with a uniform normal velocity, radiating pressure with ka = 10. The radiated pressure field is null for θ = 22.5° and θ = 44.5°.*

The spatial pattern of the acoustic radiation at a fixed frequency on the azimuthal plane is usually plot in the decibel scale, and referred to as the *beam pattern* of the transducer:

$$BP(\theta) = 20\log_{10}\left(\left|H(\theta)\right|\right). \tag{IV.5}$$

The main lobe of the radiation pattern is centred in θ = 0 (the axial direction) and spreads until the first nodal surface. For a single radiating aperture, the number of nulls and lobes in the radiation pattern depends only on the aperture dimension with respect to the wavelength at the considered frequency.

For an array of sources, all the previous study can be repeated by considering the diffraction phenomena as due to the interference of the pressure waves radiated by each of the elements of the array. In particular, due to the spatial sampling of elements in the array, the total radiation pattern will be made by replica of the spatial Fourier transform of the array aperture, whose periodicity depends on the spatial periodicity of the array elements. For instance, if we consider an array of elements arranged in space with a periodicity *p*, the radiation pattern will have several *grating lobes* directed along directions given by

$$\theta_g = \arcsin\left(m\frac{\lambda}{p}\right). \tag{IV.6}$$

This infinite repetition of the array aperture function transform will be modulated by the spatial Fourier transform of the aperture function of the single array element, centred in $\theta = 0$. Due to the small dimensions of the element with respect to the array, the element aperture function corresponds to a broad directivity, also referred to as *element factor*, which can include more than one grating lobe of the narrow array directivity inside its main lobe.

As the input signals of the elements are delayed in order to steer electronically the beam by an angle θ_s, the grating lobes also shift at angles

$$\theta_g = \arcsin\left(m\frac{\lambda}{p} + u_s\right) \tag{IV.7}$$

where

$$u_s = \sin\theta_s \tag{IV.8}$$

depends on the steering angle θ_s.

The element factor, on the contrary, remains centred at $\theta = 0$. For this reason, the steered beam is attenuated due to the gain loss of the element factor, resulting in a loss of sensitivity as the steering angle increases.

This is better explained in Figure IV.3 [1], which shows the steps for obtaining the radiation pattern of a wide linear array of small rectangular elements in the space of the variable $u = \lambda/p$. Due to the array finite aperture, the total radiation pattern includes an infinite repetition of *sinc* functions, centred in multiples of λ/p, as shown in Figure IV.3 (a). The *sinc* functions are the spatial Fourier transform of the array aperture function, and are characterized by a narrow main lobe due to the array wide size. In Figure IV.3 (b) the grating lobes are modulated by the broad main lobe of the *sinc* function of the element factor, spatial Fourier transform of the rectangular array element, whose directivity is wider due to the small dimensions. Finally, Figure IV.3 (c) shows the steered beam centred in u_s, within the element directivity main lobe.

Therefore, it is the width of the array element directivity to determine the capability to steer the transmitted beam without losing drastically pressure intensity. For this reason, during the design of a transducer array, the shaping of the element factor is of uttermost importance to improve the array steering capability.

In conclusion, in order to realize a high-performing transducer array it is important to have a very broad directivity of the element factor. Moreover, the element factor directivity should not include grating lobes: they represent a transverse sensitivity for the array that is highly detrimental for the resulting image quality. As the grating lobes are spaced according to the inverse of the

spatial period *p*, their existence within the element factor is prevented by reducing the distance between the radiating sources of the element below λ/2. This is the reason why acoustic arrays where the steering capability is an important feature are always made by closely packed elements.

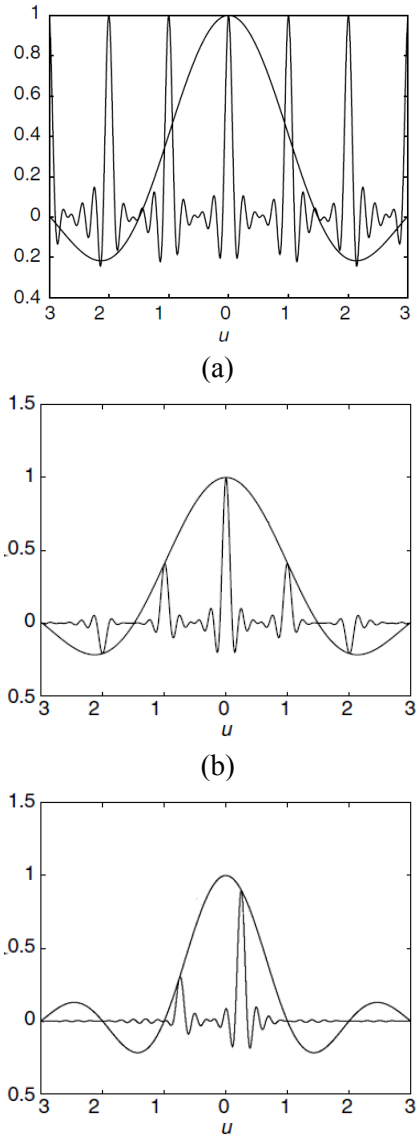

Figure IV.3 *The radiation pattern of a linear array of rectangular elements: (a) the repetition of the array factor according to the elements spacing, (b) the element factor modulating the grating lobes, (c) the steered beam within the main lobe of the element directivity.*

IV.2 FEA of the Fermat's spiral-based RF-CMUT sparse array

In Section II.1, the importance of the realization of a FEM model for the design optimization of CMUT sparse arrays was introduced. Due to the complexity of the electroacoustic behaviour of such a structure, finite element analysis is the only tool able to provide reliable prediction of the performance of a sparse array. Since 2D arrays are aimed at performing a volumetric scan, which requires the electronic beam steering, it is of great interest the study of the beam steering capabilities by observing the array directivity. A wide main lobe and low-level side lobes are desired characteristics for the device element factor.

In the view of the improvement of the performance of the RF-CMUT sparse array based on the Fermat's spiral presented in [66] and described in Section I.3, the FEM model proposed in Section II.5 was used to investigate the acoustic behaviour in transmission operation of the device.

The FEM model was used to analyse the beam pattern of the sparse array by means of a harmonic analysis at the operating frequency f_{op} = 7 MHz, by taking into account the underlying BCB layer. The effect on the acoustic performance of carving trenches into the BCB layer that makes the bonding with the front-end chip was investigated.

IV.2.1 Static analysis

The harmonic analysis simulating the transmission performance of the Fermat's spiral based RF-CMUT sparse array required the membranes to be prestressed by the application of a bias voltage, lower than the collapse voltage value, during a static analysis. In order to perform the static analysis, the collapse voltage of the cells composing the sparse array element was computed by repeating a static analysis with increasing values of the bias voltage. The material properties used in the simulation are in Table IV.1.

Table IV.1 *Material parameters used in the sparse array element simulation.*

	Young's modulus [GPa]	Poisson ratio	Density [kg/m^3]	Relative permittivity	Longitudinal velocity [m/s]
LPCVD SiN	180	0.25	3000		
PECVD SiN	88	0.25	2600	7	
Aluminium	70	0.33	2700		
BCB	2.9	0.34	957		
Fluid (water)			1000		1500

The resulting collapse voltage of the spiral array CMUT cells was V_{coll} = 173 V in the case of clamped substrate, and V_{coll} = 157 V in presence of the BCB layer under the transducer array.

Figure IV.4 shows the membrane displacement along the *z*-axis obtained by applying a bias voltage V_{dc} = 157 V to the 30° section of the sparse array element. The results, computed by means of a nonlinear static analysis, were expanded to show the entire array element.

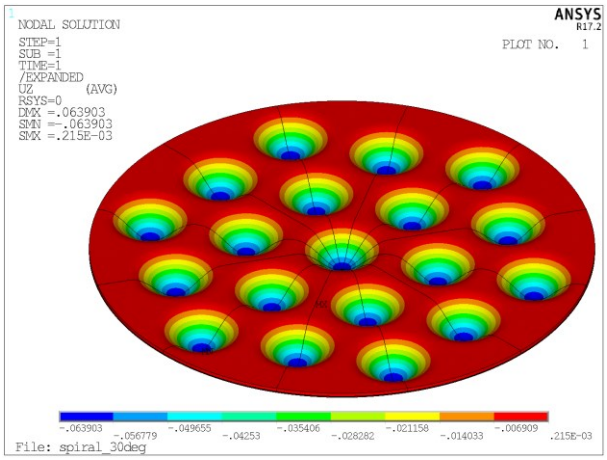

Figure IV.4 *Contour plot of the z-component of the displacement, obtained by a static analysis (ANSYS) performed by biasing the sparse array element with V_{dc} = 157 V.*

Figure IV.5 shows that the BCB layer, used to bond the CMUT array with the analog front end, suffers a deformation when the membranes deflect because of the applied bias voltage. Since this layer is mechanically active, its presence affects the collapse voltage.

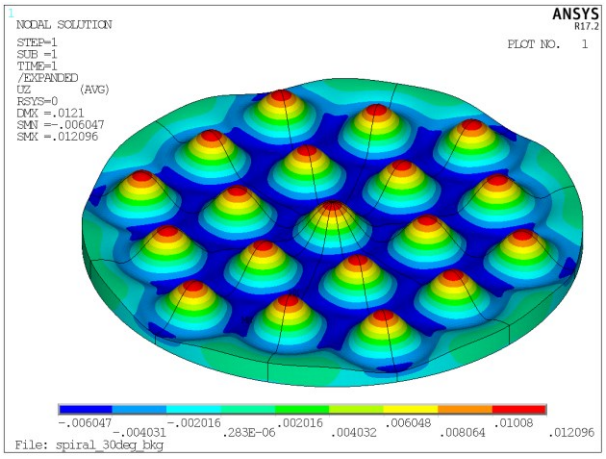

Figure IV.5 *Contour plot of the z-component of the displacement, obtained by a static analysis (ANSYS) performed by biasing the sparse array element provided with the BCB backing layer with $V_{dc} = 0.9\ V_{coll}$.*

IV.2.2 Element factor analysis

The ANSYS harmonic analysis tool was used to simulate the transducer array behaviour in transmission operation. The simulation was run at the operating frequency f_{op} = 7 MHz. The membrane displacement along the *z*-direction, normal to the radiating surface of the transducer, and the pressure wave propagation into the fluid hemisphere were observed.

The transmitted pressure in the θ-plane shown in Figure IV.6 clearly shows that, in addition to the main lobe, the first side lobes also figure in the half space into which the transducer irradiates; one surface of null directivity can be observed. Due to the symmetry of the structure, the transmitted pressure does not depend on the ϕ coordinate, thus Figure IV.6 fully describes the radiation performance of the array element at the investigated frequency.

By taking advantage of the ANSYS tool that reconstructs a time domain animation of the model DOFs starting from the harmonic results, it is possible to observe the pressure wave traveling from the radiating surface of the transducer through the fluid hemisphere. This operation is also useful to verify that the absorbing boundary at the outer surface of the fluid sphere is actually working. Figure IV.7 shows, from (a) to (d), the propagation of the pressure wave in harmonic regime in the time domain.

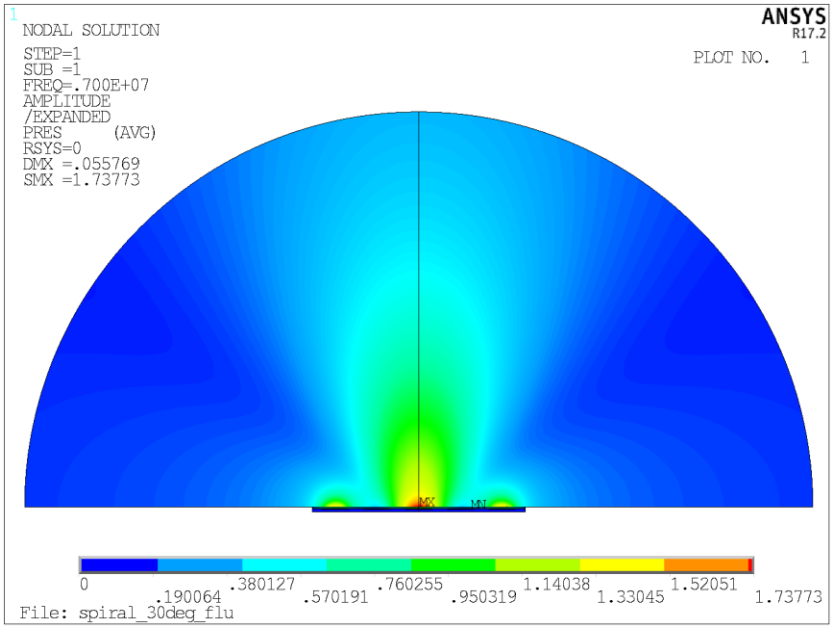

Figure IV.6 *Average transmitted pressure computed by harmonic analysis (ANSYS) at f = 7 MHz.*

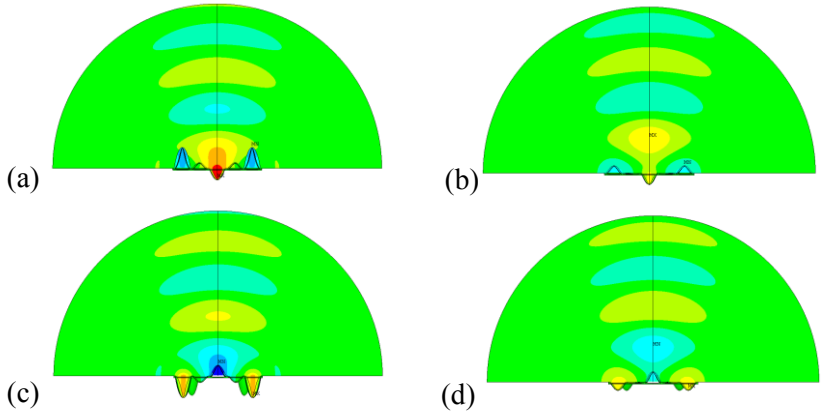

Figure IV.7 *Different frames showing the pressure wave traveling from the transducer surface through the acoustic medium at f = 7 MHz.*

One observation that immediately arises from looking at Figure IV.7 is that, even if the membranes are excited by the same input signal, they are not moving in phase. Only the membranes positioned at the same distance from the centre of the element vibrate in phase with one another. This behaviour is a consequence of the diffraction phenomenon, and can be analytically described also by referring to the self and mutual radiation impedance of flexural plates [101]. The dynamics of the displacement of flexural membranes immersed in an acoustic medium were thoroughly analysed by means of the computation of the mutual radiation impedance in [102]. Figure IV.8 gives a better understanding of this phenomenon by showing different frames of the time-domain animation of the normal displacement at $f = 7$ MHz.

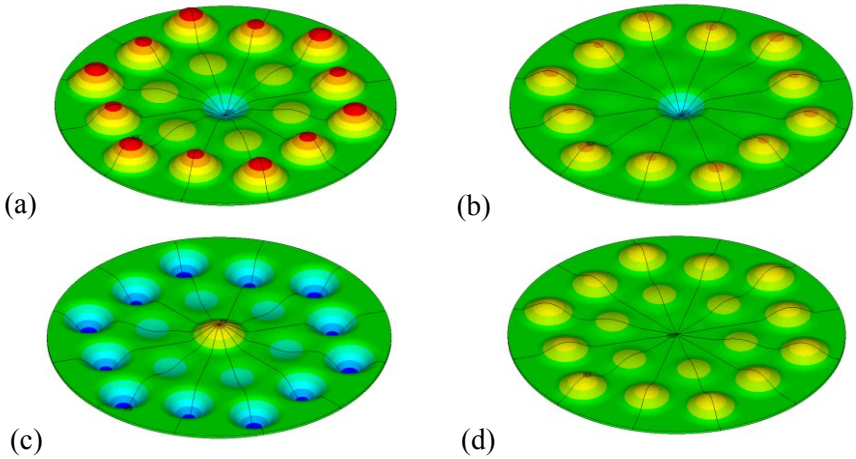

Figure IV.8 *Different frames showing the displacement along the z-axis (the pressure wave propagation direction) at f = 7 MHz.*

The beam pattern of the array element (element factor) was also computed by reading the pressure amplitude on a hemispherical surface of the acoustic medium in the far field region. Figure IV.9 shows the beam pattern obtained from the pressure computed at a distance $R = 500$ μm from the radiating surface of the transducer and represented on the θ-plane. The element directivity has a nodal surface at $\theta_n = 57°$, and the -6 dB half beam width of the main lobe (i.e. the angular section where the transmitted acoustic power is at least half the maximum power transmitted along the axial direction) is 32.5°.

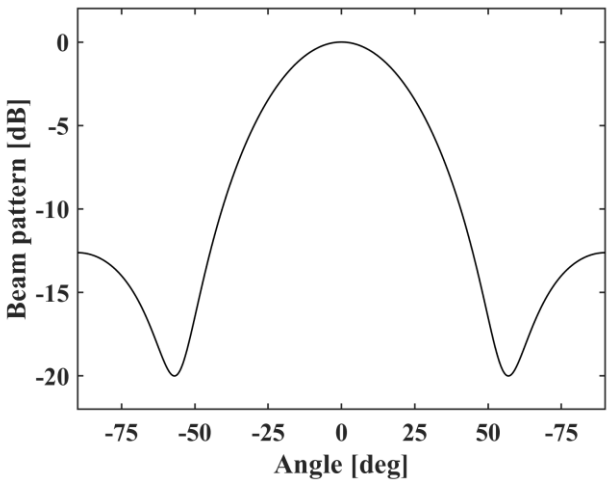

Figure IV.9 *Acoustic radiation pattern obtained from the pressure computed at a distance R = 500 μm from the radiating surface of the transducer.*

IV.3 Substrate effect on the sparse array performance

The packaging technology of the multi-module chip described in [64] supplies the CMUT array with a bonding layer that allows the interconnection of the transducer array with the analog front-end. The height of this Benzocyclobutene (BCB) layer was optimized by performing FEM simulations of the frequency response of the CMUT device. In order to evaluate the effect of this BCB layer on the element directivity, the 12-μm thick BCB backing was included in the FEM model of the sparse array, and the beam pattern was computed by applying different sets of boundary conditions. In particular, the nodes of the outer side surface of the array element and of the backing layer were constrained, preventing the displacement along the radial direction. The backing can only move along its thickness. In this way, the behavior of the array element included in a bigger device made of a continuous layer of both Nitride and BCB was simulated. Later, the possibility to etch trenches in the backing layer in order to isolate

acoustically the BCB underlying each array element was considered. By releasing the constraint on the nodes of the outer side surface of the backing layer, radial displacements were allowed. Finally, the constraint was eliminated also on the outer nodes of the CMUT structural Nitride: in this way, the array element was completely isolated from the rest of the array, as if the trenches were etched in both the BCB and the CMUT.

Figure IV.10 compares the beam pattern computed in the clamped substrate case with the directivity obtained in the different boundary conditions sets applied to the device with the backing layer. It can be seen that, with respect to the clamped substrate case, the addition of an infinitely extended backing layer in the lateral direction reduces the -6 dB half beam width from 32.5° to about 28°. At the same time, this condition improves the side lobe level, which drops from -12.6 dB to -18.3 dB. Applying trenches in the backing layer does not affect the result on the beam width with respect to this latter case, but gives slightly worse results for the side lobe level, that sets to -16.2 dB. Finally, the isolated element directivity shows a -6 dB half beam width of 30° with a side lobe level of -12.6 dB, as for the clamped substrate case.

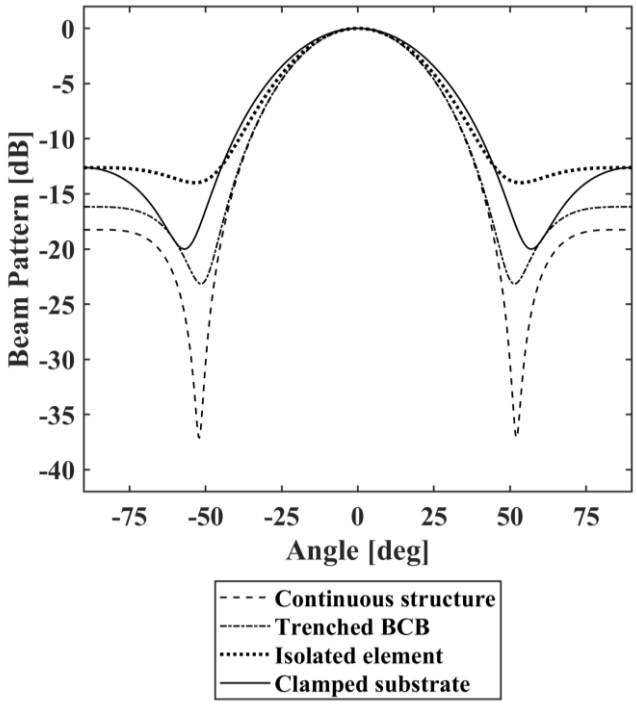

Figure IV.10 *Comparison between the array element beam pattern in the case of clamped substrate with the beam pattern of the backed device. For this latter case, three different boundary conditions are applied to the outer edge of the element.*

IV.4 Comparison with measurements

The MCM was recently tested and characterized. Acoustic measurements were performed by connecting the assembled probe head to the ULA-OP 256 scanner [103] and acquiring the radiated pressure fields by a HGL-0400 hydrophone (Onda Corporation, Sunnyvale, CA). The array elements were driven by 3-cycle Hanning tapered sine bursts, at the operation frequency of f_{op} = 7 MHz. The acquisition was carried out on a 20x20 mm area at the focal depth of 20 mm in different steering conditions: 0° (unsteered), 17° and 27°. Due to the hydrophone limited angular acceptance, the main lobe level (ML) was underestimated in the steered conditions, and a rough compensation was applied. The side lobe level (SLL) was also observed.

The measurements were compared to the simulated beam pattern computed by applying the boundary condition that represent the array element inserted into a laterally extended structure (hence, without any trench in the Nitride or in the BCB layer).

The measured one-way beam pattern returned a SLL of -28.7 dB, with respect to a simulated result of -18.3 dB. The attenuation of the ML due to the beam steering resulted, after the compensation, in ML = -4.3 dB for θ = 17° and ML = -10 dB for θ = 27°. The simulated directivity, which can be observed in Figure IV.11, shows an attenuation of the maximum amplitude of -2.1 dB for θ = 17° and -5.5 dB for θ = 27°. The small difference between the simulated values and the measured values is probably due to the inaccuracy of the hydrophone directivity compensation. In conclusion, the model proved efficient in simulating the RF-CMUT sparse array element.

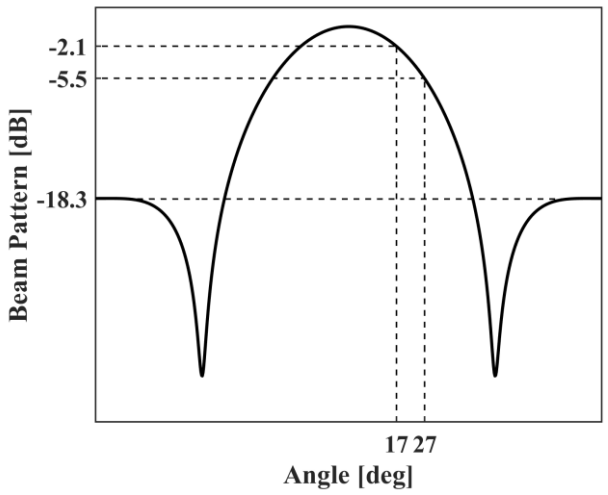

Figure IV.11 *The simulated beam pattern (ANSYS) computed by assuming the array element included in a continuous structure, to reproduce the boundary conditions of the measured device.*

Chapter V
Flextensional piezoelectric transducers

V.1 Transducers for NDT and acoustic emission techniques

Non-destructive testing (NDT) can be performed by means of ultrasound techniques, based on piezoelectric transducers operated in a pulsed mode. Analysis of reflection, scattering and attenuation of elastic waves inside a solid medium can provide information about its internal structure, in particular about the presence of discontinuities such as fractures or obstacles on the propagation path. Testing techniques include pulse-echo and through-transmission operation [104]. In pulse-echo operation, one piezoelectric transducer works as both transmitter and receiver, generating an acoustic wave inside a medium and receiving its reflection, thus relating the measured time-of-flight (the delay between the transmitted and reflected wave) to the distance between the transducer and the obstacle inside the investigated structure. In through-transmission operation, two transducers are used with the different role of transmitter and receiver, each having its own independent driving circuit. In both cases, a high conversion efficiency is required in order to collect pulses with a good signal-to-noise ratio. Moreover, the time duration of pulses should be short (broadband signals), in order to have a good spatial resolution along the axial direction. Short pulses can be obtained by increasing the operation frequency, though higher frequency signals undergo a stronger attenuation, or by increasing the transducer bandwidth, which also means increasing internal losses. Unfortunately, both measures lower the signal-to-noise ratio. Nevertheless, the use of low-noise amplifiers in the read-out circuit can improve the output signal amplitude, thus making a wide bandwidth the most desirable feature in ultrasonic transducers for non-destructive tests. The sensitivity centre frequency is usually tuned accordingly to the application requirements.

Acoustic emission techniques require the use of transducers as receivers of transient signals generated inside a medium. Frequencies of interest are

typically unknown, but usually limited to the 20 kHz – 400 kHz range; therefore, the reception transfer function of the transducer should have a flat, wide bandwidth in the low frequency ultrasonic range. For this reason, the optimization process of transducer for acoustic emission applications aims at improving the reception sensitivity bandwidth characteristics, such as the width and ripple.

Thickness-mode piezoelectric transducers are usually provided with one or more matching layers, interposed between the radiating surface and the load medium. They reduce the acoustic impedance mismatch between the transducer and the medium in order to widen the transfer function bandwidth. Such layers work as “mechanical transformers”, increasing the mechanical load at the interface and therefore adapting the load to the transducer impedance. Flexural transducers do not require matching layers, since their mechanical impedance is intrinsically lower, due to the high elasticity of membranes. In fact, membranes oppose very low resistance to vibration, and therefore are a good choice for broadband transducers design.

In recent times, another type of flextensional piezoelectric devices was investigated, which combine the MEMS fabrication technology used for CMUTs fabrication with the piezoelectric properties of new materials. These devices are known as Piezoelectric Micromachined Ultrasonic Transducers (PMUTs), and are very promising for several applications, since they provide the design flexibility of CMUTs without the need for a high bias voltage [105]. The structure of PMUTs is similar to the structure of CMUTs devices, with in addition a thin layer of piezoelectric material attached to the membrane. The bending of the membrane is caused by the deformation of the piezoelectric material in response to an electric input, as for common flexural piezoelectric devices. Since their fabrication relies on micromachining techniques, they can reach frequencies unachievable with bulk piezoceramic-based devices. The piezoelectric layer, in fact, is deposited by a sol-gel process, thus avoiding all the limitations due to the piezoceramic fabrication. Though firstly introduced and analysed at about the same time of CMUTs [106]–[109], only recently they have started being intensively investigated [110], [111]. Even if successful ultrasound imaging performed by means of PMUT arrays was described [112], at the moment their primary application is fingerprint sensing [113]. Nevertheless, several applications for NDT, sensing and imaging are next to come.

V.2 Finite Element model of circular flexural transducers

Flexural transducers have been utilized since the 1960s [114], and are still recognized as efficient and robust transducers [115]. Their vibrational behaviour is still an interesting topic, currently under investigation [116], in order to improve the dynamic performance of this kind of devices. The finite element method is the most reliable method for the simulation of the vibration

dynamics, hence it has been widely used since the early days of the computer technology diffusion [117].

V.2.1 3D FEM model of a flexural transducer

Recently, a 3D FEM model of a metallic plate attached to a thin piezoelectric layer was developed in ANSYS® for the optimization of a flexural sensor for the measurement of liquids density [118]–[120]. The model includes the piezoelectric layer (modelled by SOLID226/SOLID227 20-node/10-node hexahedral/tetrahedral elements, with displacement and voltage DOFs), and the thin metal plate (modelled by SOLID186/SOLID187 20-node/10-node hexahedral/tetrahedral elements, with displacement DOFs), constrained at the edge by setting the displacements DOFs to zero. The piezoelectric material constants are modified, starting from the PZT5-H material constants taken from the literature, in order to fit the electrical impedance measurement. The acoustic medium is modelled by solid elements (SOLID186/SOLID187) or fluid elements (FLUID30/FLUID221 8-node/10-node hexahedral/tetrahedral elements), regardless of the liquid or solid nature of the real medium: solid elements are used to have the displacements as DOFs for the propagating medium constraints, whereas fluid elements are used to ignore shear waves propagation and take into account the longitudinal waves propagation only. If the propagating medium length is such that it can be considered infinite, an absorbing boundary can be included at the farthest edge in order to prevent the reflection of acoustic waves, by using SURF154 surface elements on solid structures and by applying materials with nonzero acoustic impedance on fluid volumes.

Figure V.1 shows the structural model of a circular piezoelectric unimorph meshed with (a) hexahedral and (b) tetrahedral elements. The models have the same accuracy.

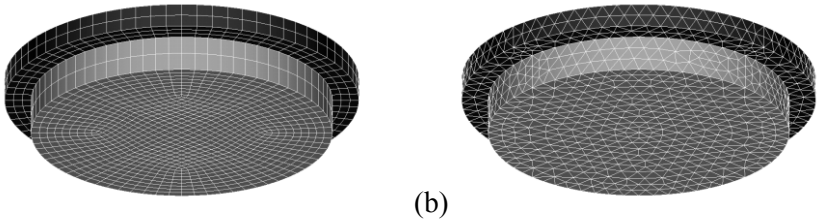

(a) (b)

Figure V.1 *3D FEM structural model of a circular piezoelectric unimorph, meshed with (a) hexahedral elements and (b) tetrahedral elements.*

V.2.2 2D FEM model of a flexural transducer

The simulation of circular plates can take advantage of the axial symmetry to reduce the complexity of the FEM model. In this way, a 2D model can be

used to simulate a 3D object with axial symmetry. Symmetry boundary conditions at the outer edge of the metallic membrane allow the simulation of a wide aperture array composed by several circular membranes by using a very light model.

Figure V.2 shows (a) the 2D axisymmetric structural model of a simple flexural transducer made of an elastic plate and an active piezoelectric layer with clamped edges and (b) its 3D axisymmetric expansion.

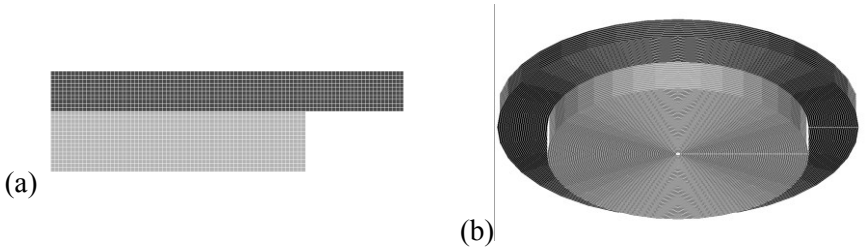

Figure V.2 *a) 2D axisymmetric structural model of a circular piezoelectric unimorph and (b) the model 3D expansion.*

V.3 Design of a broadband flextensional transducer for acoustic emission techniques on concrete structures

Concrete structures undergo a deterioration due to the formation of micro-cracks that can impair the structure stability [121]. Therefore, the monitoring of buildings is of great importance for safety concerns, as it can allow a continuous assessment of their solidity and allow prompt intervention in case of damage. The acoustic waves originated by the formation of cracks inside a concrete structure can be used to collect information about the robustness of the structure itself. The acoustic emission analysis allows the classification of acoustic signals associated to the formation of micro-cracks or the propagation of macro-cracks according to their frequency and intensity. Transducers for acoustic emission techniques applied to concrete structures should have a flat, large bandwidth of the receive sensitivity from 20 kHz up to 180 kHz, according to measurements reported in the literature [122], [123].

Due to the previously described advantages provided by flexural transducers, a piezoelectrically actuated transducer array, optimized for this particular application, was designed.

The concrete-coupled performance of the device was investigated by running harmonic analyses on a finite element model of the considered structure.

V.3.1 The device structure

While thickness-mode piezoelectric transducers can be designed with any aperture size (the bandwidth centre frequency depends on the crystal thickness), flexural-mode transducers require very small membrane lateral dimensions in order to resonate at ultrasonic frequencies. Hence, to increase sensitivity, the active area must be necessarily increased by closely packing small membranes in a dense array. Furthermore, since the device should be adequately coupled to the surface of the medium under investigation, one plain front surface is needed.

Due to the aforementioned reasons, the reference structure for the designed sensor is the multicell flextensional transducer array structure proposed in [124], [125]. The device consists of an array of circular cells arranged by hexagonal tiling. A plate made of an elastic material is coupled to several circular piezoelectric ceramics; each piezoelectric disk is housed inside a cavity, defined by an epoxy layer patterned with circular holes and glued to the back of the front plate. The cavity is closed by a metallic substrate. Figure V.3 shows (a) the exploded view of such array made of 19 cells and (b) the fully assembled view of a single transducer cell.

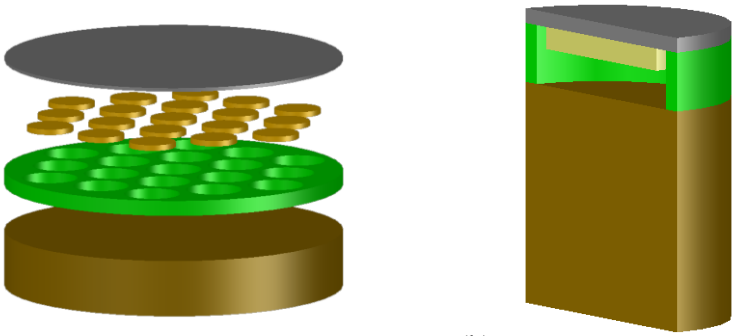

(a) (b)

Figure V.3 *The structure of the proposed device in (a) an exploded view of the array and (b) an assembled single cell section.*

The sensitivity of flexural transducers is maximum close to the membrane first axisymmetric mode frequency, which linearly depends on the membrane thickness and is inversely proportional to the square of the membrane radius, as already discussed in Chapter III. During the design process, the front plate thickness and the cell aperture were designed in order to obtain a frequency of the membrane fundamental axisymmetric mode within the frequency range of interest. Further, the other geometrical parameters such as the intermediate layer (also referred to as “rails”) thickness and the back plate thickness were designed in order to improve the device performance in receive mode in concrete-coupled conditions.

V.3.2 FEM model of the proposed device

The design process involved the use of Finite Element Analysis, which required the development of a FEM model of the proposed device. In addition to the metallic front plate and the piezoelectric disk modelled in Section V.2.2, the FEM model of the complete structure includes the thin layer of glue that attaches the piezoelectric disks to the front plate, the FR-4 rail layer and the metallic back plate. The complete 2D axisymmetric FEM model is shown in Figure V.4.

The properties of the materials included in the FEM model were taken from the literature, except for the material properties of concrete. The density and longitudinal propagation velocity of concrete used in the simulation were measured on a concrete sample, resulting in a density of $\rho = 2250$ kg/m^3 and an average longitudinal velocity of acoustic waves propagation of $v_l^{avg} = 3250$ m/s. The measurement setup for the longitudinal velocity is shown in Figure V.5.

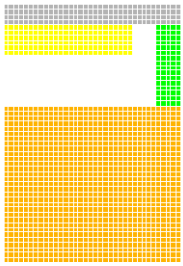

Figure V.4 *2D axisymmetric FEM model of the complete transducer flexural cell. The cell includes the steel front plate (grey), the piezoelectric layer (yellow), the epoxy rails (green), the brass back plate (orange) and the thin glue between the front plate and the piezoceramics (non-visible).*

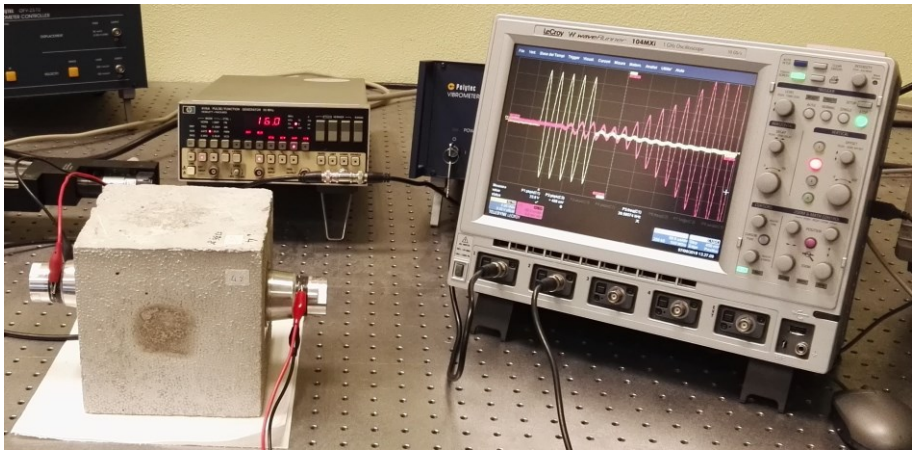

Figure V.5 *Measurement setup for the evaluation of the average longitudinal propagation velocity of the acoustic waves in a sample of concrete.*

The material properties of the structural layers included in the simulations are reported in Table V.1.

Table V.1 *Material properties of the structural layers used for the simulation.*

	Density [kg/m^3]	Young's modulus [GPa]	Poisson's number
Steel (front plate)	7900	200	0.3
Epotek 301-2 (glue)	982	12.1	0.001
FR-4 (rails)	1850	22.4	0.12
Brass (backing)	8490	97	0.31

Table V.2 lists the material constants used for the piezoelectric disk material PZT5-H.

Table V.2 *Material constants used for the PZT5-H material.*

Density [kg/m^3]	Elastic constants [10^{10} N/m^2]		Piezoelectric constants [C/m^2]		Dielectric constants	
7500	c_{11}	12.6	e_{31}	-6.5	$\varepsilon_{11}/\varepsilon_0$	1700
	c_{12}	7.95	e_{33}	23.3	$\varepsilon_{22}/\varepsilon_0$	1470
	c_{13}	8.41	e_{15}	17	$\varepsilon_{33}/\varepsilon_0$	1700
	c_{33}	11.7				
	c_{44}	2.3				
	c_{66}	2.35				

Table V.3 includes the vertical and lateral dimensions and variation range of the various elements of the device.

Table V.3 *Variation range of the geometrical parameters of the FEM model.*

	Variation range [mm]
Membrane radius r_m	2.8 – 3.2
Pitch $p = 2r_m/0.85$	6.588 – 7.529
Ceramic radius $r_c = 0.85\ r_m$	2.38 – 2.72
Membrane thickness t_m	0.2 – 1
Ceramic thickness t_c	0.2 – 1
Rails thickness t_r	0.8 – 4.8
Backing thickness t_b	3 – 10

V.3.3 Front plate design

The design of the device started from the sizing of the front-plate. The membrane radius r_m and thickness t_m fix its flexural stiffness, thus determining the plate modal frequencies according to

$$f_n = \frac{\alpha_n}{2}\frac{t_m}{\pi r_m^{\,2}}\sqrt{\frac{Y_m}{12\rho_m\left(1-\nu_m^{\,2}\right)}}\,, \tag{V.1}$$

where $\alpha_1 = 10.24$ for the first axisymmetric mode of vibration of a thin plate and Y_m, ρ_m, ν_m are respectively Young's modulus, volume density and Poisson's ratio of the elastic plate material.

By considering the frequency range 20 kHz – 200 kHz as the desired range for the device sensitivity bandwidth, the desired frequency of the first axisymmetric mode is the centre frequency $f_0 = 110$ kHz. Hence, the values of the radius r_m and the thickness t_m resulting in a flexural mode frequency f_0 can be computed by

$$r_m^2 = \frac{\alpha_1}{2\pi f_0}\sqrt{\frac{Y_m}{12\rho_m\left(1-\nu_m^{\,2}\right)}}t_m\,. \tag{V.2}$$

The cells shall house bulk piezoceramic disks, whose miniaturization is limited to some hundreds of microns of radius. For this reason, and to allow a sufficiently easy handling of components, the membrane radius was fixed at $r_m = 3$ mm. Hence, the front plate thickness chosen was $t_m = 400$ μm, as can be observed in Figure V.6.

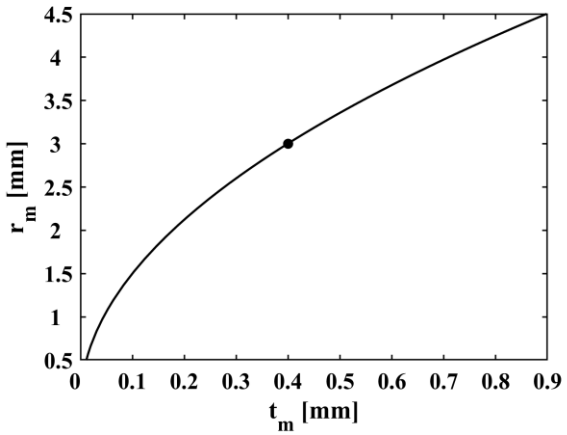

Figure V.6 *The radius and thickness design curve for a steel plate resonating at its first flexural mode at $f_0 = 110$ kHz.*

V.3.4 Piezoelectric disk design

The material chosen for the piezoelectric disk is PZT5-H, a soft piezoelectric ceramic that has been widely used over the years for its high d_{13} piezoelectric constant, which is involved in flexural deformation.

The radius of the bulk piezoceramic glued at the back surface of the front plate was obtained by choosing a disk-to-membrane ratio of 0.85, as to obtain a wide active surface by also granting enough tolerance for the disk positioning and the wire bonding. Therefore, the chosen ceramic radius was r_c = 2.55 mm.

By fixing the plate thickness and the cavity radius, the flexural mode resonance frequency is only slightly affected by the thickness of the underlying piezoelectric disk. This was proven by performing harmonic analyses on a FEM model of one membrane with clamped edge, attached to the piezoelectric layer. The structure was replicated along both lateral directions. The in-vacuum mechanical impedance was computed by extracting the normal velocity value averaged on the front-plate surface for different values of the piezoelectric disk thickness. The mechanical impedance of the device computed by FEA by varying the piezoelectric disk thickness is reported in Figure V.7. Figure V.7 confirms that the variation of the piezoceramic thickness hardly affects the first mode resonance frequency. Conversely, Figure V.8 and Figure V.9 show how the mechanical impedance maximum and minimum frequency strongly depend on the membrane geometrical parameters (the membrane radius and thickness, respectively).

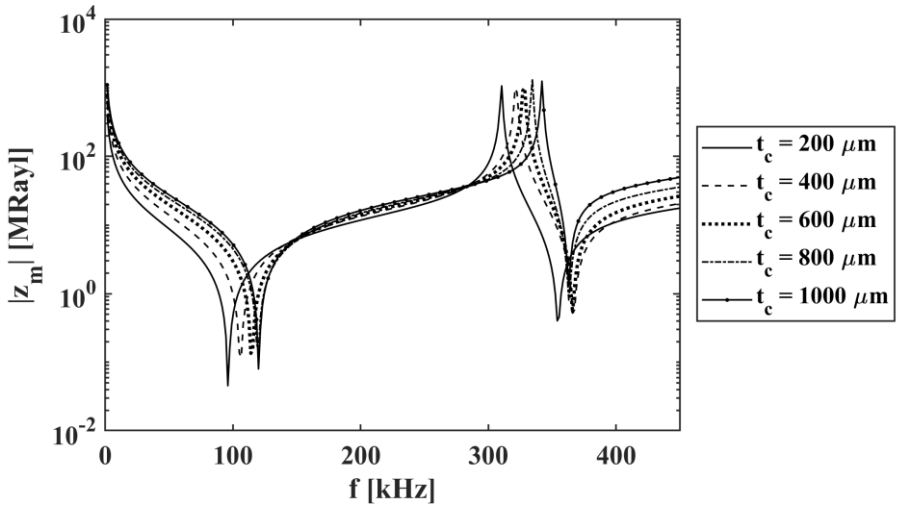

Figure V.7 *The amplitude of the resonant device mechanical impedance, computed by FEA on the structural model of the transducer by varying the thickness of the piezoelectric disk underlying the front plate.*

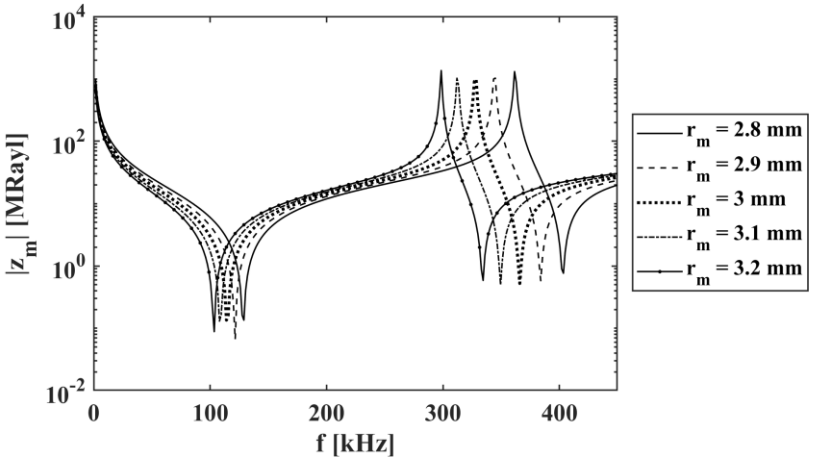

Figure V.8 *The amplitude of the resonant device mechanical impedance, computed by FEA on the structural model of the transducer by varying the radius of the membrane.*

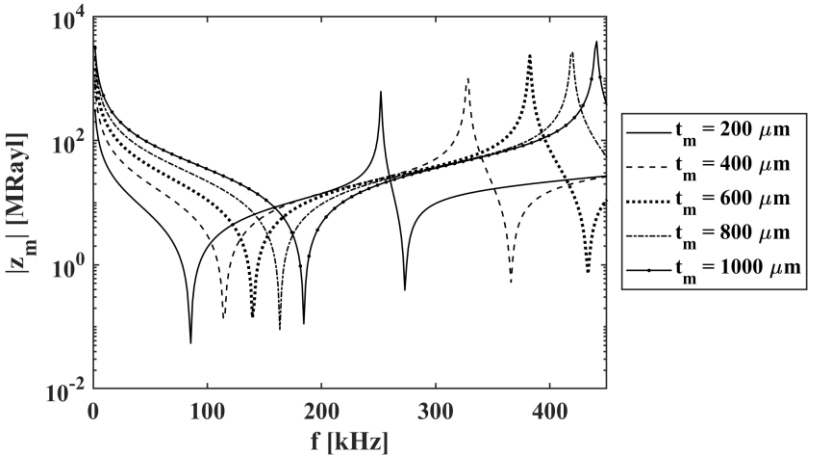

Figure V.9 *The amplitude of the resonant device mechanical impedance, computed by FEA on the structural model of the transducer by varying the thickness of the membrane.*

In order to choose the most convenient value of the piezoelectric disk thickness, the Reception Transfer Function (RTF) of the device was observed by varying t_c. The RTF was obtained by coupling the FEM axisymmetric model described in Section V.2.2 to a propagating medium having the material properties of concrete.

A uniform pressure was applied on the outer surface of the membrane, and the resulting voltage across the piezoelectric disk electrodes was extracted to compute the RTF according to eq. (III.12).

Figure V.10 shows the RTF computed by varying the piezoelectric disk thickness t_c from 200 μm to 1 mm. It can be seen how, by increasing the thickness, the transfer function bandwidth widens because the matching between the device and the load improves. By further increasing the thickness, though, the resonant peak sharpens, improving the received signals for frequencies outside the range of interest and reducing the performance below 200 kHz, which is the highest frequency of the range of interest. So, in order to design the piezoelectric disk thickness, the value returning the highest product between the maximum gain and the -3 dB bandwidth around the first relative maximum amplitude of the RTF was obtained. Therefore, the value t_c = 600 μm was chosen.

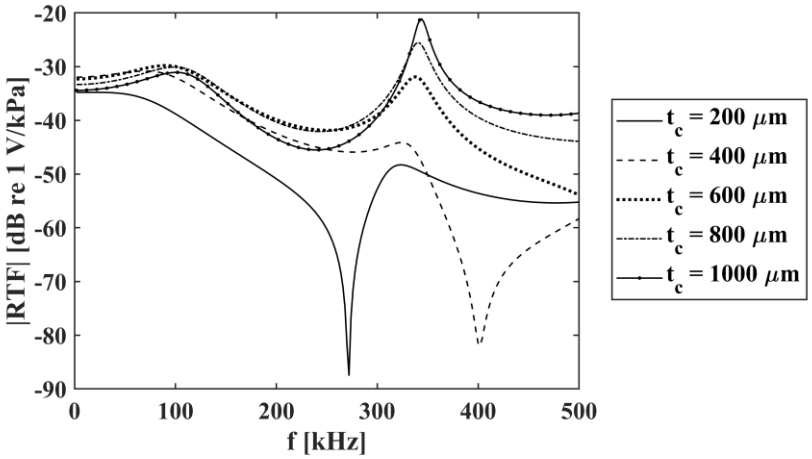

Figure V.10 *The amplitude of the transducer RTF, computed by FEA by varying the thickness of the piezoelectric disk underlying the front plate.*

V.3.5 Rails thickness design

The front plate and piezoelectric thickness design was carried out assuming the boundary condition of clamped membrane edge. This condition would accurately describe a system with a very rigid cell structure, which is not exactly the case currently considered. The rail layer into which the cavities are patterned is made of an epoxy laminate layer, whose acoustic impedance is not high enough to clamp the upper plate to the substrate. Hence, it takes part to the structure vibration when an acoustic emission signal is received, influencing the device performance in receive mode.

The effect of the rail layer was assessed by performing the harmonic finite element analysis on the model described in Section V.3.2.

By applying a uniform pressure on the front surface of the device, the average normal velocity of the front surface was extracted and used to compute the reception transfer function by varying the rail layer thickness t_r

from 0.8 mm to 4.8 mm with a step of 0.4 mm. The rail layer lower boundary was clamped. The results in Figure V.11 show that, by increasing the thickness of the rails, the RTF bandwidth narrows and the resonant peaks sharpen and shift at a lower frequency. The decrease of the frequency of the peaks is a sign of the lower flexural stiffness of the structure: the rail layer compresses and extends, thus making a movable substrate for the membranes. The increase of the peaks amplitude, on the contrary, reveals that a higher part of the energy coming from the concrete coupled to the front face contributes to the piezoelectric layer deformation, thus increasing the received voltage signal.

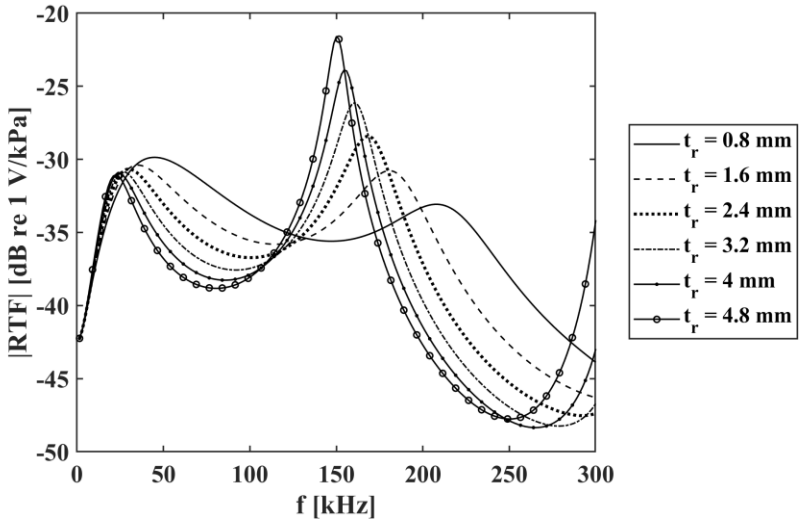

Figure V.11 *The amplitude of the transducer RTF, computed by FEA by varying the thickness of the epoxy layer patterned with the cavities, clamped at the lower edge.*

This improvement of the energy conversion can be due to the better acoustic impedance matching operated by the rails, whose acoustic impedance ($z_r \approx 6.5$ MRayl) is quite close to the concrete specific acoustic impedance ($z_L \approx 7.3$ MRayl). Due to the improved matching with respect to the case of clamped substrate (infinitely rigid backing, $z_B \to \infty$), a lower part of the incoming energy is reflected, and a higher part is conveyed to the active transduction layer.

Further investigation proved that the increased amplitude of the RTF is due to a stronger deformation of the membrane. Figure V.12 shows the amplitude of the complex displacement observed along the membrane radius, computed at the frequency of the maximum RTF amplitude for each value of the investigated rails thickness. It can be seen that the displacement amplitude increases by increasing the rail layer thickness.

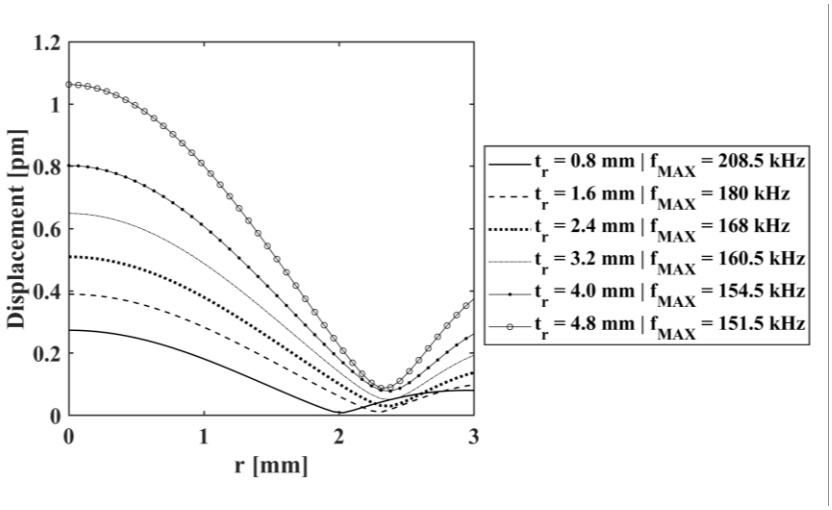

Figure V.12 *The amplitude of the displacement along the normal direction (y-axis) computed at the frequency of the maximum RTF amplitude by varying the rail layer thickness.*

Figure V.13 shows an example of flexural vibration that causes the previously shown displacement across the radius, observed at f = 186 kHz on the device provided with a rail layer thickness of t_r = 1.6 mm. Figure V.13 shows (a) the membrane deflection towards the cavity, associated with a slight compression of the rails, and (b) the membrane moving outwards, together with a compression of the rails. The overall displacement along the y-axis is much higher at the centre of the membrane, according to the flexural mode of vibration. The minimum displacement is observed at a nodal circle close to the rails. The fact that the nodal circle is not exactly placed on the outer point of the structure confirms that the rails are actually moving alternatively upwards and downwards.

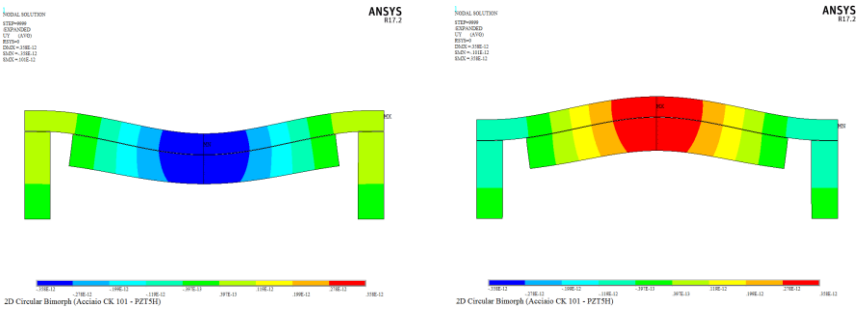

Figure V.13 *An example of flexural deformation of the membrane supported by the rails moving (a) upwards and (b) downwards in time. The frames were taken from a time-harmonic animation of the device with t_r = 1.6 mm at the frequency f_{MAX} = 186 kHz, where the RTF is maximum.*

Though the widest bandwidth of the RTF was obtained for t_r = 0.8 mm, in order to reduce the difficulties due to the electrical connection of the piezoelectric layers in a small space, a higher value for the rail thickness t_r = 1.6 mm was chosen. 1.6 mm is also the most common thickness for the conductive FR-4 layers used for PCB fabrication, thus is cheaper and more easily available on the market.

V.3.6 Back plate thickness design

The last step for the design of the flexural transducer array for acoustic emission techniques on concrete structures was the design of the metallic back plate, which acts as a mechanical support for the whole structure and provides a rigid substrate that clamps the membranes outer edge.

The material chosen for the back plate was brass, since this material is very easily processed.

The longitudinal velocity of acoustic waves is estimated in v_B = 4700 m/s [126]. Since the thickness mode resonance of the back plate occurs at

$$f_B = \frac{v_B}{2\,t_B}\ , \tag{V.3}$$

in order to place it outside of the bandwidth of the device RTF, e.g., f_B > 350 kHz, the brass backing should have a thickness

$$t_B < \frac{v_B}{2 f_B} = 6.7\ \text{mm}\,. \tag{V.4}$$

The effect of the back plate on the RTF of the transducer array was investigated by performing a harmonic analysis on the FEM model described in Section V.3.2, by varying the thickness t_b from 3 mm to 10 mm. Figure V.14 shows how the back plate resonance interferes with the RTF bandwidth when the backing thickness is increased above the value t_b = 7 mm.

For this reason, a good choice for the brass back plate thickness is t_B = 6 mm. This dimension, together with the previously described design, leads to the final RTF computed for the proposed device shown in Figure V.15. Such device has a 200 kHz-wide -6 dB bandwidth centred in f = 112 kHz in receive mode when coupled to concrete, thus is suitable for the reception of acoustic emission from concrete structures undergoing stability monitoring.

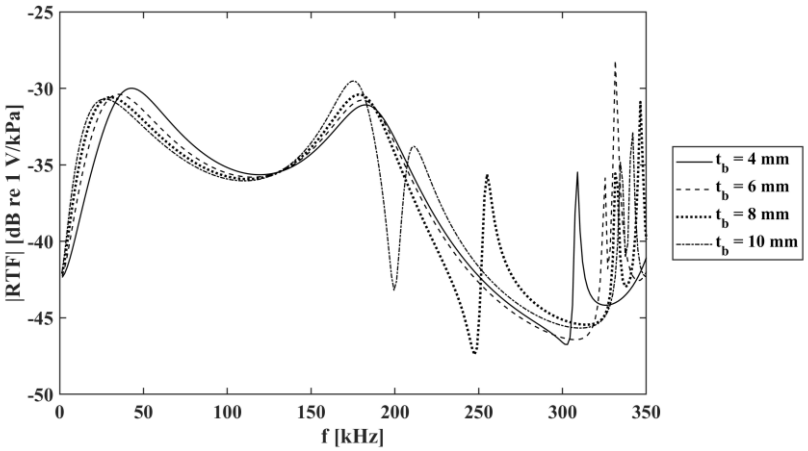

Figure V.14 *The amplitude of the transducer RTF, computed by FEA by varying the thickness of the brass back plate.*

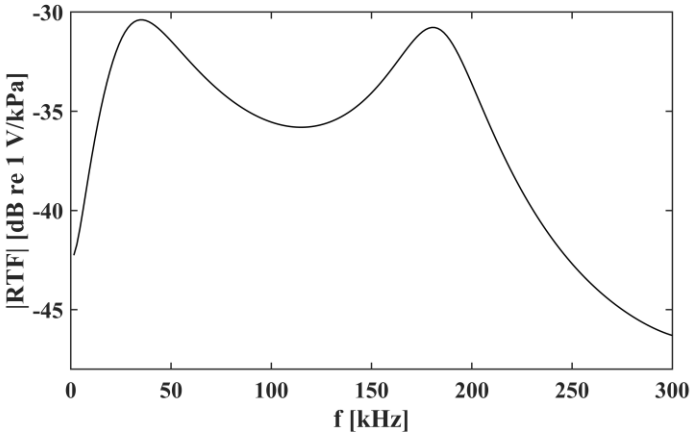

Figure V.15 *The amplitude of the transducer RTF, computed by FEA, on the final design of the proposed array.*

Conclusions

In this work, a finite element analysis of the electroacoustic behaviour of ultrasonic flexural transducer arrays was carried out.

An ANSYS model for the simulation of wide aperture multicell CMUT devices, developed by taking advantage of the circular cell axial symmetry, was used to investigate the static and dynamic performance of Reverse-Fabricated CMUTs in vacuum and in immersion. The infinite transducer model was validated by comparing the electrical impedance and the transmission sensitivity results with measurement performed on single-element RF-CMUTs, provided with different backing materials. Agreement with measurements confirms the validity of the infinite transducer model in simulating the electrical and acoustic behaviour of wide aperture CMUT devices, whose radiating surface aperture is much wider than the propagating signal wavelength.

By means of this model, the collapse voltage was computed by varying the membrane radius and thickness and the cell cavity height. By varying the bias voltage from 0 to the collapse voltage value, the increase of the static capacitance and the membrane deflection profile variation were observed. Further, the dynamic behaviour in pulse-echo immersion operation of such devices was simulated by varying the vertical and lateral dimensions and by increasing the applied bias voltage. The computation of the transmitted pressure and of the received voltage provides an accurate characterization of the devices, which serves as a useful tool for the design process of application specific transducers. The proposed model was also used to investigate the benefits of using low-impedance backing material for the reduction of the RF-CMUT front face acoustic reflectivity, thus attenuating the reverberation echoes received by the transducer by up to 8 dB. The mitigation of the reverberation phenomenon improves the received ultrasound image quality.

A FEM model of a 2D sparse RF-CMUT array element was also described. A CAD model of the array element, made by 19 circular cells arranged by hexagonal tiling, was made by the commercial software AUTOCAD and imported in ANSYS to obtain the FEM model of the device. The considered transducer array is composed of 256 elements arranged according to a density tapered golden angle Fermat's spiral, and is part of a recently developed multi-

chip module, in which the CMUT is bonded to the analog front-end ASIC by means of a thin layer of BCB. The effect of this BCB layer on the acoustic performance of the array was studied by means of transmission operation simulation in ANSYS. The pressure radiation pattern was computed by varying the boundary conditions applied to the array and to the backing layer, in order to investigate the effect of carving trenches in the BCB and in the Nitride to isolate acoustically the elements populating the array. The study of the array element beam pattern is important to assess the beam steering capabilities of the transducer array. Simulations were performed in harmonic regime at the designed operation frequency of 7 MHz. Allowing lateral displacements at the outer surface nodes of the backing layer, as if trenches were carved inside the BCB, does not improve the beam width with respect to the results obtained by considering the array element as part of an infinitely extended structure. Isolating the entire element by performing trenches in the backing and the structural Nitride increases the side lobes level thus degrading the acoustic performance, and therefore is not a desirable solution. The steering capabilities of the device obtained by ANSYS were compared to the radiated pressure measurements performed after the packaging of the transducer array and the analog front-end on the probe head prototype. The directivity simulation results are in agreement with the steered radiated field measurement, even if some differences in the main lobe level are present. These differences can be due to the rough compensation of the hydrophone directivity applied to the measured values. The simulations underestimate the side lobe level, which is about 10 dB lesser than the expected. A deeper understanding of the device performance could be obtained by simulating the sparse array acoustic behaviour on a wider range of frequencies, by also taking into account the attenuating layer of the acoustic lens placed on the device front-face. The addition of this attenuating layer in the FEM model would allow a more accurate quantification of the acoustic power generated by the device, as well as the investigation of the acoustic lens effect on the crosstalk phenomenon. Such expansion of the FEM model will be the subject of future work. The proposed model, as it is, allows the study of the beam pattern of an array element with the described membrane geometry. Nevertheless, the same model could be used also to investigate the possibility of shaping the element factor by acting on the dimensions of the membranes composing the array element, thus obtaining a phase delay that is intrinsically bounded to the device structure rather than provided by delaying the input signals. Such study could support the beamshaping techniques, and help to reduce the complexity of the beamformers.

The FEM model of a flexural plate was also used to design a piezoelectric transducer array for acoustic emission techniques applied to concrete structures for the assessment of the structural health. The model was modified to include the piezoceramic housed inside the cavity and glues to the elastic front plate. The design was carried out by computing the device Reception

Transfer Function in concrete-coupled conditions, and by varying the geometrical parameters of the membrane and of the structural material in order to obtain a broadband reception on the frequency range of interest. The resulting device 200 kHz-wide -6 dB bandwidth centred in f = 112 kHz in receive mode when coupled to concrete. The work will possibly be concluded by fabricating the designed device, and testing its functionality in acoustic emission experiments.

In the future, the FEM models used for the design of the piezoelectric transducer array and for the design of wide aperture CMUT devices could be used, with very little variations, to simulate wide aperture PMUT devices. PMUTs are very promising flextensional transducers and therefore represent an interesting topic for future research. By using the proposed FEM model and the code developed for the evaluation of the geometrical parameter variation effect, further work could be based on the design of application specific PMUT devices.

References

[1] T. Szabó, *Diagnostic ultrasound imaging : inside out*. Elsevier Academic, 2004.

[2] K. K. Shung, *Diagnostic ultrasound : imaging and blood flow measurements*. CRC Press, 2015.

[3] Q. Huang and Z. Zeng, "A Review on Real-Time 3D Ultrasound Imaging Technology," *Biomed Res. Int.*, vol. 2017, pp. 1–20, Mar. 2017.

[4] A. Fenster, G. Parraga, and J. Bax, "Three-dimensional ultrasound scanning," *Interface Focus*, vol. 1, no. 4, pp. 503–519, Aug. 2011.

[5] S. W. Smith, H. G. Pavy, and O. T. von Ramm, "High-speed ultrasound volumetric imaging system. I. Transducer design and beam steering," *IEEE Trans. Ultrason. Ferroelectr. Freq. Control*, vol. 38, no. 2, pp. 100–108, Mar. 1991.

[6] O. T. von Ramm, S. W. Smith, and H. G. Pavy, "High-speed ultrasound volumetric imaging system. II. Parallel processing and image display," *IEEE Trans. Ultrason. Ferroelectr. Freq. Control*, vol. 38, no. 2, pp. 109–115, Mar. 1991.

[7] B. Savord and R. Solomon, "Fully sampled matrix transducer for real time 3D ultrasonic imaging," in *IEEE Symposium on Ultrasonics, 2003*, pp. 945–953.

[8] O. Oralkan, A. S. Ergun, Ching-Hsiang Cheng, J. A. Johnson, M. Karaman, T. H. Lee, and B. T. Khuri-Yakub, "Volumetric ultrasound imaging using 2-D CMUT arrays," *IEEE Trans. Ultrason. Ferroelectr. Freq. Control*, vol. 50, no. 11, pp. 1581–1594, Nov. 2003.

[9] J. T. Yen and S. W. Smith, "Real-time rectilinear 3-D ultrasound using receive mode multiplexing," *IEEE Trans. Ultrason. Ferroelectr. Freq. Control*, vol. 51, no. 2, pp. 216–226, Feb. 2004.

[10] J. Woo and Y. Roh, "Ultrasonic two-dimensional array transducer of the single-unit type with a conductive backing of the 1–3 piezocomposite structure," *Jpn. J. Appl. Phys.*, vol. 53, no. 7S, p. 07KD06, Jul. 2014.

[11] S. Blaak, Z. Yu, G. C. M. Meijer, C. Prins, C. T. Lancee, J. G. Bosch,

and N. de Jong, “Design of a micro-beamformer for a 2D piezoelectric ultrasound transducer,” in *2009 IEEE International Ultrasonics Symposium*, 2009, pp. 1338–1341.

[12] U.-W. Lok and P.-C. Li, “Microbeamforming With Error Compensation,” *IEEE Trans. Ultrason. Ferroelectr. Freq. Control*, vol. 65, no. 7, pp. 1153–1165, Jul. 2018.

[13] G. Matrone, A. S. Savoia, G. Caliano, and G. Magenes, “The delay multiply and sum beamforming algorithm in ultrasound B-mode medical imaging,” *IEEE Trans. Med. Imaging*, vol. 34, no. 4, pp. 940–949, 2015.

[14] M. Karaman, A. Atalar, and H. Koymen, “VLSI circuits for adaptive digital beamforming in ultrasound imaging,” *IEEE Trans. Med. Imaging*, vol. 12, no. 4, pp. 711–720, 1993.

[15] G. Gurun, J. S. Zahorian, A. Sisman, M. Karaman, P. E. Hasler, and F. L. Degertekin, “An Analog Integrated Circuit Beamformer for High-Frequency Medical Ultrasound Imaging,” *IEEE Trans. Biomed. Circuits Syst.*, vol. 6, no. 5, pp. 454–467, Oct. 2012.

[16] G. Matrone, A. Savoia, M. Terenzi, G. Caliano, F. Quaglia, and G. Magenes, “A volumetric CMUT-based ultrasound imaging system simulator with integrated reception and μ-beamforming electronics models,” *IEEE Trans. Ultrason. Ferroelectr. Freq. Control*, vol. 61, no. 5, pp. 792–804, 2014.

[17] R. E. Davidsen, J. A. Jensen, and S. W. Smith, “Two-Dimensional Random Arrays for Real Time Volumetric Imaging,” *Ultrason. Imaging*, vol. 16, no. 3, pp. 143–163, Jul. 1994.

[18] R. M. Leahy and B. D. Jeffs, “On the design of maximally sparse beamforming arrays,” *IEEE Trans. Antennas Propag.*, vol. 39, no. 8, pp. 1178–1187, 1991.

[19] G. Lockwood, P. Li, and M. O’Donnell, “Optimizing the Radiation Pattern of Sparse Periodic Linear Arrays,” *IEEE Trans. Ultrason. Ferroelectr. Freq. Control*, vol. 43, no. 3, pp. 4473–4473, 1996.

[20] J. W. Choe, O. Oemer, and P. Khuri-Yakub, “Design Optimisation for a 2-D Sparse Transducer Array for 3-D Ultrasound Imaging,” *Proc. IEEE Ultrason. Symp.*, vol. 18, no. 9, pp. 1928–1931, 2010.

[21] E. Roux, A. Ramalli, P. Tortoli, C. Cachard, M. C. Robini, and H. Liebgott, “2-D ultrasound sparse arrays multidepth radiatio optimization using simulated annealing and spiral-array inspired energy functions,” *IEEE Trans. Ultrason. Ferroelectr. Freq. Control*, vol. 63, no. 12, pp. 2138–2149, 2016.

[22] E. Roux, A. Ramalli, H. Liebgott, C. Cachard, M. C. Robini, and P. Tortoli, “Wideband 2-D array design optimization with fabrication constraints for 3-D US imaging,” *IEEE Trans. Ultrason. Ferroelectr. Freq. Control*, vol. 64, no. 1, pp. 108–125, 2017.

[23] J. T. Yen, J. P. Steinberg, and S. W. Smith, “Sparse 2-D array design

for real time rectilinear volumetric imaging," *IEEE Trans. Ultrason. Ferroelectr. Freq. Control*, vol. 47, no. 1, pp. 93–110, Jan. 2000.

[24] E. Roux, F. Varray, L. Petrusca, C. Cachard, P. Tortoli, and H. Liebgott, "Experimental 3-D Ultrasound Imaging with 2-D Sparse Arrays using Focused and Diverging Waves," *Sci. Rep.*, vol. 8, no. 1, p. 9108, Dec. 2018.

[25] A. Ramalli and P. Tortoli, "256-element density-tapered spiral matrices for ultrasound phased imaging," in *2014 IEEE International Ultrasonics Symposium*, 2014, pp. 2087–2090.

[26] A. Ramalli, E. Boni, A. S. Savoia, and P. Tortoli, "Density-tapered spiral arrays for ultrasound 3-D imaging," *IEEE Trans. Ultrason. Ferroelectr. Freq. Control*, vol. 62, no. 8, pp. 1580–1588, 2015.

[27] M. I. Haller and B. T. Khuri-Yakub, "A surface micromachined electrostatic ultrasonic air transducer," in *1994 Proceedings of IEEE Ultrasonics Symposium*, 1994, pp. 1241–1244 vol.2.

[28] I. Ladabaum, B. T. Khuri-Yakub, D. Spoliansky, and M. I. Haller, "Micromachined ultrasonic transducers (MUTs)," *IEEE Int. Ultrason. Symp.*, pp. 501–504, 1995.

[29] D. W. Schindel, D. A. Hutchins, Lichun Zou, and M. Sayer, "The design and characterization of micromachined air-coupled capacitance transducers," *IEEE Trans. Ultrason. Ferroelectr. Freq. Control*, vol. 42, no. 1, pp. 42–50, Jan. 1995.

[30] I. Ladabaum, X. Jin, H. T. T. Soh, F. Pierre, A. Atalart, E. L. G. Lnboratory, S. Universitv, S. Ca, I. Ladabaum, A. Atalar, and B. T. Khuri-Yakub, "Microfabricated ultrasonic transducers: towards robust models and immersion devices," *1996 IEEE Ultrason. Symp. Proc.*, vol. 1, pp. 335–338, 1996.

[31] I. Ladabaum, X. Jin, H. T. Soh, A. Atalar, and B. T. Khuri-Yakub, "Surface micromachined capacitive ultrasonic transducers," *IEEE Trans. Ultrason. Ferroelectr. Freq. Control*, vol. 45, no. 3, pp. 678–690, 1998.

[32] G. Caliano, V. Foglietti, E. Cianci, and M. Pappalardo, "A silicon microfabricated electrostatic transducer: 1 MHz transmission in air and in water," *Microelectron. Eng.*, vol. 53, no. 1–4, pp. 573–576, Jun. 2000.

[33] X. C. Jin, F. L. Degertekin, S. Calmes, X. J. Zhang, I. Ladabaum, and B. T. Khuri-Yakub, "Micromachined capacitive transducer arrays for medical ultrasound imaging," in *1998 IEEE Ultrasonics Symposium. Proceedings (Cat. No. 98CH36102)*, vol. 2, pp. 1877–1880.

[34] Ö. Oralkan, A. S. Ergun, J. A. Johnson, M. Karaman, U. Demirci, K. Kaviani, T. H. Lee, and B. T. Khuri-Yakub, "Capacitive micromachined ultrasonic transducers: Next-generation arrays for acoustic imaging?," *IEEE Trans. Ultrason. Ferroelectr. Freq. Control*, vol. 49, no. 11, pp. 1596–1610, 2002.

[35] G. Caliano, R. Carotenuto, A. Caronti, and M. Pappalardo, “cMUT echographic probes: design and fabrication process,” in *2002 IEEE Ultrasonics Symposium, 2002. Proceedings.*, vol. 2, pp. 1067–1070.
[36] Ö. Oralkan, A. S. Ergun, C. H. Cheng, J. A. Johnson, M. Karaman, T. H. Lee, and B. T. Khuri-Yakub, “Volumetric ultrasound imaging using 2-D CMUT arrays,” *IEEE Trans. Ultrason. Ferroelectr. Freq. Control*, vol. 50, no. 11, pp. 1581–1594, 2003.
[37] U. Demirci, A. S. Ergun, Ö. Oralkan, M. Karaman, and B. T. Khuri-Yakub, “Forward-viewing CMUT arrays for medical imaging,” *IEEE Trans. Ultrason. Ferroelectr. Freq. Control*, vol. 51, no. 7, pp. 887–895, 2004.
[38] D. M. Mills and L. S. Smith, “Real-time in-vivo imaging with capacitive micromachined ultrasound transducer (cMUT) linear arrays,” in *IEEE Symposium on Ultrasonics, 2003*, pp. 568–571.
[39] S. Panda, C. Daft, and P. Wagner, “Microfabricated ultrasound transducer (CMUT) probes: imaging advantages over piezoelectric probes,” *Ultrasound Med. Biol.*, vol. 29, no. 5, p. S69, May 2003.
[40] G. Caliano, R. Carotenuto, E. Cianci, V. Foglietti, A. Caronti, and M. Pappalardo, “A cMUT linear array used as echographic probe: fabrication, characterization, and images,” in *IEEE Ultrasonics Symposium, 2004*, vol. 1, pp. 395–398.
[41] A. Savoia, G. Caliano, R. Carotenuto, C. Longo, P. Gatta, A. Caronti, E. Cianci, V. Foglietti, and M. Pappalardo, “Enhanced echographic images obtained improving the membrane structural layer of the cMUT probe,” *Proc. - IEEE Ultrason. Symp.*, vol. 4, no. c, pp. 1960–1963, 2005.
[42] A. Caronti, G. Caliano, R. Carotenuto, A. Savoia, M. Pappalardo, E. Cianci, and V. Foglietti, “Capacitive micromachined ultrasonic transducer (CMUT) arrays for medical imaging,” *Microelectronics J.*, vol. 37, no. 8, pp. 770–777, 2006.
[43] B. Bayram, M. Kupnik, G. G. Yaralioglu, Ö. Oralkan, A. S. Ergun, D. S. Lin, S. H. Wong, and B. T. Khuri-Yakub, “Finite element modeling and experimental characterization of crosstalk in 1-D CMUT arrays,” *IEEE Trans. Ultrason. Ferroelectr. Freq. Control*, vol. 54, no. 2, pp. 418–429, 2007.
[44] A. S. Savoia, G. Caliano, and M. Pappalardo, “A CMUT probe for medical ultrasonography: From microfabrication to system integration,” *IEEE Trans. Ultrason. Ferroelectr. Freq. Control*, vol. 59, no. 6, pp. 1127–1138, 2012.
[45] J. W. Choe, O. Oralkan, A. Nikoozadeh, M. Gencel, D. N. Stephens, M. O’Donnell, D. J. Sahn, and B. T. Khuri-Yakub, “Volumetric real-time imaging using a CMUT ring array,” *IEEE Trans. Ultrason. Ferroelectr. Freq. Control*, vol. 59, no. 6, pp. 1201–1211, Jun. 2012.
[46] D. F. Lemmerhirt, Xiaoyang Cheng, R. D. White, C. A. Rich, Man

Zhang, J. B. Fowlkes, and O. D. Kripfgans, “A 32 x 32 capacitive micromachined ultrasonic transducer array manufactured in standard CMOS,” *IEEE Trans. Ultrason. Ferroelectr. Freq. Control*, vol. 59, no. 7, pp. 1521–1536, Jul. 2012.

[47] C. Tekes, J. Zahorian, G. Gurun, S. Satir, T. Xu, M. Hochman, and F. L. Degertekin, “Volumetric imaging using single chip integrated CMUT-on-CMOS IVUS array,” in *2012 Annual International Conference of the IEEE Engineering in Medicine and Biology Society*, 2012, pp. 3195–3198.

[48] T. L. Christiansen, M. F. Rasmussen, J. P. Bagge, L. N. Moesner, J. A. Jensen, and E. V. Thomsen, “3-D imaging using row–column-addressed arrays with integrated apodization— part ii: transducer fabrication and experimental results,” *IEEE Trans. Ultrason. Ferroelectr. Freq. Control*, vol. 62, no. 5, pp. 959–971, May 2015.

[49] A. S. Ergun, Y. Huang, X. Zhuang, Ö. Oralkan, G. G. Yaralıoglu, and B. T. Khuri-Yakub, “Capacitive Micromachined Ultrasonic Transducers: Fabrication Technology,” *IEEE Trans. Ultrason. Ferroelectr. Freq. Control*, vol. 52, no. 12, pp. 2242–2258, Dec. 2005.

[50] M. I. Haller and B. T. Khuri-yakub, “A Surface Micromachined Electrostatic Ultrasonic Air Transducer,” *IEEE Trans. Ultrason. Ferroelectr. Freq. Control*, vol. 43, no. 1, 1996.

[51] X. Jin, I. Ladabaum, and B. T. Khuri-Yakub, “The microfabrication of capacitive ultrasonic transducers,” *J. Microelectromechanical Syst.*, vol. 7, no. 3, pp. 295–302, 1998.

[52] P.-C. Eccardt, K. Niederer, T. Scheiter, and C. Hierold, “Surface micromachined ultrasound transducers in CMOS technology,” *1996 IEEE Ultrason. Symp. Proc.*, vol. 2, pp. 959–962, 1996.

[53] Y. Huang, A. Sanli Ergun, E. Hæggström, M. H. Badi, and B. T. Khuri-Yakub, “Fabricating capacitive micromachined ultrasonic transducers with wafer-bonding technology,” *J. Microelectromechanical Syst.*, vol. 12, no. 2, pp. 128–137, Apr. 2003.

[54] G. Caliano, A. Caronti, A. Savoia, C. Longo, M. Pappalardo, E. Cianci, and V. Foglietti, “Capacitive Micromachined Ultrasonic Transducer (cMUT) made by a novel ‘reverse fabrication process,’” *Proc. - IEEE Ultrason. Symp.*, vol. 1, no. c, pp. 479–482, 2005.

[55] A. Coppa, E. Cianci, V. Foglietti, G. Caliano, and M. Pappalardo, “Building CMUTs for imaging applications from top to bottom,” *Microelectron. Eng.*, vol. 84, no. 5–8, pp. 1312–1315, 2007.

[56] J. Zahorian, R. Guldiken, G. Gurun, M. S. Qureshi, M. Balantekin, F. L. Degertekin, S. Carlier, A. Sisman, and M. Karaman, “2F-2 Annular CMUT Arrays for Side Looking Intravascular Ultrasound Imaging,” in *2007 IEEE Ultrasonics Symposium Proceedings*, 2007,

pp. 84–87.
[57] A. Nikoozadeh, O. Oralkan, M. Gencel, J. W. Choe, D. N. Stephens, A. de la Rama, P. Chen, F. Lin, A. Dentinger, D. Wildes, K. Thomenius, K. Shivkumar, A. Mahajan, C. H. Seo, M. O'Donnell, U. Truong, D. J. Sahn, and P. T. Khuri-Yakub, "Forward-looking intracardiac imaging catheters using fully integrated CMUT arrays," in *2010 IEEE International Ultrasonics Symposium*, 2010, pp. 770–773.
[58] D. N. Stephens, U. T. Truong, A. Nikoozadeh, Ö. Oralkan, C. H. Seo, J. Cannata, A. Dentinger, K. Thomenius, A. de la Rama, T. Nguyen, F. Lin, P. Khuri-Yakub, A. Mahajan, K. Shivkumar, M. O'Donnell, and D. J. Sahn, "First In Vivo Use of a Capacitive Micromachined Ultrasound Transducer Array-Based Imaging and Ablation Catheter," *J. Ultrasound Med.*, vol. 31, no. 2, pp. 247–256, Feb. 2012.
[59] G. Jung, A. Pirouz, C. Tekes, T. Carpenter, M. W. Rashid, A. Revanitabar, D. Cowell, S. Freear, M. Ghovanloo, and F. L. Degertekin, "Single-Chip Reduced-Wire CMUT-on-CMOS System for Intracardiac Echocardiography," in *2018 IEEE International Ultrasonics Symposium (IUS)*, 2018, pp. 1–4.
[60] E. F. Arkan and F. L. Degertekin, "Analysis and Design of High Frequency 1-D CMUT Imaging Arrays in Non-collapsed Mode," *IEEE Trans. Ultrason. Ferroelectr. Freq. Control*, pp. 1–1, 2018.
[61] A. Stuart Savoia, B. Mauti, L. Fanni, G. Caliano, E. Boni, P. Mattesini, M. Scaringella, and P. Tortoli, "A 120+ 120- Element Crisscross CMUT Probe's with Real-Time Switchable Electronic and Fresnel Focusing Capabilities," in *2018 IEEE International Ultrasonics Symposium (IUS)*, 2018, pp. 1–4.
[62] B.-H. Kim, Y. Kim, S. Lee, K. Cho, and J. Song, "Design and test of a fully controllable 64×128 2-D CMUT array integrated with reconfigurable frontend ASICs for volumetric ultrasound imaging," in *2012 IEEE International Ultrasonics Symposium*, 2012, pp. 77–80.
[63] A. Moini, A. Nikoozadeh, J. W. Choe, C. Chang, D. N. Stephens, D. J. Sahn, and P. T. Khuri-Yakub, "Fully integrated 2D CMUT ring arrays for endoscopic ultrasound," in *2016 IEEE International Ultrasonics Symposium (IUS)*, 2016, pp. 1–4.
[64] A. S. Savoia, B. Mauti, G. Caliano, G. Matrone, M. Piastra, R. Bardelli, F. Toia, F. Quaglia, and A. Ramalli, "A 3D packaging technology for acoustically optimized integration of 2D CMUT arrays and front end circuits," *IEEE Int. Ultrason. Symp. IUS*, no. c, pp. 3–6, 2017.
[65] O. Martínez, C. J. Martín, G. Godoy, and L. G. Ullate, "2D array based on fermat spiral," *Phys. Procedia*, vol. 3, no. 1, pp. 399–406, 2010.
[66] A. Ramalli, E. Boni, and A. S. Savoia, "Density-tapered spiral arrays

for ultrasound 3-D imaging," *IEEE Trans. Ultrason. Ferroelectr. Freq. Control*, vol. 62, no. 8, pp. 1580–1588, Aug. 2015.

[67] A. S. Savoia and G. Caliano, "MEMS-Based Transducers (CMUT) and Integrated Electronics for Medical Ultrasound Imaging," 2018, pp. 421–429.

[68] A. Ronnekleiv, I. Ladabaum, X. Jin, and B. T. Khuri-Yakub, "An Improved Circuit Model of MUTs," *IEEE Int. Ultrason. Symp.*, pp. 395–399, 1997.

[69] R. N. (Robert N. . Thurston and W. P. (Warren P. Mason, *Physical acoustics : principles and methods*. Academic Press, 1964.

[70] A. Bozkurt, I. Ladabaum, A. Atalar, and B. T. Khuri-Yakub, "Theory and analysis of electrode size optimization for capacitive microfabricated ultrasonic transducers," *IEEE Trans. Ultrason. Ferroelectr. Freq. Control*, vol. 46, no. 6, pp. 1364–1374, Nov. 1999.

[71] I. O. Wygant, M. Kupnik, and B. T. Khuri-Yakub, "Analytically calculating membrane displacement and the equivalent circuit model of a circular CMUT cell," *Proc. - IEEE Ultrason. Symp.*, no. 6, pp. 2111–2114, 2008.

[72] A. Caronti, G. Caliano, A. Iula, and M. Pappalardo, "An accurate model for capacitive micromachined ultrasonic transducers," *IEEE Trans. Ultrason. Ferroelectr. Freq. Contr.*, vol. 49, no. 2, pp. 159–68, 2002.

[73] M. Maadi and R. J. Zemp, "Self and Mutual Radiation Impedances for Modeling of Multi-Frequency CMUT Arrays," *IEEE Trans. Ultrason. Ferroelectr. Freq. Control*, vol. 63, no. 9, pp. 1441–1454, 2016.

[74] H. Köymen, M. N. Şenlik, A. A. Alar, and S. Olcum, "Parametric linear modeling of circular cMUT membranes in vacuum," *IEEE Trans. Ultrason. Ferroelectr. Freq. Control*, vol. 54, no. 6, pp. 1229–1239, 2007.

[75] H. K. Oguz, S. Olcum, M. N. Senlik, A. Atalar, and H. Köymen, "A novel equivalent circuit model for CMUTs," *Proc. - IEEE Ultrason. Symp.*, no. 2, pp. 2193–2196, 2009.

[76] P. C. Eccardt, P. Wagner, and S. Hansen, "Analytical models for micromachined transducers - An overview," *Proc. - IEEE Ultrason. Symp.*, vol. 1, pp. 572–581, 2006.

[77] J. D. Fraser and P. Reynolds, "Finite-element method for determination of electromechanical coupling coefficient for piezoelectric and capacitive micromachined ultrasonic transducers," *J. Acoust. Soc. Am.*, vol. 108, no. 5, pp. 2599–2599, Nov. 2000.

[78] G. G. Yaralioglu, A. S. Ergun, B. Bayram, E. Haeggström, and B. T. Khuri-Yakub, "Calculation and measurement of electromechanical coupling coefficient of capacitive micromachined ultrasonic transducers.," *IEEE Trans. Ultrason. Ferroelectr. Freq. Control*, vol.

50, no. 4, pp. 449–456, 2003.
[79] B. Bayram, E. Hæggström, G. G. Yaralioglu, and B. T. Khuri-Yakub, "A new regime for operating capacitive micromachined ultrasonic transducers," *IEEE Trans. Ultrason. Ferroelectr. Freq. Control*, vol. 50, no. 9, pp. 1184–1190, 2003.
[80] G. G. Yaralioglu, a. S. Ergun, and B. T. Khuri-Yakub, "Finite-element analysis of capacitive micromachined ultrasonic transducers," *IEEE Trans. Ultrason. Ferroelectr. Freq. Control*, vol. 52, no. 12, pp. 2185–98, 2005.
[81] A. Lohfink, P.-C. Eccardt, W. Benecke, and H. Meixner, "Derivation of a 1D CMUT model from FEM results for linear and nonlinear equivalent circuit simulation," in *IEEE Symposium on Ultrasonics, 2003*, pp. 465–468.
[82] B. Bayram, G. G. Yaralioglu, a. S. Ergun, M. Oralkan, and B. T. Khuri-Yakub, "Dynamic FEM analysis of multiple cMUT cells in immersion [capacitive micromachined ultrasonic transducers]," *IEEE Ultrason. Symp. 2004*, vol. 1, no. c, pp. 252–255, 2004.
[83] G. G. Yaralioglu, B. Bayram, A. Nikoozadeh, and B. T. P. Khuri-Yakub, "Finite element modeling of capacitive micromachined ultrasonic transducers," in *Medical Imaging 2005: Ultrasonic Imaging and Signal Processing*, 2005, vol. 5750, p. 77.
[84] M. La Mura, N. A. Lamberti, B. L. Mauti, G. Caliano, and A. S. Savoia, "Acoustic reflectivity minimization in Capacitive Micromachined Ultrasonic Transducers (CMUTs)," *Ultrasonics*, vol. 73, pp. 130–139, 2017.
[85] B. Bayram, G. G. Yaralioglu, M. Kupnik, A. S. Ergun, O. Oralkan, A. Nikoozadeh, and B. T. Khuri-Yakub, "Dynamic analysis of capacitive micromachined ultrasonic transducers.," *IEEE Trans. Ultrason. Ferroelectr. Freq. Control*, vol. 52, no. 12, pp. 2270–5, 2005.
[86] A. Caronti, G. Caliano, P. Gatta, C. Longo, A. Savoia, and M. Pappalardo, "A finite element tool for the analysis and the design of capacitive micromachined ultrasonic transducer (cMUT) arrays for medical imaging," *J. Acoust. Soc. Am.*, vol. 123, no. 5, pp. 3375–3375, May 2008.
[87] L. E. Kinsler and A. R. Frey, *Fundamentals of Acoustics (4th ed.)*. New York Wiley, 2000.
[88] ANSYS, *ANSYS Mechanical APDL Element Reference*. Ansys, Inc., 2016.
[89] A. W. Leissa, *Vibration of plates*. 1969.
[90] S. Timoshenko and S. Woinowsky-Krieger, *Theory of Plates and Shells*. McGraw-Hill, 1959.
[91] S. Olcum, M. N. Senlik, and A. Atalar, "Optimization of the gain-bandwidth product of capacitive micromachined ultrasonic

transducers," *IEEE Trans. Ultrason. Ferroelectr. Freq. Control*, vol. 52, no. 12, pp. 2211–2219, Dec. 2005.

[92] A. Sako, M. Sato, H. Tanaka, and T. Nagata, "Optimization of backside structures with wideband reflectivity reduction for a CMUT," *2015 IEEE Int. Ultrason. Symp. IUS 2015*, 2015.

[93] M. Nickel, "A New Model Describing Ultrasound Reflectivity at the Transducer Surface," pp. 889–892, 1996.

[94] A. S. Savoia, M. La Mura, B. Mauti, N. Lamberti, and G. Caliano, "Reverberation reduction in capacitive micromachined ultrasonic transducers (CMUTs) by front-face reflectivity minimization," *Phys. Procedia*, vol. 70, pp. 941–944, 2015.

[95] K. K. Win, J. Wang, C. Zhang, and R. Yang, "Identification and removal of reverberation in ultrasound imaging," *Proc. 2010 5th IEEE Conf. Ind. Electron. Appl. ICIEA 2010*, pp. 1675–1680, 2010.

[96] I. Ladabaum, P. Wagner, C. Zanelli, J. Mould, P. Reynolds, and G. Wojcik, "Silicon substrate ringing in microfabricated ultrasonic transducers," *Proc. IEEE Ultrason. Symp.*, vol. 1, pp. 943–946, 2000.

[97] A. Rønnekleiv, "Design modeling of CMUT's for medical imaging," *Proc. - IEEE Ultrason. Symp.*, pp. 442–450, 2009.

[98] K. R. Chapagain and A. Rønnekleiv, "Minimizing the bottom reflection in ultrasonic CMUT transducer backing using low profile structuring," *Proc. - IEEE Ultrason. Symp.*, pp. 430–433, 2009.

[99] K. R. Chapagain and A. Rønnekleiv, "Grooved backing structure for CMUTs," *IEEE Trans. Ultrason. Ferroelectr. Freq. Control*, vol. 60, no. 11, pp. 2440–2452, 2013.

[100] G. S. Kino, *Acoustic Waves: Devices, Imaging, and Analog Signal Processing*, vol. 100. 1987.

[101] D. T. Porter, "Self- and Mutual-Radiation Impedance and Beam Patterns for Flexural Disks in a Rigid Plane," *J. Acoust. Soc. Am.*, vol. 36, no. 6, pp. 1154–1161, 1964.

[102] K. K. Park and B. T. Khuri-Yakub, "Dynamic response of an array of flexural plates in acoustic medium," *J. Acoust. Soc. Am.*, vol. 132, no. 4, pp. 2292–2303, 2012.

[103] E. Boni, L. Bassi, A. Dallai, F. Guidi, V. Meacci, A. Ramalli, S. Ricci, and P. Tortoli, "ULA-OP 256: A 256-Channel Open Scanner for Development and Real-Time Implementation of New Ultrasound Methods," *IEEE Trans. Ultrason. Ferroelectr. Freq. Control*, vol. 63, no. 10, pp. 1488–1495, Oct. 2016.

[104] A. Ramos and J. L. S. Emeterio, "Ultrasonic Systems for Non-Destructive Testing Using Piezoelectric Transducers:.Electrical Responses and Main Schemes," in *Piezoelectric Transducers and Applications*, Berlin, Heidelberg: Springer Berlin Heidelberg, 2009, pp. 413–431.

[105] J. Jung, W. Lee, W. Kang, E. Shin, J. Ryu, and H. Choi, "Review of

piezoelectric micromachined ultrasonic transducers and their applications Review of piezoelectric micromachined ultrasonic transducers and their applications Topical Review," *J. Micromechanics Microengineering Top. Rev.*, vol. 27, p. 24, 2017.
[106] G. Percin and B. Khuri-Yakub, "Micromachined 2-D array piezoelectrically actuated flextensional transducers," *1997 IEEE Ultrason. Symp. Proc.*, vol. 2, pp. 959–962, 1997.
[107] G. Perçin and B. T. Khuri-Yakub, "Piezoelectrically actuated flextensional micromachined ultrasound droplet ejectors," *IEEE Trans. Ultrason. Ferroelectr. Freq. Control*, vol. 49, no. 6, pp. 756–766, 2002.
[108] G. Percin and B. T. Khuri-Yakub, "Piezoelectrically actuated flextensional micromachined ultrasound transducers. II. Fabrication and experiments," *IEEE Trans. Ultrason. Ferroelectr. Freq. Control*, vol. 49, no. 5, pp. 585–595, May 2002.
[109] F. Akasheh, T. Myers, J. D. Fraser, S. Bose, and A. Bandyopadhyay, "Development of piezoelectric micromachined ultrasonic transducers," *Sensors Actuators A Phys.*, vol. 111, no. 2–3, pp. 275–287, Mar. 2004.
[110] J. Li, W. Ren, G. Fan, and C. Wang, "Design and Fabrication of Piezoelectric Micromachined Ultrasound Transducer (pMUT) with Partially-Etched ZnO Film.," *Sensors (Basel).*, vol. 17, no. 6, Jun. 2017.
[111] A. Ben Amar, H. Cao, and A. B. Kouki, "Modeling and process design optimization of a piezoelectric micromachined ultrasonic transducers (PMUT) using lumped elements parameters," *Microsyst. Technol.*, vol. 23, no. 10, pp. 4659–4669, Oct. 2017.
[112] D. E. Dausch, K. H. Gilchrist, J. B. Carlson, S. D. Hall, J. B. Castellucci, and O. T. von Ramm, "In vivo real-time 3-D intracardiac echo using PMUT arrays," *IEEE Trans. Ultrason. Ferroelectr. Freq. Control*, vol. 61, no. 10, pp. 1754–1764, Oct. 2014.
[113] Y. Lu, H. Tang, S. Fung, Q. Wang, J. M. Tsai, M. Daneman, B. E. Boser, and D. A. Horsley, "Ultrasonic fingerprint sensor using a piezoelectric micromachined ultrasonic transducer array integrated with complementary metal oxide semiconductor electronics," *Appl. Phys. Lett.*, vol. 106, no. 26, p. 263503, Jun. 2015.
[114] C. P. Germano, "Flexure Mode Piezoelectric Transducers," *IEEE Trans. Audio Electroacoust.*, vol. 19, no. 1, pp. 6–12, 1971.
[115] S. Dixon, L. Kang, M. Ginestier, C. Wells, G. Rowlands, and A. Feeney, "The electro-mechanical behaviour of flexural ultrasonic transducers," *Appl. Phys. Lett.*, vol. 110, no. 22, pp. 1–5, 2017.
[116] A. Feeney, L. Kang, G. Rowlands, and S. Dixon, "The dynamic performance of flexural ultrasonic transducers," *Sensors (Switzerland)*, vol. 18, no. 1, 2018.

[117] V. V. Varadan, C. C. Liang, and V. K. Varadan, “Finite-element modeling of flextensional electroacoustic transducers,” *Smart Mater. Struct.*, vol. 2, no. 4, pp. 201–207, 1993.

[118] N. A. Lamberti, M. La Mura, V. Apuzzo, A. Casella, P. D’Uva, G. Caliano, and A. S. Savoia, “A resonant sensor for liquid density measurement based on a piezoelectric bimorph,” *Proc. - 2015 6th IEEE Int. Work. Adv. Sensors Interfaces, IWASI 2015*, pp. 293–296, 2015.

[119] N. A. Lamberti, M. La Mura, V. Apuzzo, N. Greco, and P. D’Uva, “Optimization of a piezoelectric resonant sensor for liquids density measurement,” *IEEE Int. Ultrason. Symp. IUS*, vol. 2016–Novem, pp. 16–19, 2016.

[120] N. A. Lamberti, M. La Mura, V. Apuzzo, N. Greco, and P. D’Uva, “A sensor for the measurement of liquids density,” in *Lecture Notes in Electrical Engineering*, 2018, vol. 431, pp. 30–36.

[121] N. A. Lamberti, M. La Mura, C. Guarnaccia, G. Rizzano, C. Chisari, J. Quartieri, and N. E. Mastorakis, “An ultrasound technique for the characterization of the acoustic emission of reinforced concrete beam,” in *Lecture Notes in Electrical Engineering*, 2019, vol. 489, pp. 63–68.

[122] D. Masera, P. Bocca, and A. Grazzini, “Frequency analysis of acoustic emission signal to monitor damage evolution in masonry structures,” *J. Phys. Conf. Ser.*, vol. 305, no. 1, 2011.

[123] N. A. A. S. Bahari, S. Shahidan, S. R. Abdullah, N. Ali, S. S. Mohd Zuki, M. H. W. Ibrahim, and M. A. Rahim, “Crack classification in concrete beams using AE parameters,” *IOP Conf. Ser. Mater. Sci. Eng.*, vol. 271, no. 1, pp. 1–8, 2017.

[124] A. S. Savoia, B. Mauti, G. Caliano, and N. Lamberti, “A low frequency broadband flexural mode ultrasonic transducer for immersion applications,” in *2014 IEEE International Ultrasonics Symposium*, 2014, pp. 2591–2594.

[125] A. S. Savoia, B. Mauti, and G. Caliano, “A low frequency broadband flextensional ultrasonic transducer array,” *IEEE Trans. Ultrason. Ferroelectr. Freq. Control*, vol. 63, no. 1, pp. 128–138, 2016.

[126] A. R. Selfridge, “Approximate Material Properties in Isotropic Materials,” *IEEE Trans. Sonics Ultrason.*, vol. 32, no. 3, pp. 381–394, 1985.